Charles University, Faculty of Mathematics and Physics
Astronomical Institute

# Thermal Effects in the Physics and Dynamics of the Small Solar System Bodies

Ph.D. Thesis

David Čapek


Supervisor: Doc. RNDr. David Vokrouhlický, DrSc.

Prague, 2007

Čapek, David

Thermal effects in the physics and dynamics of the small solar system bodies

keywords: YORP effect, Yarkovsky effect, asteroids, heat diffusion

**Acknowledgements**

I would like to thank my supervisor David Vokrouhlický, who is a co-autor of this research, for kind leadership, as well as for many suggestions concerning this Thesis. Furthermore, I wish to thank Miroslav Brož especially for his great help with the text of the Thesis, and Josef Ďurech for useful proposals. I am also thankful to Martin Černý, Lukáš Hambálek, Jana Hekalová Katka Milerová and Petr Kotas for their help with English. At last, I am very grateful to my parents for their universal support during all my studies.

# Contents

# Chapter 1

# Introduction

## 1.1 Motivation and aims of our work

Phenomena produced by thermal radiation forces and torques have been extensively studied during last 20 years, since they were recognized to be very important with respect to the dynamics of small Solar System bodies. A phenomenon which is known as *the Yarkovsky effect* is able to secularly change the semimajor axis of an orbit, while *the YORP effect* affects the rotation state of a body.

The Yarkovsky force and the YORP torque were previously calculated with many constraining assumptions like spherical shapes, circular orbits, small variations of the surface temperature, principal axis rotation, constant thermal parameters, etc. We developed a model of the Yarkovsky/YORP effect without such simplifications. With this model we were able to study thermal phenomena in more complex circumstances.

## 1.2 A brief review of our research

At first we focused on the YORP effect recently re-discovered by [Rubincam, 2000]. We studied the YORP effect on a sample of artificially generated shapes, roughly resembling Main Belt asteroids, and also on several shapes of real asteroids [Čapek and Vokrouhlický, 2002], [Vokrouhlický and Čapek, 2002]. These bodies were approximated by a polyhedral description, we assumed that their surface has a zero thermal conductivity and their orbits were circular.

We then improved our model and took into account the finite thermal conductivity and elliptical orbits. With this model we determined the Yarkovsky effect on asteroid (6489) Golevka for the purpose of the direct detection of the semimajor axis drift [Chesley et al., 2003]. The same model was used for the more general investigation of influence of the finite thermal conductivity on the YORP effect [Čapek and Vokrouhlický, 2004] and prediction of the detection of the YORP effect on asteroid (25143) Itokawa. The subsequent improvement of our model allowed to determine the Yarkovsky effect for tumbling asteroid (4179) Toutatis [Vokrouhlický et al., 2005a] and the binary system 2000 DP107 [Vokrouhlický et al., 2005b]. The last modification of the model allowed us to incorporate the temperature and spatial dependence of material parameters of an asteroid. It was used for the determination of Golevka's regolith parameters [Čapek and Vokrouhlický, 2005b].

As a result we have developed a sophisticated model which has following features: (i) it is able to describe very complicated shapes of asteroids by polyhedral representation, with several thousands surface triangular facets. (ii) It assumes arbitrary eccentric orbits. (iii) The rotation of the body can be both regular or tumbling. (iv) The insolation term (necessary for the determination of the surface temperature) is computed including mutual shadowing between

different parts of the body's surface. (In the case of binary systems it takes into account mutual eclipses between the components.) (v) The surface temperature (needed for the evaluation of the thermal force and torque) is solved numerically for each surface facet individually, using one-dimensional heat diffusion equation without any linearization. This approach assumes the body is larger than several tens of meters. (vi) Thermal parameters of the body can depend both on the temperature and the depth.

## 1.3 Structure of the thesis

This thesis is divided to four chapters and five appendices. Chapter 2 is devoted to the common base of the thermal effects: forces produced by a radiation. Chapter 3 deals with the YORP effect, while Chapter 4 discusses the Yarkovsky effect. There are brief summaries at the end of both chapters. In the Appendices we present details about our numerical model of the Yarkovsky/YORP effect: first, we deal with methods of solution of the heat diffusion problem (Appendix A). Then we present the polyhedral representation of the asteroidal shapes (Appendix B), the method for generation of artificial Gaussian shapes (Appendix C) and also several examples of shapes resembling real bodies (Appendix D). Finally we present a list of publications (Appendix E), with reprints of some of them (Appendix F).

# Chapter 2

# Radiation and corresponding forces

Let us suppose the situation in Figure 2.1, where the Sun illuminates the surface element of an asteroid. The incident direct solar radiation (D) is partially reflected (R) and partially absorbed (C). The surface with non-zero temperature emits thermal radiation (T). Here we shall derive the expressions for the forces that are applied on the surface element due to these three components of radiation.

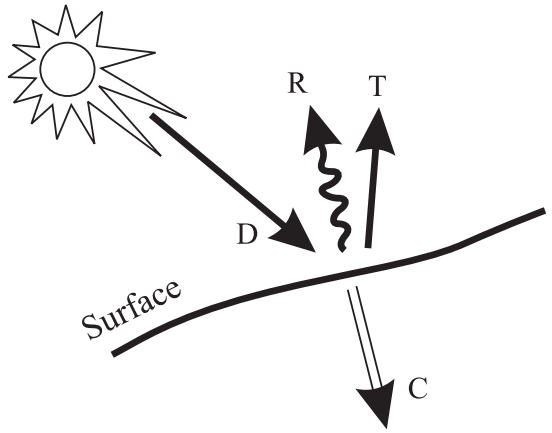


Figure 2.1: Direct (D), reflected (R) and thermally re-emitted (T) radiation from a surface element of an asteroid.

## 2.1 Direct solar radiation

The energy $dE$ of the solar radiation, hitting the oriented surface element $dS$ during the time $dt$ can be expressed as

$$dE = \Phi\, \mathbf{s} \cdot \mathbf{n}\, dS\, dt,$$

or

$$dE = 0,$$

if the Sun is below the local horizon. Here, $\Phi$ denotes the solar energy flux (in W/m$^2$ units) at the given distance from the Sun, $\mathbf{s}$ the unit vector aiming towards the Sun and $\mathbf{n}$ the outer surface normal. The force $d\mathbf{f}_{\mathrm{srp}}$ produced by the solar radiation pressure[1] is

[1]Note that the relationship between the momentum and the energy of a photon is $p = E/c$, where $c$ denotes speed of light (e.g., [Swihart, 1971]).

$$d\mathbf{f}_{\mathrm{srp}} = -\frac{\Phi}{c}\,\mathbf{s}\,\mathbf{s}\cdot\mathbf{n}\;dS\,, \tag{2.1}$$

where $c$ is the speed of light. Integrating (2.1) over the surface $\Sigma$ of a body we obtain the total force $\mathbf{f}_{\mathrm{srp}}$ produced by the solar radiation pressure:

$$\mathbf{f}_{\mathrm{srp}} = \int_{\Sigma} d\mathbf{f}_{\mathrm{srp}}\,.$$

Under normal circumstances, this force points directly from the Sun thus it is not able to secularly change the semimajor axis of an orbit. For larger bodies it only effectively weakens the solar gravitation, but it can even surpass the solar gravitation for particles with very small mass-to-area ratio. This usually occurs for $< 1\,\mu$m dust particles, e.g. [Bertotti et al., 2003]. [Vokrouhlický and Milani, 2000] showed that the direct radiation pressure (i.e., the absorbed and reflected radiation together) can produce observable long-term orbital effects for non-spherical bodies or for bodies with nontrivial albedo distribution. The total torque $\mathbf{T}_{\mathrm{srp}}$, corresponding to the direct radiation pressure, can be calculated as

$$\mathbf{T}_{\mathrm{srp}} = \int_{\Sigma} \mathbf{r}\times d\mathbf{f}_{\mathrm{srp}}\,,$$

where $\mathbf{r}$ denotes the radius vector. It is able to cause small variations of rotation during one spin period; over longer time scale it completely vanishes. [Breiter et al., 2007] showed that the torques produced by direct radiation pressure acting on spheroids are zero.

## 2.2 Reflected radiation

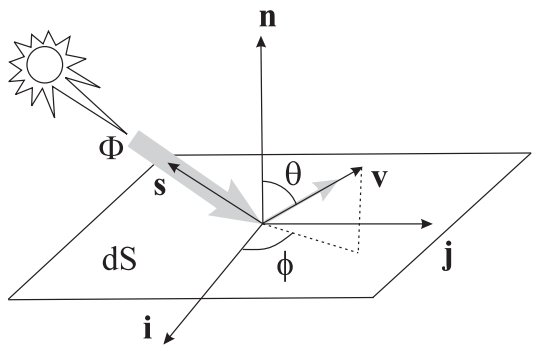


Figure 2.2: Reflection of direct solar radiation on a surface element $dS$. Here $\Phi$ is the flux of the solar radiation, $\mathbf{n}$ is the unit outer normal to $dS$, the unit vector $\mathbf{s}$ points to the Sun and the unit vector $\mathbf{v}$ parallel to the reflected radiation, is described by spherical angles $\theta$ and $\phi$.

A part of incident photons is not absorbed but it is immediately reflected into the space in the optical band. Let us suppose the situation in Figure 2.2 describing geometry of the incident and reflected radiation. The direction of reflected radiation is characterized by the unit vector $\mathbf{v}$, which can be described by angles $\theta$, $\phi$ with respect to the base ($\mathbf{i}$, $\mathbf{j}$, $\mathbf{n}$) as $\mathbf{v} = (\sin\theta\cos\phi, \sin\theta\sin\phi, \cos\theta)$. The intensity of the radiation reflected in the direction $\mathbf{v}$ can be expressed as

$$I_R(\mathbf{s},\mathbf{v}) = \Phi\rho(\mathbf{s},\mathbf{v}),$$

where $\rho(\mathbf{s},\mathbf{v})$ represents a reflectance (or scattering) function and $\Phi$ the incident flux. Let us introduce the hemispheric albedo $A_H$ by the relation (see [Breiter et al., 2007]):

$$A_H(\cos\theta_0) = \frac{1}{\Phi\ \cos\theta_0} \int_{\phi=0}^{2\pi} \int_{\theta=0}^{\pi/2} I_R(\mathbf{s},\mathbf{v})\ \mathbf{v}\ \sin\theta\, d\theta\, d\phi\, dS\,, \tag{2.2}$$

where $\cos\theta_0 = \mathbf{s}\cdot\mathbf{n}$. The recoil force acting on the surface element $dS$ is given by

$$d\mathbf{f}_R = -\frac{1}{c} \int_{\phi=0}^{2\pi} \int_{\theta=0}^{\pi/2} I_R(\mathbf{s},\mathbf{v})\ \mathbf{v}\ \cos\theta\ \sin\theta\, d\theta\ d\phi\ dS\,. \tag{2.3}$$

Assuming Lambert's law of diffuse reflection, we can express the intensity of the reflected radiation as (e.g. [Breiter et al., 2007]):

$$I_R = A\Phi\frac{\mathbf{s}\cdot\mathbf{n}}{\pi}\,, \tag{2.4}$$

where $A = const.$ With this approximation (which has been used in the whole text), the resulting force acting on $dS$ reads

$$d\mathbf{f}_R = -\frac{2A\Phi}{3c}\,\mathbf{s}\cdot\mathbf{n}\,\mathbf{n}\,dS\,. \tag{2.5}$$

Integrating (2.5) over the surface $\Sigma$ of an asteroid we obtain the whole recoil force arising from reflected radiation:

$$\mathbf{f}_R = \int_\Sigma d\mathbf{f}_R\,.$$

Under normal circumstances, this force is not able to change the orbit of a body on a long time scale (like the force caused by direct radiation). On contrary, the torque

$$\mathbf{T}_R = \int_\Sigma \mathbf{r}\times d\mathbf{f}_R \tag{2.6}$$

of this reflected-radiation force does not vanish and it is able to change the rotation of the body. In fact it is equal to the YORP with the assumption of zero thermal conductivity multiplied by a factor $A/(1-A)$. For bodies with higher albedo, such as the E-type asteroids, it is necessary to take this reflected-radiation torque into account.

## 2.3 Thermal radiation

Assuming isotropic emission, the intensity of a black body radiation can be expressed by Stephan-Boltzmann's law:

$$B(\mathbf{v}) = \frac{\epsilon\sigma T^4}{\pi}\,, \tag{2.7}$$

where $\sigma = 5.67051 \times 10^{-8}$ W/m$^2$/K$^4$ is the Stephan-Boltzmann constant, $\epsilon$ the emisivity and $T$ is the temperature. Similarly as in Section 2.2, the recoil force due to the thermal radiation can be expressed as

$$d\mathbf{f}_{\rm th} = -\frac{1}{c}\int_{\phi=0}^{2\pi}\int_{\theta=0}^{\pi/2} B(\mathbf{v})\ \mathbf{v}\ \cos\theta\ \sin\theta\, d\theta\ d\phi\ dS\,, \tag{2.8}$$

which is equal to

$$d\mathbf{f}_{\rm th} = -\frac{2}{3}\frac{\epsilon\sigma T^4}{c}\mathbf{n}\, dS\,, \tag{2.9}$$

In the case of zero thermal conductivity (K=0), all absorbed solar energy is immediately re-radiated and the resulting force on a non-shadowed facet can be expressed as

$$d\mathbf{f}_{\rm th}^{K=0} = -\frac{2(1-A)\Phi}{3c}\,\mathbf{s}\cdot\mathbf{n}\,\mathbf{n}\, dS\,. \tag{2.10}$$

For a shadowed facet $d\mathbf{f}_{\rm th}^{K=0} = \mathbf{0}$. In reality, even shadowed facets experience thermal recoil force because their temperatures $T$ are not zero, but this needs to be determined using heat diffusion in the body.

The total thermal force acting on the asteroid is given by an integration of (2.9) over asteroid's surface:

$$\mathbf{f}_{\rm th} = \int_\Sigma d\mathbf{f}_{\rm th}\,. \tag{2.11}$$

This represents the thermal (Yarkovsky) force. It is able to secularly change the semimajor axis of an asteroid's orbit. This effect arises from an anisotropic temperature distribution (due to the finite thermal inertia) across the surface[2]. The precise knowledge of the surface temperature $T$ is necessary (see Appendix A).

The total thermal torque acting on the asteroid is given by integration over it's surface:

$$\mathbf{T}_{\rm th} = \int_\Sigma \mathbf{r}\times d\mathbf{f}_{\rm th}\,. \tag{2.12}$$

This thermal torque (or the YORP torque, Chapter 3) is able to change the spin rate and obliquity of the body. The main difference between the YORP and the Yarkovsky effect is that the YORP is strongly dependent on the shape of an asteroid (it affects only bodies with a certain amount of "windmill" asymmetry[3]). The Yarkovsky effect is nonzero for rotating sphere but vanishes for zero thermal inertia. On the other hand, the YORP effect is nonzero even for a vanishing thermal conductivity (i.e., without any thermal lag).

[2]The thermal emission from irregularly shaped surface with zero thermal inertia is not able to change the orbit on a long scale.

[3]For example, it does not affect spheroids [Breiter et al., 2007].

**Isothermal body**

Our numerical results show that $\mathbf{f}_{\mathrm{th}} = 0$ and $\mathbf{T}_{\mathrm{th}} = 0$ for an isothermal body of an arbitrary shape. This is in accordance with an intuition but we shall prove it in a rigorous way. Let us recall *Gauss' theorem* in vector analysis:

$$\oint_{\Sigma} \mathbf{a} \cdot d\mathbf{S} = \int_{V} \nabla \cdot \mathbf{a} \, dV \,, \tag{2.13}$$

where the first integral is over the closed surface $\Sigma$, the second over the corresponding enclosed volume $V$, $\mathbf{a}$ represents a general vector field. The Gauss' theorem gives rise to the following identities (e.g. [Sedlák and Štoll, 1993]):

$$\oint_{\Sigma} b \, d\mathbf{S} = \int_{V} \nabla b \, dV \,, \tag{2.14}$$

$$\oint_{\Sigma} d\mathbf{S} \times \mathbf{a} = \int_{V} \nabla \times \mathbf{a} \, dV \,, \tag{2.15}$$

where $b$ is a general scalar field.

Let $T_c$ be a constant temperature of the body. The total thermal force is

$$\mathbf{f}_{\mathrm{th}} = -\frac{2}{3}\frac{\epsilon\sigma}{c} \oint_{\Sigma} T_c^4 \, d\mathbf{S} = -\frac{2}{3}\frac{\epsilon\sigma}{c} \int_{V} \nabla \left(T_c^4\right) \, dV = 0 \,. \tag{2.16}$$

Here we used Equations (2.9), (2.11), (2.14) and the assumption of the constant temperature $T_c$ (i.e., $\nabla T_c = 0$). Similarly, the thermal torque can be expressed as

$$\mathbf{T}_{\mathrm{th}} = -\frac{2}{3}\frac{\epsilon\sigma}{c} T_c^4 \oint_{\Sigma} \mathbf{r} \times d\mathbf{S} = \frac{2}{3}\frac{\epsilon\sigma}{c} T_c^4 \int_{V} \nabla \times \mathbf{r} \, dV = 0 \,. \tag{2.17}$$

Here we used Equations (2.9), (2.12), (2.15) and the well-known relation $\nabla \times \mathbf{r} = 0$. We can see clearly, that neither thermal force nor thermal torque affect a body with a constant temperature.

## 2.4 Example: (1620) Geographos

Here we shall demonstrate the effect of the direct, reflected and thermal radiation on the asteroid (1620) Geographos. We assumed the following orbital parameters: semimajor axis $a = 1.24547\,\mathrm{AU}$, eccentricity $e = 0.3354$, inclination $i = 13.34°$, argument of perihelion $\omega = 277.8°$, longitude of ascending node $\Omega = 337.3°$ and the pole of rotation $\lambda = 55°$, $\beta = -46°$. The rotation period is $P = 5.22484\,\mathrm{hours}$. We used the density of surface layers $\rho_s = 1.7\,\mathrm{g/cm^3}$, the bulk density $\rho_b = 2.5\,\mathrm{g/cm^3}$, the thermal conductivity $K = 0.02\,\mathrm{W/m/K}$, the thermal capacity $c = 680\,\mathrm{J/kg/K}$ and the Bond albedo 0.2. The shape was represented by a polyhedron with 4092 surface triangular facets according to [Hudson and Ostro, 1999]. (See also Appendix D.) We used a numerical one-level scheme (see Appendix A) to model forces and torques corresponding to the direct, reflected and thermal radiation.

The magnitude of radiative acceleration can be seen in Figure 2.3. The left plot shows perturbations of the semimajor axis $da/dt$ of the orbit during first 12 hours after the perihelion

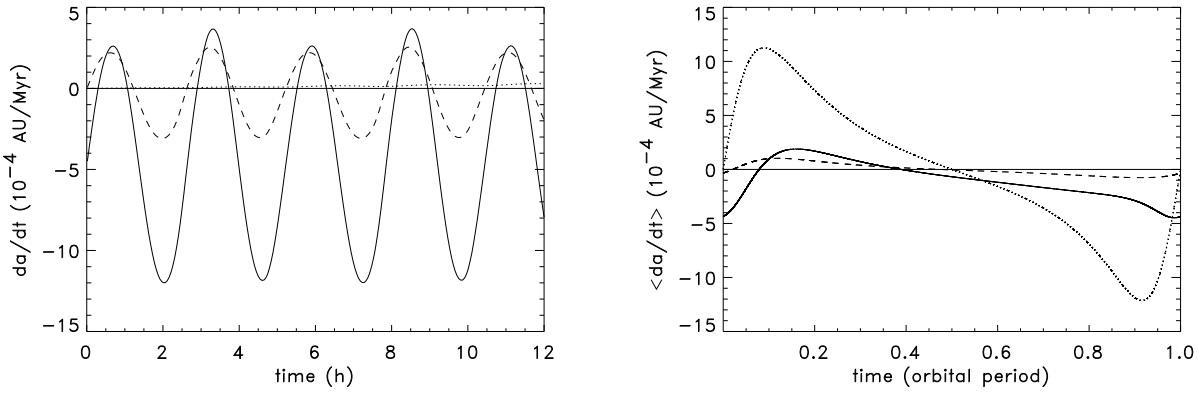


Figure 2.3: Perturbations of semimajor axis by the thermal radiation (solid curve), reflected radiation (dashed curve) and direct radiation (dotted). Left: Perturbations during the first 12 hours after passage of perihelion. Right: Perturbations averaged over spin period during one revolution about the Sun. The perihelion passage corresponds to $t = 0$. The orbit-averaged value of the semimajor axis drift $\langle da/dt \rangle$ produced by direct and reflected radiation is zero, but thermally induced $\langle da/dt \rangle = -1.26 \times 10^{-4}$ AU/Myr.

passage and the right one shows these perturbations averaged over spin periods during one whole revolution about the Sun.

The thermal acceleration is able to secularly change semimajor axis by a mean (i.e. orbit-averaged) rate $\langle da/dt \rangle = -1.26 \times 10^{-4}$ AU/Myr. The variations caused by this force are shifted with respect to the variations produced by the reflected radiation due to finite thermal inertia. The reflected radiation is able to produce short-term perturbations but their orbit-averaged value is zero (the actual value $\sim 10^{-7}$ AU/Myr is due to minor numerical inaccuracies in our model). Perturbations of semimajor axis produced by direct radiation are precisely symmetric with respect to the perihelion. They can be the largest for a short term but their orbit-averaged effect is also zero ($\sim 10^{-8}$ AU/Myr due to numerical round-off errors).

We demonstrate how the radiative torques affect the spin rate in Figure 2.4. The left plot shows perturbations of the spin rate $d\omega/dt$ during 12 hours after passage of perihelion while the right one shows the perturbations averaged over the spin period during the whole revolution about the Sun.

The thermal torque produces both short-term and long-term perturbations of the spin rate, with the orbit-averaged value $\sim 2.4 \times 10^{-19}\,\mathrm{s}^{-2}$. These perturbations are somewhat shifted with respect to the perturbations produced by reflected radiation which has a smaller amplitude. The value of the orbit-averaged perturbations of reflected radiation is $\sim 6 \times 10^{-20}\,\mathrm{s}^{-2}$. The direct radiation produces only short-term variations of the spin rate, but the orbit-averaged value is zero ($\sim 10^{-21}\,\mathrm{s}^{-2}$ due to numerical inaccuracies).

Note the resulting torque strongly depends on the shape model. See Section 3.4.2.

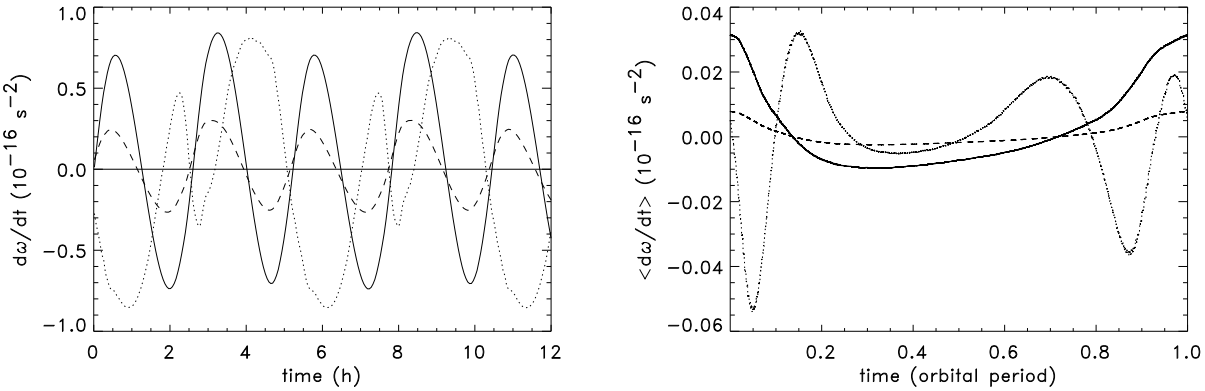


Figure 2.4: Perturbations of the spin rate $d\omega/dt$ by the thermal radiation (solid curve), reflected radiation (dashed curve) and direct radiation (dotted curve). Left: The perturbations during the first 12 hours after passage of perihelion. Right: The perturbations averaged over the spin period during one revolution about the Sun. The perihelion passage corresponds to $t = 0$. The orbit-averaged value of perturbations of spin rate $\langle d\omega/dt \rangle$ produced by direct radiation is zero, but thermally induced $\langle d\omega/dt \rangle = 2.4 \times 10^{-19}$ s$^{-2}$.

# Chapter 3

# The YORP effect

## 3.1 Introduction

The rotation of small asteroids or meteoroids is modified especially by mutual collisions with other small solar system bodies [Farinella et al., 1992] and by solar and planetary tides. Moreover, a dissipation of free-precession energy inside larger bodies (which are though to be rubble piles) causes a principal-axis rotation [Burns and Safronov, 1973], [Efroimsky and Lazarian, 2000].

Aditionally, there are several non-gravitational effects caused by absorption, reflection or reemission of the solar radiation, that can also change rotation. For example [Radzievskii, 1954] showed that small ($\sim$ cm) body with a realistic albedo distribution across the surface can be spun up by solar radiation to the disruption limit on a time scale of thousand years. [Paddack, 1969] studied a possibility of destruction of small meteoroids and tektites due to the rotational fission. His "windmill effect" is due to the reflection of sunlight from surface of body with an appropriate shape. He estimated this effect is able to spin up a several cm long body, composed from tektite glass, to the bursting limit in about 60 000 years.

**General properties of the YORP effect.** Recently, [Rubincam, 2000] investigated spinning up and down of small asteroids due to the infrared emission from their irregularly shaped surfaces. He named this phenomenon the YORP effect as an acronym of Yarkovsky–O'Keefe–Radzievskii–Paddack (four names of planetary scientists). Rubincam computed thermal torques on bodies that were assumed to be (i) blackbodies with (ii) zero thermal conductivity on (iii) circular orbits around the Sun and (iv) rotating about the principal axis of inertia tensor. Their shapes were described by (v) spherical harmonic expansion of the shapes of real asteroids. Rubincam showed there are two important components of the YORP torque. The first one is able to change the rotation rate and the second one the obliquity of the asteroid. Both components depend on the obliquity. Rubincam's conclusions are: (a) The YORP effect is able to spin up or spin down an asteroid with 5-km radius during $10^8$ years. (b) The YORP effect dominates collisions in the inner Solar System for bodies with radius $R$ smaller than 5 km and it dominates tidal encounters for bodies with $R < 1$ km. (c) The YORP may be responsible for the observed excess of slow and fast rotators among small asteroids. (d) Due to inevitable interplay between the torque affecting rotation rate and torque affecting obliquity, a rotational bursting due to the YORP effect actually happens very rarely. (e) The YORP effect may explain rotation states of several NEAs.

[Vokrouhlický and Čapek, 2002] studied the YORP effect on 10 shapes of real bodies (8 asteroids and Phobos and Deimos) and also on a sample of 500 automatically generated shapes corresponding to small Solar System bodies. They assumed the Rubincam's approximation[1]

[1] i.e., asteroids are blackbodies with zero thermal conductivity on circular orbits around the Sun and rotating

but used polyhedral description of shapes of asteroids instead. They classified the bodies into four classes according to the dependance of the YORP effect on the obliquity. Most often the obliquity is slowly driven to $0°/180°$ or $90°$ and the rotation is asymptotically decelerated. Only a minority of the bodies is asymptotically accelerated. They also present several examples of the spin-state evolution due to the YORP effect where also gravitational torques due to the Sun and gravitational perturbations of the orbit by planets play an important role. They realized the YORP effect may be important for driving the rotation into resonances between the precession of the spin axis due to the solar torques and the precession of the orbital plane by planetary perturbations. In the case of small members of the Themis family, the evolution due to the YORP alone describes the evolution quite well whereas in the case of Flora family asteroids the evolution of rotation is usually much more complicated.

[Čapek and Vokrouhlický, 2004] analyzed the influence of the surface thermal conductivity $K$ both on a sample of artificial shapes and on several real bodies for which the possibilities of the YORP detection were also discussed. They found, unlike in the zero conductivity model, the YORP effect preferentially drives the spin axis to be perpendicular to the orbital plane (i.e., the obliquity $0°$ or $180°$) for the realistic values of $K$. They also found a nearly complete independence of the YORP component affecting the spin rate on surface thermal conductivity. They showed that asymptotical spinning up and down are equally likely and (unlike the results of [Rubincam, 2000]) the rotational bursting due to the YORP effect can be relatively common.

[Vokrouhlický et al., 2007] eliminated the principal axis rotation constraint used in previous studies and numerically integrated Euler's equations for several bodies. They found several new asymptotic states and analytically proved an onset of the tumbling caused by the YORP instead of slow-rotation asymptotic state.

[Scheeres, 2007] derived linearized analytical equations describing evolution of spin rate and obliquity of uniformly rotating asteroids due to YORP effect. (Non-zero thermal inertia was involved by simplified "thermal lag".) He also introduced several dimensionless parameters dependent only on the shape and mass distribution across the body, which describe the strength of YORP effect. He was able to analytically confirm a lot of results on general YORP properties obtained previously by numerical studies.

[Breiter et al., 2007] derived an analytical expression for the YORP torque acting on spheroids and proved the YORP does not contribute to the long-term evolution of their rotation.

**The observation of the YORP effect in the Solar System.** [Slivan, 2002] photometrically observed rotation of several Koronis family members and found a surprising anisotropy of their spin axes distribution. The prograde rotators have spin periods between 7.5 and 9.5 hours and obliquities $42° - 50°$. On the other hand, spin periods of retrograde rotators are $< 5$ h or $> 13$ h and their obliquities are $\geq 154°$. Moreover, he found the longitudes of spin axes are clustered. Such distribution can not be explained by mutual collisions.

[Vokrouhlický et al., 2003] succeded to explain the non-random distribution of the obliquities and spin periods of the Koronis family asteroids as a consequence of the YORP effect. They used a numerical model involving torques produced by reflected and thermal radiation as well as gravitational effects of the Sun and planets. With a wide range of initial conditions (shapes, spin periods and obliquities) they reproduced the observed distribution of the spin axes. [Vokrouhlický et al., 2003] found that the $s_6$ spin – orbit resonance is important for the prograde rotators resulting in the capture of the spin axes longitudes. Their research showed the YORP effect may be more important to changing rotation state than collisions for bodies $< 40$ km in diameter.

[Vokrouhlický et al., 2004] investigated a possibility of direct detection of the YORP effect

about the principal axis of the inertia tensor.

on the asteroid (25143) Itokawa by precise measurement of its rotation period or rotation phase. They used a generalized model of the YORP effect, taking into account a finite thermal conductivity of asteroid's surface, actual elliptical orbit and proper spin axis orientation. They predicted an observable $1-3$ hr delay of the lightcurve maximum in January, 2004. Unfortunately their results were incorrect due to aninaccurate shape model and some other mistakes also (see Section 3.4.2).

[Scheeres et al., 2007] used a more precise shape, rotation pole and mass of Itokawa, determined by the Hayabusa mission ([Demura et al., 2006], [Gaskell et al., 2006], [Saito et al., 2006]), and calculated how the YORP affects the asteroid's rotation rate. They found Itokawa's rotation is decelerated so that doubling time is 50 000 – 90 000 years (see Equation (3.10)). They predict the detection of the YORP effect for Itokawa during future apparitions. They also discussed the distant-past rotation history of Itokawa and concluded, Itokawa's rotation was accelerated. 100 – 180 Myr ago, spin period of Itokawa reached 6.5 hours, corresponding to the bursting limit. Then the shape had been changed to the present state and it has been decelerated since that time (However, they noticed the possibility that Itokawa had a close approach with the Earth during this period, which could also change it's shape.)

Recently, the YORP effect was directly detected for small ($\sim$ 57 m) near-Earth asteroid (54509) 2000 PH5 ([Lowry et al., 2007], [Taylor et al., 2007]). The acceleration of rotation $(2.0\pm 0.2)\times 10^{-4}$ deg/day$^2$ was determined from radar and lightcurve data. This value corresponds to the theoretical prediction by the YORP model calculated for the shape of (54509) 2000 PH5, simultaneously determined by photometry and radar.

In the same time, [Kaasalainen et al., 2007] analyzed (1862) Apollo's photometric observations from 1980 to 2005. These authors concluded that Apollo's spin behaviour is not consistent with the assumption of a constant period of rotation. They found a change angular velocity $d\omega/dt = (5.3 \pm 1.3)\times 10^{-8}$ rad/day$^2$. For the shape determined by photometry they calculated corresponding YORP effect and found that it is consistent with observed $d\omega/dt$, such that they interpret acceleration of Apollo's rotation rate by effects of YORP.

Here we shall present some of our results concerning the YORP effect. In Section 3.2 we derive expressions of YORP evolution of asteroid's rotational state. Basic facts concerning YORP effect are demonstrated on a simple example in Section 3.2.1. Following Section 3.3 is devoted to study of YORP effect on large sample of artificial bodies. Section 3.3.1 is based on our paper [Vokrouhlický and Čapek, 2002] and describes YORP dependence on obliquity, while 3.3.2 is based on [Čapek and Vokrouhlický, 2004] and deals with the thermal conductivity dependence of YORP. The YORP effect on the real asteroids is presented in 3.4, which is based on [Čapek and Vokrouhlický, 2004]. In the case of asteroid Itokawa we corrected our results from [Vokrouhlický et al., 2004].

## 3.2 Theory of the YORP effect

The YORP effect changes spin state of an irregularly shaped body due to the thermal torque. This torque is caused by a recoil force due to thermal emission from surface, heated by absorption of sunlight. The thermal torque was expressed in previous chapter by Equation (2.12). The torque arising from *the reflected radiation* also contributes to the total torque (see Section 2.2). The torque $\mathbf{T}$ changes the angular momentum $\mathbf{L}$ of the body (with respect to the inertial frame) according to the relation

$$\frac{d\mathbf{L}}{dt} = \mathbf{T}, \tag{3.1}$$

If we assume that dissipation of the rotation energy inside the body is so rapid, that any non-principal axis rotation is quickly damped and thus the body rotates around the shortest axis

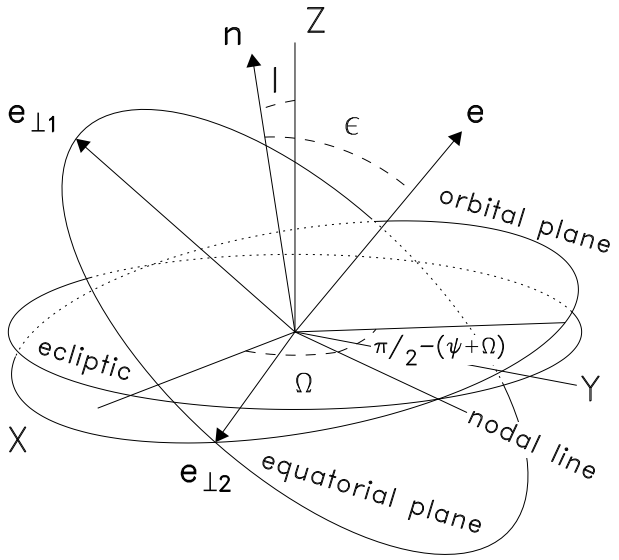


Figure 3.1: Three coordinate systems: *Ecliptical system* $(X - Y - Z)$ defined bythe plane of ecliptic and the vernal equinox $X$, *the orbital system* defined by orbital plane and perihelion and finally *the equatorial system* defined by the base vectors $\mathbf{e}_{\perp 1}$, $\mathbf{e}_{\perp 2}$ (the intersection of the equatorial and the orbital plane) and $\mathbf{e}$ (parallel with the spin vector).

of the inertia tensor (corresponding the moment of inertia $C$), the angular momentum will be simply

$$\mathbf{L} = C\omega\mathbf{e}, \tag{3.2}$$

where $\omega$ denotes the angular velocity and $\mathbf{e}$ corresponds to the unit vector of the spin axis. This together with (3.1) leads to the expression

$$\frac{d\omega}{dt}\mathbf{e} + \frac{\mathbf{e}}{dt}\omega = \frac{\mathbf{T}}{C}, \tag{3.3}$$

The scalar product of this equation with the vector $\mathbf{e}$ allows us to express the change of the angular velocity due to the torque[2]:

$$\frac{d\omega}{dt} = \frac{\mathbf{T}\cdot\mathbf{e}}{C} = \frac{T_\omega}{C} \tag{3.4}$$

Substituting (3.4) back into (3.3), we obtain the expression for the change of the spin axis direction:

$$\frac{d\mathbf{e}}{dt} = \frac{\mathbf{T} - (\mathbf{T}\cdot\mathbf{e})\mathbf{e}}{C\omega}. \tag{3.5}$$

The spin vector direction $\mathbf{e}$ is usually characterized by the obliquity $\epsilon$ which is the angle between the spin vector and the normal to the orbital plane, and by the precession angle in longitude $\psi$. The components of the unit vector $\mathbf{e}$ with respect to the inertial system connected with the orbital plane of the body, where $x-$ axis corresponds to the nodal line (see Fig. 3.1), are

[2]Here we use that $\dot{\mathbf{e}}\cdot\mathbf{e} = 0$, because $d(\mathbf{e}\cdot\mathbf{e})/dt = 2\dot{\mathbf{e}}\,\mathbf{e}$ and $\mathbf{e}\cdot\mathbf{e} = \mathbf{1}$.

$\mathbf{e} = (\sin\epsilon\sin(\psi+\Omega), \sin\epsilon\cos(\psi+\Omega), \cos\epsilon)$. The scalar product of (3.5) and the unit vector $\mathbf{N}$, perpendicular to the orbit of the body, leads to the expression for the change rate of the obliquity $\epsilon$:

$$\frac{d\epsilon}{dt} = \frac{\mathbf{T}\cdot\mathbf{e}_{\perp 1}}{C\omega} = \frac{T_\epsilon}{C\omega}, \tag{3.6}$$

where

$$\mathbf{e}_{\perp 1} = \frac{(\mathbf{N}\cdot\mathbf{e})\mathbf{e} - \mathbf{N}}{\sin\epsilon}. \tag{3.7}$$

The rate of change of the precession angle $\psi$ can be derived by a cross product of Equation (3.5) and the vector $\mathbf{N}$. After some algebra we have

$$\frac{d\psi}{dt} = \frac{\mathbf{T}\cdot\mathbf{e}_{\perp 2}}{C\omega} = \frac{T_\psi}{C\omega}, \tag{3.8}$$

where

$$\mathbf{e}_{\perp 2} = \frac{\mathbf{N}\times\mathbf{e}}{\sin\epsilon}. \tag{3.9}$$

So, the thermal torque $\mathbf{T}$ has three components $(T_\epsilon, T_\psi, T_\omega)$ with respect to the system $(\mathbf{e}_{\perp 1}, \mathbf{e}_{\perp 2}, \mathbf{e})$ which change the obliquity, the angle of precession and the angular velocity.

**Useful quantities**

The characteristic timescale of the YORP-driven evolution of the rotation rate can be described by the quantity called *doubling time* [Rubincam, 2000]:

$$t_d = \frac{\omega}{\langle\dot{\omega}\rangle} = \frac{C\omega}{\langle T_\omega\rangle}. \tag{3.10}$$

After the time $t_d$ the YORP effect increases the rotation rate $\omega$ twice or decrease it to the half value. This is because $\omega(t)$ is quasilinear in time.

The quantity describing the windmill asymmetry - *windmill factor* - of the given shape can be defined as

$$\varphi_w = \frac{1}{2}\left(-1 + \sqrt{1 + \frac{2\,\pi\,(2+\sqrt{2})}{V}\,\mathbf{e}\cdot\int_{\phi=0}^{2\pi}\int_{\Sigma}\delta(\mathbf{r},\mathbf{s},\Sigma)\;\mathbf{r}\times\mathbf{s}\cdot\mathbf{n}\mathbf{n}\;dS\,d\phi}\right), \tag{3.11}$$

where $V$ denotes volume of the body, $\mathbf{e}$ the unit vector of the spin axis, $\mathbf{r}$ the position vector of the surface element $dS$, $\mathbf{n}$ the outer unit normal of $dS$ and $\mathbf{s}$ the unit vector perpendicular to spin axis. (In the body-fixed frame it can be expressed as $\mathbf{s} = (\cos\phi, \sin\phi, 0)$.) The integration is realized over the surface $\Sigma$ of the body and over one revolution of $\mathbf{s}$ about the spin axis. The "mutual shadowing" function $\delta(\mathbf{r},\mathbf{s},\Sigma)$ is equal to 1 if half-line starting at $\mathbf{r}$ and propagating in the direction $\mathbf{s}$ does not intersects the surface $\Sigma$ and it is equal to 0 in the opposite case.

This expression is established on the basis of computing the YORP effect for a simple body composed of cylinder with two wedges, as described in following Section 3.2.1. The windmill

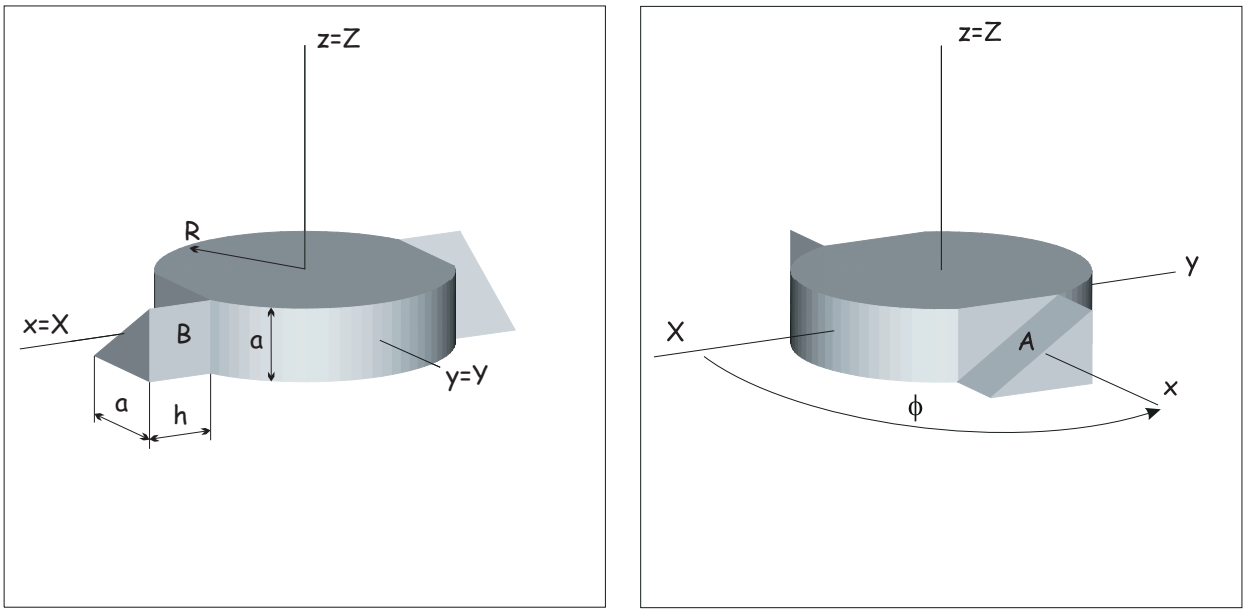


Figure 3.2: A simple test body. The small letters denote the axes of the body-fixed frame, while the capital letters the inertial frame. The facets causing the non-zero torques are denoted by "A" and "B" and $\phi$ represents the angle of rotation about $Z$-axis.

factor is a dimensionless parameter and it depends only on the shape of the body. In reality it has value approximately from $-0.15$ to 0.15, but most frequently for usual asteroid-like shapes, the absolute value $|\varphi|$ is about 0.015. The positive value indicates spinning up of the body and the negative value indicates spinning down.

There is a simple relationship between the windmill factor $\varphi_w$ and the mean change of the angular velocity caused by the YORP effect, under the assumption of a circular orbit, zero thermal conductivity $K$, zero albedo $A$ and zero obliquity $\epsilon$:

$$\langle \dot{\omega} \rangle = -\frac{2(2-\sqrt{2})}{3\pi c} \frac{\Phi}{d^2} \frac{\varphi_w (1+\varphi_w)}{\rho} \frac{m}{C}, \tag{3.12}$$

where $\Phi$ is the solar flux at the heliocentric distance $d$, $\rho$ is the bulk density of the asteroid and $m$ its mass.

### 3.2.1 The YORP effect on a windmill shape

Here we shall explain the basic YORP efect properties, using an example of the artificial body shown in Figure 3.2. It is composed from a cylinder with two wedges. This body rotates about the $z$-axis and the Sun shines from the $X-$axis direction. At first, we express the thermal torque acting on arbitrary surface element. Let us suppose that all incoming radiation is immediately re-radiated as a thermal radiation. This means there is no thermal conductivity of the surface material, no thermal lag. Assuming the thermal emission obeys Lambert's law, the thermal radiation pressure acting on $i$-th surface element $\mathbf{S}^i$ causes the force

$$\mathbf{f}^i = -\frac{2E^i}{3c}\mathbf{S}^i,$$

where $E^i$ is the incomming solar energy (W/m$^2$) and $c$ the speed of light. This force acting on the arm $\mathbf{r}^i$ results in a torque

$$\mathbf{T}^i = \mathbf{r}^i \times \mathbf{f}^i.$$

The whole thermal torque acting on the body is the sum over all its surface elements:

$$\mathbf{T} = \sum_i \mathbf{T}^i.$$

The mean change of the angular speed $\omega$ over the time is given by

$$\langle \dot{\omega} \rangle = \frac{1}{C} \langle T_z \rangle,$$

where $C$ is the principal moment of inertia around the spin axis and $\langle T_z \rangle = \int_0^P T_z \, dt \, / \, P$ denotes mean $z-$component of the thermal torque $\mathbf{T}$.

Let us now compute the thermal torques applied on the windmill from Figure 3.2. The jacket of the cylinder as well as its bases do not cause any torque, because any force acting on each facet has a zero arm. The only facets that can cause a thermal torque are the inclined facets denoted by $A$ and the facets perpendicular to the $xy-$plane denoted by $B$. These facets have the outer normals

$$\mathbf{n}^A = \frac{1}{\sqrt{2}} \begin{pmatrix} -\sin\phi \\ \cos\phi \\ 1 \end{pmatrix}, \qquad \mathbf{n}^B = \begin{pmatrix} \sin\phi \\ -\cos\phi \\ 0 \end{pmatrix},$$

the area $S^A = ah\sqrt{2}$, $S^B = ah$ and the arms

$$\mathbf{r}^A = \mathbf{r}^B = \frac{R+h}{2} \begin{pmatrix} \cos\phi \\ \sin\phi \\ 0 \end{pmatrix}.$$

The incomming solar energy (neglecting mutual shadowing) can be expressed as

$$E^A = \begin{cases} 0, & \phi \in \langle 0, \pi \rangle \\ \Phi \, S^A \, \mathbf{n}^A \cdot \mathbf{s}, & \phi \in \langle \pi, 2\pi \rangle, \end{cases} \qquad E^B = \begin{cases} \Phi \, S^B \, \mathbf{n}^B \cdot \mathbf{s}, & \phi \in \langle 0, \pi \rangle, \\ 0, & \phi \in \langle \pi, 2\pi \rangle \end{cases}$$

where $\Phi$ is the solar flux at the asteroid's orbit and $\mathbf{s} = (1, 0, 0)$ is the direction toward the Sun. Putting all these facts together we obtain a mean torque caused by one wedge:

$$\langle \tau_z \rangle = \frac{2 - \sqrt{2}}{3c} \Phi \, ah(R + h).$$

The principal moment of inertia can be approximated by the moment of inertia of the cylinder part of the body:

$$C = \frac{1}{2} (\pi R^2 a \rho) R^2.$$

Finally, the mean change of the angular velocity caused by the two wedges can be expressed as

$$\langle \dot{\omega} \rangle = -\frac{4(2 - \sqrt{2})}{3\pi c} \frac{\Phi_0}{d^2} \frac{\varphi_w (1 + \varphi_w)}{\rho R^2}, \tag{3.13}$$

where $\Phi_0 = 1366 \, \mathrm{W/m^2}$ is the solar flux at 1 AU, $d$ is semimajor axis of the orbit (in AU units) and $\varphi_w$ the dimensional-less windmill factor, which can be expressed as $\varphi_w = h/R$ in this simple case.

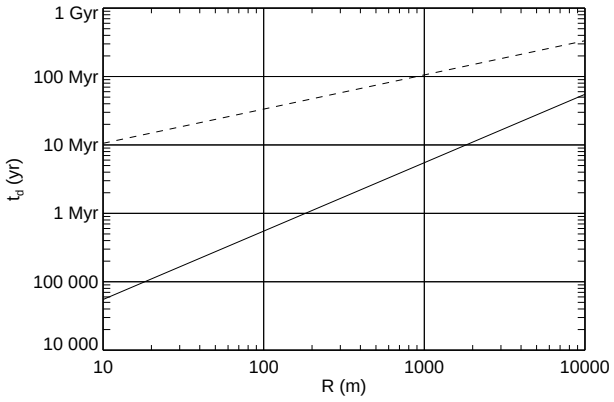


Figure 3.3: Doubling time for the body from Figure 3.2 as a function of radius of the body. The solid line corresponds to time necessary for double the rotation period due to YORP effect for body with windmill factor $\varphi_w = 0.014$, bulk density $\rho = 2.5\,\mathrm{g/cm^3}$ and orbit with semimajor axis $d = 2.5\,\mathrm{AU}$. Period of rotation is assumed $P[\mathrm{hr}] = 0.01R[\mathrm{m}]$. Dashed line describes timescale corresponding to reorientation of the spin axis due to collisions in the Main Belt.

Let us now estimate a characteristic timescale of the YORP acting on the body. Using (3.13) and (3.10) the doubling time is:

$$t_d = 0.05\,\mathrm{yr}\,\frac{1}{\varphi_w(1+\varphi_w)}\left(\frac{1\,\mathrm{hr}}{P}\right)\left(\frac{d}{1\,\mathrm{AU}}\right)^2\left(\frac{\rho}{1\,\mathrm{g/cm^3}}\right)\left(\frac{R}{1\,\mathrm{m}}\right)^2 \tag{3.14}$$

We can see the dependence of the doubling time on the radius of the body in Figure 3.3. We used Equation (3.14) and assumed windmill factor[3] $\varphi_w = 0.014$, period of rotation $P[\mathrm{hr}] = 0.01R[\mathrm{m}]$ and bulk density $\rho = 2.5\,\mathrm{g/cm^3}$. The solid line corresponds to the semimajor axis $d = 2.5\,\mathrm{AU}$. Dashed line denotes the timescale $t_{col}$ corresponding to complete change of the spin axis due to collisions according to [Farinella et al., 1998]:

$$t_{col} = 3.34 \times 10^6\,\mathrm{yr}\left(\frac{R}{1\mathrm{m}}\right).$$

In the radius interval from 10 meters to 10 km, the YORP doubling time is smaller than typical collisional reorientation time. Then the YORP effect predominates the collisions in the evolution of spin axes for the bodies with assumed properties in the Main Belt.

Though expression (3.13) was derived for the body and situation described above, it can be generalized and we can summarize the YORP effect dependance on several parameters:

- Our first simple model (i.e., the equation describing the long term evolution of the rotation state) is valid only for bodies with sufficiently fast rotation which is strong enough to damp any deviations from principal axis rotation via inelastic dissipation of energy inside the body [Efroimsky and Lazarian, 2000]. If the spin period increases up to several hundreds hours, the asteroid begins to tumble and the approach used here is unreliable. This slow rotation limit has been studied by [Vokrouhlický et al., 2007].

- The shape is the key property affecting the YORP effect. There are no thermal torques acting on spheres, triaxial ellipsoids or other bodies with lack of "windmill asymmetry" (The analytical proof can be found in [Breiter et al., 2007].) It can be roughly described by the windmill factor $\varphi_w$.

[3] The main belt asteroids have $\langle|\varphi_w|\rangle \simeq 0.015$.

- The YORP (i.e., mean change of angular velocity) decreases with square of the size of an asteroid $\propto 1/R^2$. It is important only for bodies smaller than, say $\sim 10\,\mathrm{km}$ in diameter[4]
- The shape of the orbit, especially the semimajor axis is important. The YORP decrease with square of the distace from the Sun $\propto 1/d^2$.
- The YORP decreases with the bulk density of the body as $1/\rho$.

This simple model does not describe the dependence of the YORP effect on mutual position of the spin axis and the orbital position of the spin axis and the orbital plane, and also on thermal behaviour of the surface material. The dependence of the YORP effect on these quantities is discussed in Section 3.3

[4]On the other hand, the dissipation of the free-rotation energy does not operate for very small bodies and moreover the temperature differences between the insolated and shadowed facets are minimal due to fast rotation and effective heat transfer through the body. These facts are not included in this simple model.

## 3.3 Statistical study of the YORP effect

Here we shall demonstrate the diversity of the YORP results with respect to various parameters. By computing the YORP torqe on several asteroids with known shapes we can conclude that the shape of the body is the most important characteristic that determines the overall effect. Since the YORP depends sensitively on shape, we decided to study this effect on a large sample of Gaussian random spheres that sufficiently describe the shape characteristics of small asteroids in the Main Belt (see Appendix C).

We use a polyhedral description of shapes which consists of a list of surface vertices and their mutual identifications as triangular facets. This description allows us to determine the volume, inertia tensor, surface area and self-shadowing of the surface in a simple way (see Appendix B).

We are interested in the long-term evolution of the spin state. Hence we discuss the torques $\langle T_\epsilon \rangle$ and $\langle T_\omega \rangle$ averaged over rotation and revolution cycles.

### 3.3.1 Obliquity dependence – the YORP classification

*This section is based on [Vokrouhlický and Čapek, 2002]*

A study of the dependence of the YORP on obliquity was performed for 500 Gaussian random spheres orbiting on a circle with radius 2.5 AU. All bodies rotated about the shortest axis of inertia tensor with a period $P = 6$ hr. The bulk density was $\rho_{\rm bulk} = 2.5\,{\rm g/cm}^3$ and the volume corresponding to the sphere with radius 1 km. The surface thermal conductivity was assumed $K = 0$ and albedo $A = 0$. For each value of the obliquity ($\epsilon$ goes from $0^\circ$ to $180^\circ$ with a $30^\circ$ step) the thermal force causing the YORP torque was determined according to (2.10) for all surface facets in 250 000 points during the orbital period. The final YORP torque was given by a sum over the whole body's surface (2.12) and an averaging along the orbit.

According to the dependence of the YORP component $\langle T_\epsilon \rangle$ on obliquity $\epsilon$ we can distinguish four principal types. Their description follows. We also attempt to illustrate a typical evolution of the spin axis of each type due to *the YORP effect alone*. We neglect influence of the gravitational torques due to the Sun and planets as well as meteoroid impacts. (These effects on rotation state are discussed in [Vokrouhlický and Čapek, 2002].) We use the four-order Runge-Kutta integrator with a timestep of 100 years. We compute the evolution of the spin axis for the initial rotation period of 6 hours and various initial obliquities. Each integration was stopped when the YORP effect increased the spin period to the value equal to the orbital period.

**Type I.** Figure 3.4a shows the averaged YORP torques $\langle T_\epsilon \rangle / C$ and $\langle T_\omega \rangle / C$ for one of Gaussian random spheres. This type is characterized by positive values of $\langle T_\epsilon \rangle / C$ in the $(0^\circ, 90^\circ)$ obliquity range and negative values for $\epsilon \in (90^\circ, 180^\circ)$. This means (see Equation (3.6)) that obliquity of such body will be driven to the "asymptotic obliquity" $\epsilon_f = 90^\circ$, i.e., the spin axis will be parallel with the orbital plane. The torque affecting the rotation rate $\langle T_\omega \rangle / C$ is negative for $\epsilon \in (50^\circ, 130^\circ)$, and consequently the rotation of the asteroid is decelerated in this obliquity range and accelerated elsewhere. Type I is (together with Type II) the most probable YORP type and represents approximately 40% of all cases for the zero thermal conductivity.

Figures 3.4b and 3.4c show the evolution of obliquity and rotation rate during 50 Myr. We assumed the initial rotation period to be 6 hours. Initial obliquities were chosen with a step of $10^\circ$. For example, an obliquity with initial value $\epsilon_0 = 80^\circ$ monotonously increases and after $\sim 38.5$ Myr reaches $90^\circ$. The corresponding rotation frequency monotonously decreases and after the same time reaches zero. The rotation of bodies with smaller initial obliquities evolves more slowly. If the initial obliquity is smaller than $\sim 55^\circ$, the rotation rate initially increases until this obliquity is reached. For instance, rotation of a body with $\epsilon_0 = 10^\circ$ is accelerated during the first $\sim 24.3$ Myr.

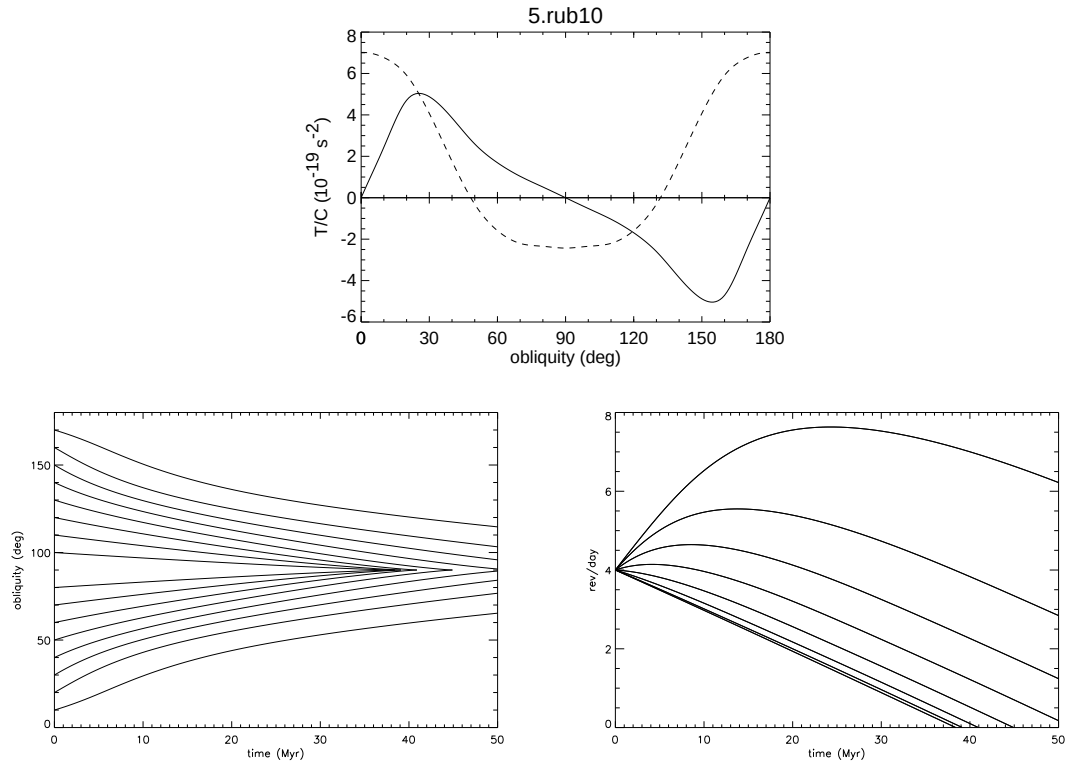


Figure 3.4: The YORP-type I: a) The dependence of $\langle T_\epsilon \rangle / C$ (solid line) and $\langle T_\omega \rangle / C$ (dashed line) on the obliquity, b) the evolution of obliquity, c) evolution of rotation rate. For explanation see the text.

The evolution of obliquities of bodies with $\epsilon_0 > 90^\circ$ is symmetric with respect to the value of $90^\circ$. This means that obliquities monotonously decrease and finally reach $90^\circ$ after the same time as bodies with initial obliquity $180^\circ - \epsilon_0$. Nevertheless, the rotation rates evolve in the same way.

The rate of obliquity change depends also on angular velocity; if a body rotates slowly, obliquity changes faster and vice–versa.

After the obliquity of a body reaches $90^\circ$, its rotation rate falls to zero. Our model is not able to described the YORP effect during this slow rotation limit consistently. One of the basic presumptions - principal axis rotation - is not valid in this state. [Vokrouhlický et al., 2007] studied this limit and realized onset of non-principal axis rotation of slow rotators due to the YORP effect. The non–YORP effects (solar or planetary torques or meteoroid impacts) play an important role during slow rotation state.

**Type II** represents just an opposite case to the Type I (see Figure 3.5b). Here, $\langle T_\epsilon \rangle / C$ is negative in $(0^\circ, 90^\circ)$ and positive in the $(90^\circ, 180^\circ)$ obliquity range. Obliquity of this body will move to $\epsilon_f = 0^\circ$, if the initial obliquity $\epsilon_0$ is less than $90^\circ$, or to $\epsilon_f = 180^\circ$, if the initial obliquity $\epsilon_0$ is larger than $90^\circ$. The spin axis becomes perpendicular to the orbital plane. The spin rate increases due to positive value of $\langle T_\omega \rangle / C$ for $\epsilon \in (55^\circ, 125^\circ)$ and decreases elsewhere. The Type II is (together with Type I) the most probable YORP-behaviour and represents approximately 40% of all cases for zero thermal conductivity.

Evolution of obliquity and rotation frequency can be seen in Figure 3.5b and 3.5c. The initial conditions are the same as in the case of Type I. Focusing on the curve with initial obliquity $80^\circ$ we see that obliquity is decreasing to zero. Rotation rate increases during first $\sim 20\,\mathrm{Myr}$

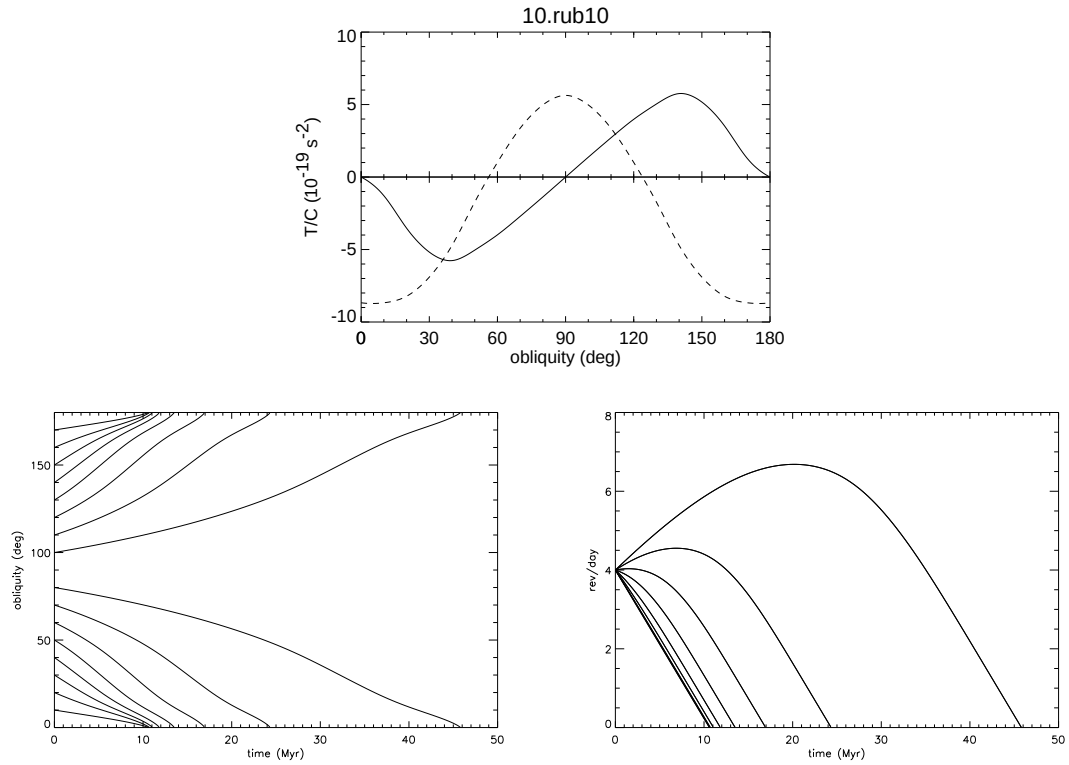


Figure 3.5: The YORP-type II: a) The dependence of $\langle T_\epsilon \rangle / C$ (solid line) and $\langle T_\omega \rangle / C$ (dashed line) on obliquity, b) the evolution of obliquity, c) evolution of rotation rate. For explanation see the text.

(obliquity is $> 55^\circ$ and $\langle T_\omega \rangle > 0$ here) and then decreases to zero. The zero rotation rate as well as zero obliquity is reached after $\sim 46$ Myr.

Spin states of bodies with smaller initial obliquities evolve faster. Some of them do not undergo a phase of acceleration of rotation frequency, because their obliquity has never been larger then $55^\circ$ and therefore $\langle T_\omega \rangle$ is always less than zero.

Bodies with $\epsilon_0 > 90^\circ$ have a similar evolution. In this case the obliquity increases up to $180^\circ$ and it is symmetrical to cases with $\epsilon_0$, while the evolution of the rotation rate is the same.

For the slow rotation limit, see the discussion in the previous paragraph.

**Type III** represents a more complicated case than types I and II discussed above (see Figure 3.6). There are two asymptotic obliquities: the first one in $(0^\circ, 90^\circ)$ obliquity interval and the second one in $(90^\circ, 180^\circ)$. In the particular case of Figure 3.6 these asymptotic obliquities are $\epsilon_f = 44^\circ$ and $\epsilon_f = 136^\circ$. The spin axis will be tilt to the first one, if the initial obliquity is less than $90^\circ$, and tilt to the second one, if initial obliquity is higher then $90^\circ$. The dependence of $\langle T_\omega \rangle / C$ on $\epsilon$ differs from case to case, but in the asymptotic obliquities it is always negative. Type III represents less probable case of YORP behaviour (7%).

We can see from Figure 3.6b, that obliquities of bodies with $\epsilon_0 < 90^\circ$ are driven to the value $44^\circ$, but they reach this obliquity after longer time than 50 Myr. Obliquities $\epsilon$ higher then $90^\circ$ evolve toward value of $136^\circ$. In each case the rotational speed is finally decelerated, but some bodies undergo a phase of spinning up before deceleration (Figure 3.6c).

**Type IV.** There are three asymptotic obliquities for the type IV. The first one is $\epsilon_f = 0^\circ$ and the spin axis tilt to this value if the initial obliquity is less than $42^\circ$. If $\epsilon_0$ is more than $138^\circ$, the

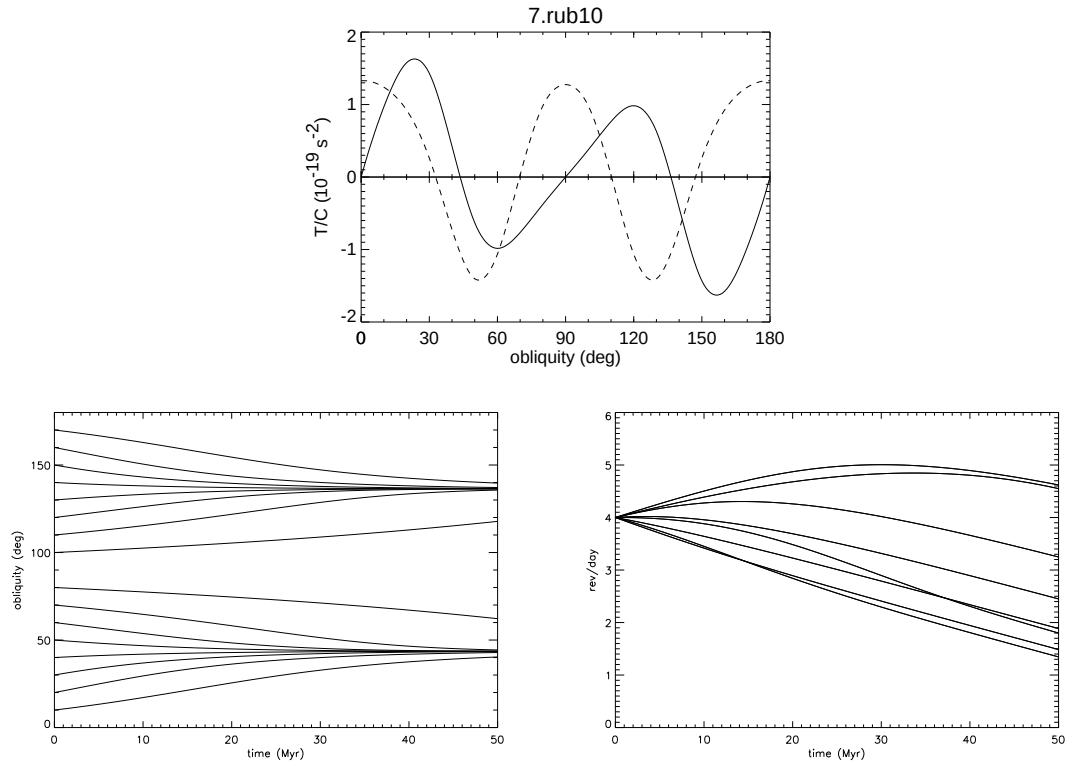


Figure 3.6: The YORP-type III: a) The dependence of $\langle T_\epsilon \rangle / C$ (solid line) and $\langle T_\omega \rangle / C$ (dashed line) on obliquity, b) the evolution of obliquity, c) the evolution of rotation rate. For explanation see the text.

spin axis is driven to $\epsilon_f = 180°$. If initial obliquity lies inside $(32°, 138°)$ range, the asymptotic obliquity will be $\epsilon_f = 90°$. The behaviour of $\langle T_\omega \rangle / C$ differs from case to case again.

The YORP effect drives obliquities of bodies with $\epsilon_0 < 45°$ to final value $0°$, while initial obliquity greater than $135°$ is driven to $\epsilon = 180°$. If $\epsilon_0$ is between $45°$ and $135°$, the obliquity evolves toward $90°$. The evolution of the spin rates is similar as in the previous cases. Initially some bodies undergo a spin up but finally all of them are decelerated.

### Symmetries

General dependence of averaged torques on obliquity can be described by these symmetries[5]:

$$\langle T_\epsilon \rangle(\epsilon) = -\langle T_\epsilon \rangle(180 - \epsilon), \tag{3.15}$$

$$\langle T_\omega \rangle(\epsilon) = \langle T_\omega \rangle(180 - \epsilon). \tag{3.16}$$

Another symmetry stems from change of the spin axis orientation to the opposite one. This is important in the situations when a body is decelerated to zero angular velocity and then spun up in the opposite direction. Then:

$$\epsilon \longrightarrow 180 - \epsilon, \tag{3.17}$$

$$\langle T_\epsilon \rangle(\epsilon) \longrightarrow -\langle T_\epsilon \rangle(\epsilon), \tag{3.18}$$

$$\langle T_\omega \rangle(\epsilon) \longrightarrow -\langle T_\omega \rangle(\epsilon). \tag{3.19}$$

[5] derived from the geometry of the problem

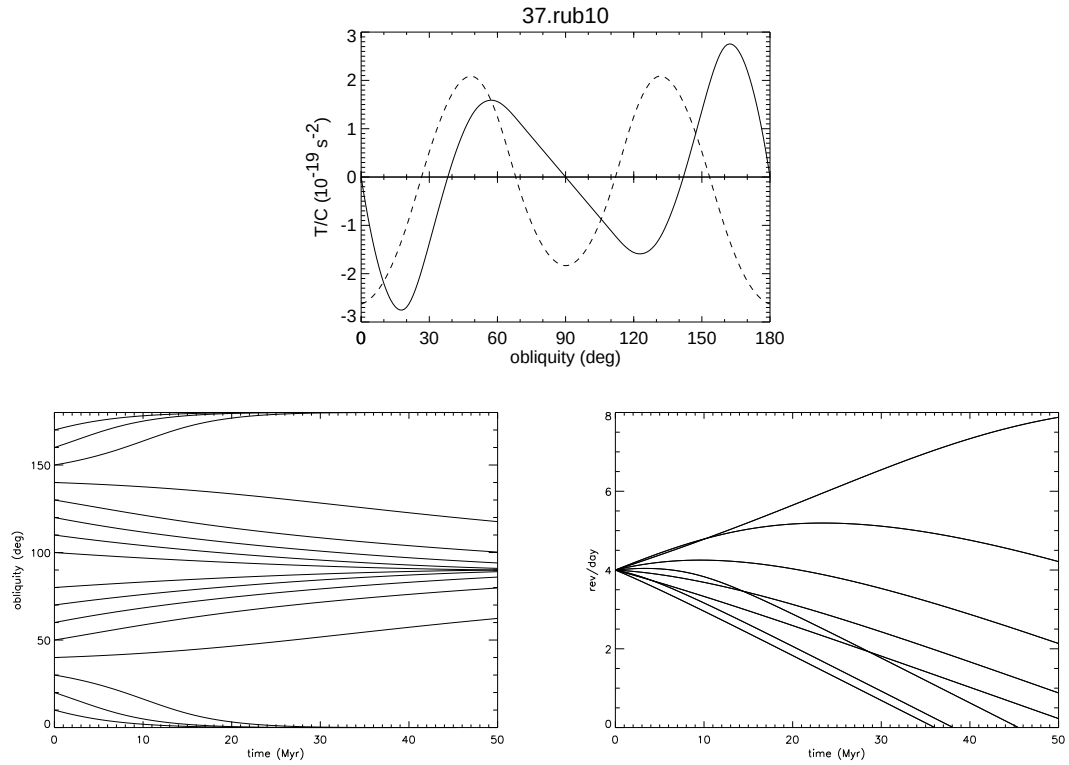


Figure 3.7: The YORP-type IV: a) The dependence of $\langle T_\epsilon \rangle / C$ (solid line) and $\langle T_\omega \rangle / C$ (dashed line) on obliquity. b) the evolution of obliquity, c) the evolution of rotation rate. For explanation see the text.

Note that all these symmetries are valid only for bodies with zero thermal conductivity on circular orbits. An elliptic orbit and non–zero thermal conductivity lead to deviations from symmetries mentioned above.

### 3.3.2 The non–zero conductivity of the surface material

*This section is based on [Čapek and Vokrouhlický, 2004].*

Here we discuss our statistical investigation of the influence of conductivity of the surface material on the orbit-averaged YORP torques $\langle T_\epsilon \rangle$ and $\langle T_\omega \rangle$ for a sample of 200 Gaussian random spheres. We assume three different values of surface conductivity: $K = 0$, 0.001 and 0.01 W/m/K. The thermal conductivity represents a very important quantity – it can vary by several orders of magnitude for different materials. This is discussed especially in Appendix A and Section 3.4.1.

We assumed that orbits are circular with $a = 2.5\,\mathrm{AU}$ and period of rotation are 6 hr. The volume corresponded to a sphere with radius 1 km, the bulk density was $\rho_{bulk} = 2.5\,\mathrm{g/cm^3}$, the surface density was a bit smaller $\rho_{surf} = 1.7\,\mathrm{g/cm^3}$, the thermal capacity was $c = 680\,\mathrm{J/kg/K}$ and albedo $A = 0$.

The computation of surface temperature was performed by a one-level scheme (see Appendix A), with a non-constant spatial step, increasing as a geometrical series with quotient $q \sim 1.0725$, and a time step $\Delta t = 500\,\mathrm{s}$ (it corresponds to $\sim 8^\circ$ of rotation). The temperature computation along the orbit was made so many times, until the temperature difference between the last two turns was less than 0.5 K. The lower boundary condition was put down in the depth $15\ell_s$,

where $\ell_s$ represents the penetration depth of a seasonal temperature wave. For more details see Appendix A.

We focused mainly on the following characteristics of the YORP effect:

1. An abundance of particular YORP-types.
2. A fraction of asymptotically accelerated bodies.
3. A strength of the YORP torque. An appropriate quantity describing the torque component $\langle T_\omega \rangle$ (which affects the angular velocity) is the doubling time $t_d$. The amplitude of $\langle T_\epsilon \rangle$ torque component (in units degrees per Myr) was chosen a description of obliquity change.

**Zero conductivity.** We studied this quite unrealistic limit case at the beginning of our investigation, because it is simple to evaluate – it is not necessary to solve HDE in this case. The thermal force (and torque) can be determined directly from insolation (see (2.10)). This allows to compute YORP effect for relatively large number of bodies.

Figure 3.9 shows orbit averaged rate of change of the obliquity and Figure 3.9 shows orbit averaged rate of change of the rotation speed. Among 200 Gaussian random spheres, there is roughly the same number of type I and type II objects: 40.0% and 46.5%, respectively. This means almost the same number of spin axes are driven to asymptotic obliquities $0°/180°$ and $90°$. Among 500 Gaussian random spheres the difference between occurrences of these two types is even smaller[6] A minority of cases is represented by type III (7%) and IV (6.5%). The rotation of only 2% of all the bodies is accelerated in the asymptotic obliquity; all these cases correspond to bodies of type III or IV. Strength of the YORP torque can be characterized by a median of doubling times which is 14 Myr, and by a median of $\langle d\epsilon/dt \rangle$ amplitude, which is $3\,°$/Myr (see Figure 3.11a,b).

**Conductivity** $0.001\,\mathbf{W/m/K}$**.** We chose this value to describe a thermal behaviour of highly particulated regolith-like surface. This is actually close to the lunar regolith value. The computation of the HDE is necessary here.

The balance between the YORP types I and II disappears completely in this case, as we can seen in Figure 3.8. A lot of types I transform to types II: only 7% of bodies remain in the type I, while 88% form type II. As a consequence the spin axes are driven with a higher likelihood to the asymptotic obliquity $0°/180°$. The spin rate affecting YORP torque is almost the same as in the case of zero obliquity, as shown in Figure 3.8. This means that all types I transformed to types II will be asymptotically accelerated (40% of al the bodies).

Type III is represented by 5% of objects and there is no type IV. The median of doubling times is 13 Myr and the median of $\langle d\epsilon/dt \rangle$ amplitude is $6\,°$/Myr (see Figure 3.11c,d).

**Conductivity** $0.01\,\mathbf{W/m/K}$**.** This thermal conductivity value was chosen to describe surface composed of a mixture of regolith and fresh rock.

The largest difference between abundance of types I (95.5%) and types II (3.5%) can be seen in Figure 3.10. The number of asymptotically accelerated bodies as well as spin axes driven to $0°/180°$ is even higher than in the case of $K = 0.001\,\mathrm{W/m/K}$. Abundance of types III and IV is the same - 0.5%. This corresponds to the most powerful YORP effect among among the studied conductivities: The median of doubling times is 12 Myr and the median of $\langle d\epsilon/dt \rangle$ amplitude is $9\,°$/Myr (see Figure 3.11e,f).

[6] Abundance of type I, II, III and IV are 39.2%, 40.4%, 10.2% and 6.2%. The remaining 4% correspond to cases with a more complicated evolution.

| thermal conductivity | abundance of types | | | | | $d\epsilon/dt$ | $t_d$ | # of accelerated |
|---|---|---|---|---|---|---|---|---|
| (W/m/K) | I | II$^-$ | II$^+$ | III | IV | (deg/Myr) | (Myr) | % |
| 0.000 | 40 | 46.5 | 0 | 7 | 6.5 | 3.33 | 14.3 | 2 |
| 0.001 | 7 | 52.5 | 35.5 | 5 | 0 | 5.94 | 13.1 | 40 |
| 0.010 | 3.5 | 52 | 43.5 | 0.5 | 0.5 | 8.60 | 11.9 | 45 |

Table 3.1: Influence of surface conductivity on the abundance of different YORP-types and the YORP evolution timescale among 200 (or 500 in the case of zero conductivity) gaussian random spheres. The II$-$ (II$^+$) denotes YORP type II with the asymptotic deceleration (acceleration) of rotation.

### 3.3.3 Discussion

The study of the YORP effect on a large sample of artificial shapes, corresponding to small Main Belt asteroids with the assumption of zero thermal conductivity, shows that shapes can be divided according to the obliquity-affecting YORP component $T_\epsilon$ into four principal groups. The Type I is driven to the obliquity 90° and rotation is asymptotically decelerated. Type II is characterized by driving the initial spin axis to obliquity 0° or 180° and asymptotic spinning down again. Less frequent types III and IV have more complicated behaviour, but in most cases they are also asymptotically decelerated.

The statistical study of YORP effect on a sample of Gaussian random spheres shows that the surface thermal conductivity $K$ strongly affects YORP component $T_\epsilon$, which changes the obliquity, while spin rate affecting torque $T_\omega$ is nearly independent on the surface conductivity $K$. Very low value of conductivity (zero limit) results in an equal likelihood of driving the spin axes to the asymptotic obliquity 0°/180° and 90° and the rotation of the most of bodies is asymptotically decelerated. More realistic values of conductivity (0.001 and 0.01 W/m/K) lead to higher likelihood of driving spin axes to the obliquity 0°/180° and almost equal probability of accelerating and decelerating rotation in the asymptotic states. The quantitative results are summarized in Table 3.1.

We also found that the rotation of bodies with obliquity $\epsilon \simeq 55°$ and $\epsilon \simeq 125°$ is neither accelerated nor decelerated.

The YORP evolution timescales are shorter than collisional timescales. The YORP effect is then able to significantly accelerate the rotational speed (maybe up to a bursting limit) or decelerate it (to the state of very slow tumbling rotators).

Our model is not able to describe the YORP effect in these two limit states. In the case of very fast rotators it is because of very large CPU expenses and in the case of very slow rotators (and also in case of bodies with size comparable to penetration depth of seasonal temperature wave – i.e. meteodoids) due to possible non-principal axis rotation of such bodies and more complicated heat diffusion inside of them.

Since the YORP component $T_\omega$ does not depend on the surface thermal conductivity $K$, the approximation of zero $K$ can be used for modeling the short-time evolution of spin states due to the YORP effect. For instance, it can be used for the prediction and subsequent direct detection of the YORP effect. On the other hand, the $T_\epsilon$ depends on the thermal conductivity. The model with the finite value of the surface thermal conductivity should be used for an investigation of the long-time evolution of the spin states due to the YORP effect.

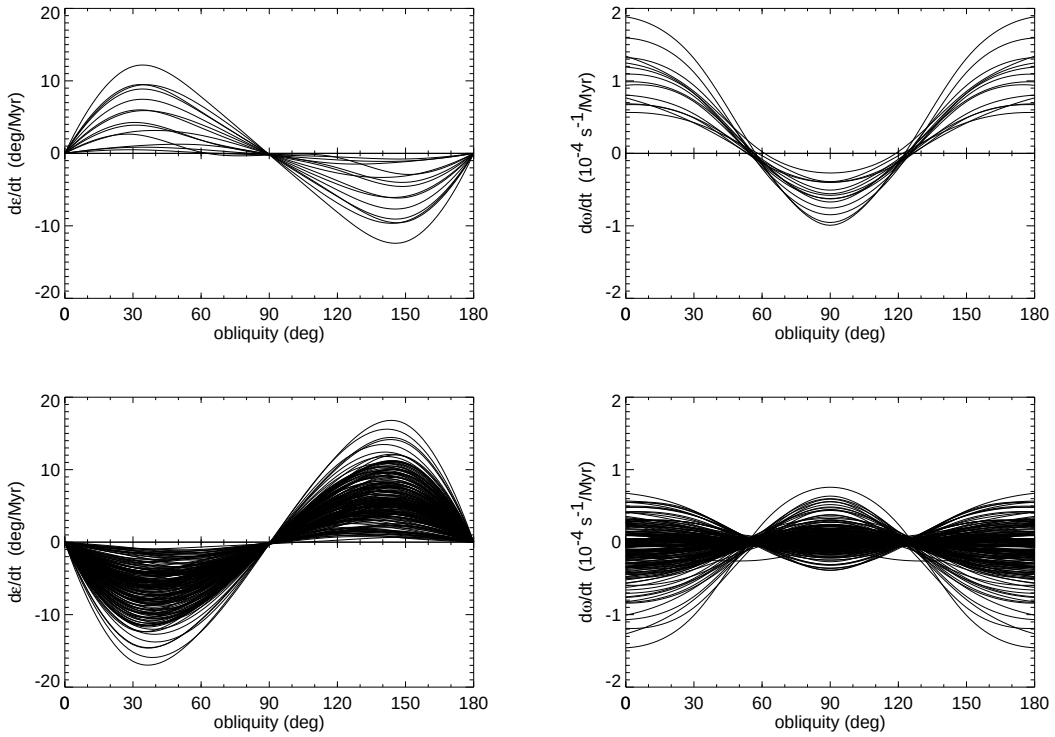


Figure 3.8: The orbit averaged YORP effect as a function of obliquity for 200 Gaussian random spheres for thermal conductivity $K = 0.001\,\mathrm{W/m/K}$. The figures in the left column represent the orbit-averaged rate of change of the obliquity $\langle d\epsilon/dt \rangle$, while the figures in the left column represent the orbit-averaged change rate of angular velocity $\langle d\omega/dt \rangle$. The upper row describes Type I objects, the lower one Type II. Here, the Type II is more likely. Type I produces asymptotic deceleration while Type II produces both deceleration and acceleration of rotation.

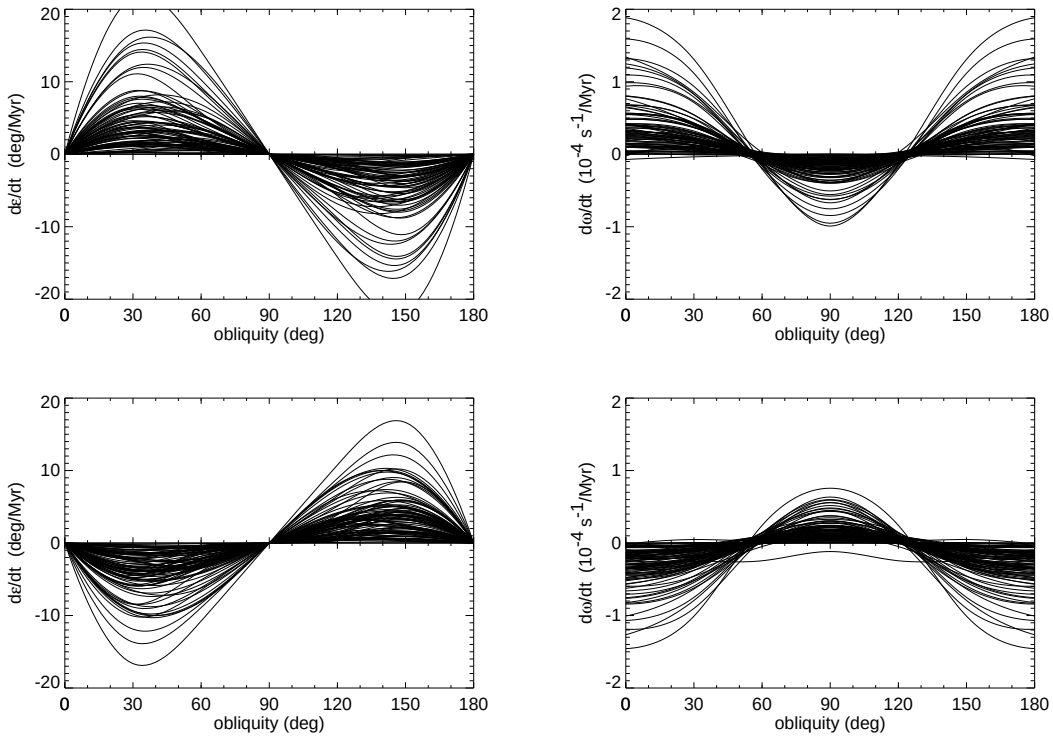


Figure 3.9: The orbit averaged YORP effect as a function of obliquity for 200 Gaussian random spheres in case of a zero conductivity limit. The figures in the left column represent the orbit-averaged rate of change of the obliquity $\langle d\epsilon/dt \rangle$, while the figures in the left column represent the orbit-averaged change rate of angular velocity $\langle d\omega/dt \rangle$. The upper row describes Type I objects, the lower one Type II. Both cases are equally likely and both produce an asymptotic deceleration of rotation.

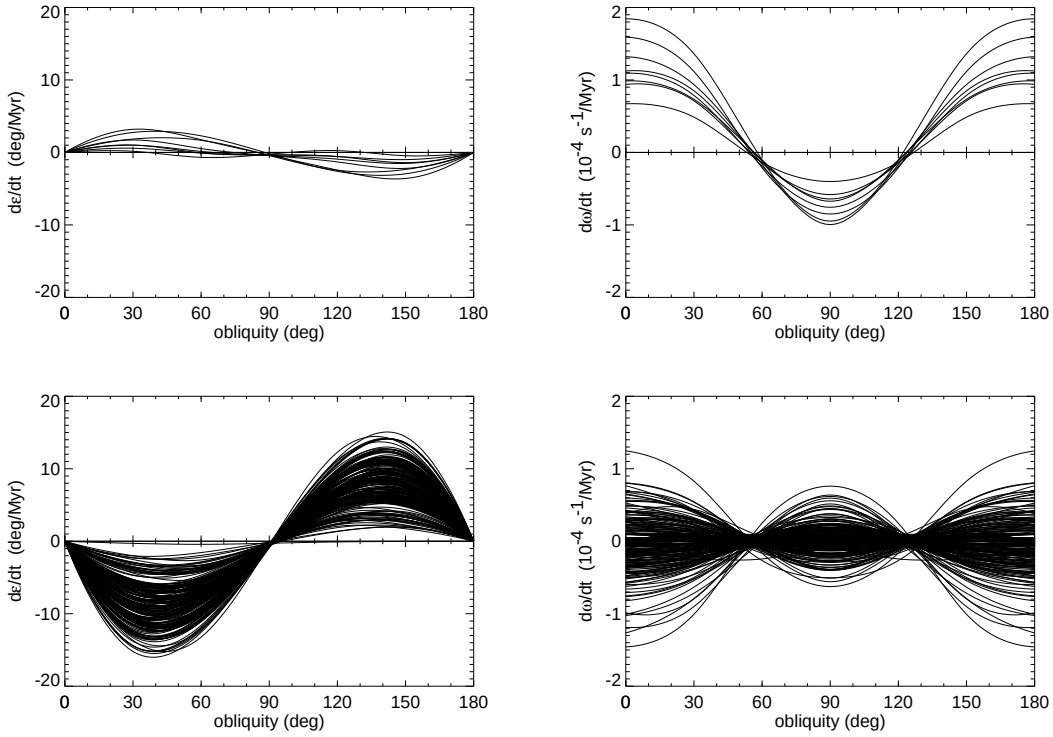


Figure 3.10: The orbit averaged YORP effect as a function of obliquity for 200 Gaussian random spheres for thermal conductivity $K = 0.01\,\mathrm{W/m/K}$. The figures in the left column represent the orbit-averaged rate of change of the obliquity $\langle d\epsilon/dt \rangle$, while the figures in the left column represent the orbit-averaged change rate of angular velocity $\langle d\omega/dt \rangle$. The upper row describes Type I objects, the lower one Type II. A great difference between the number of Type I and Type II bodies can be seen clearly. Type I produces asymptotic deceleration while Type II produces both deceleration and acceleration of rotation.

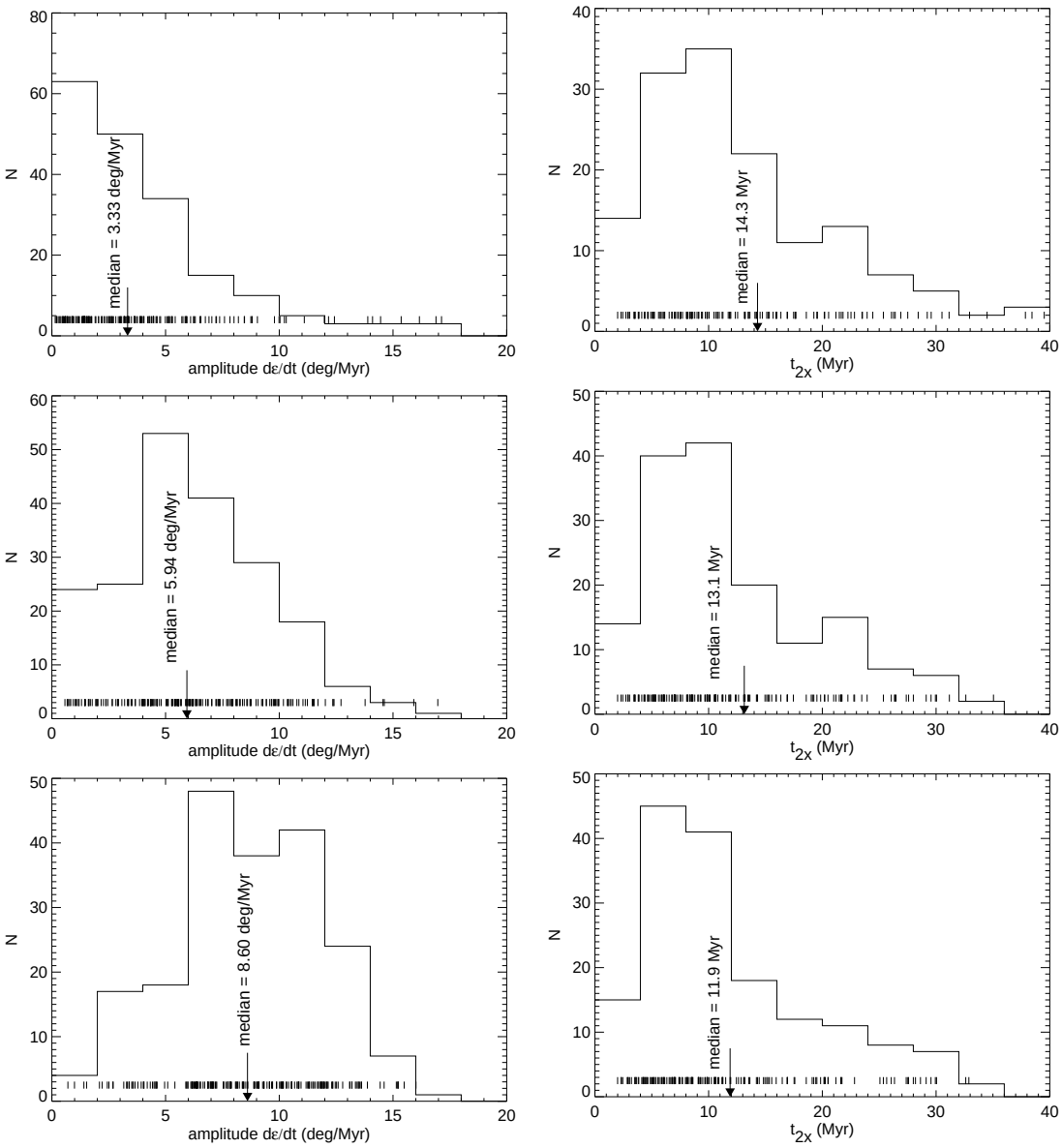


Figure 3.11: Histograms of statistical distributions of the characteristic timescales of the YORP effect acting on sample of 200 Gaussian random spheres for conductivity $K = 0\,\mathrm{W/m/K}$ (upper row, a and b), $K = 0.001\,\mathrm{W/m/K}$ (middle one, c and d) and $K = 0.01\,\mathrm{W/m/K}$ (lower row, e and f). The left column shows the distribution of maximal obliquity change rate. Small lines at the bottom of plots represent actual values and the arrow is the median value. Tn the right column we present distribution of doubling time at the asymptotic values of obliquity.

## 3.4 The YORP effect on individual bodies

*This section is based on [Vokrouhlický and Čapek, 2002] and [Vokrouhlický et al., 2004].*

We chose several asteroids with available shape models and investigated how the YORP effect acts on these bodies. We study both the YORP dependence on the thermal conductivity for bodies on circular orbits [Čapek and Vokrouhlický, 2004] and how it affects angular velocity of asteroids in actual configuration including possible direct detection of the YORP effect [Vokrouhlický et al., 2004].

### 3.4.1 The YORP dependence on the surface thermal conductivity

The material properties, like the density $\rho$ and thermal capacity $c$ of small Solar System bodies can be roughly determined by laboratory measurement of its meteorite equivalents (e.g. [Yomogida and Matsui, 1983]). In the case of the surface thermal conductivity $K$ the situation is more complicated. We do not know the composition and degree of porosity of surface material and then have to assume some similar material measured in laboratory, or use measurements of the lunar soil returned by Apollo missions (e.g. [Cremers, 1972])

Another way to determine $K$ is to use data from infrared observations [Delbò et al., 2006], [Delbò et al., 2007] or measurements of non-gravitational (Yarkovsky) semimajor axis drift which is strongly dependent on asteroid's surface thermal inertia [Chesley et al., 2003]. The value of the thermal conductivity can vary by several orders of magnitude. For highly particulated regolith it can be $K \simeq 10^{-4}\,\mathrm{W/m/K}$, while for fresh iron surface $K \simeq 80\,\mathrm{W/m/K}$. Moreover, [Delbò et al., 2007] discovered a dependence of thermal inertia on asteroids diameter. So, the value of thermal conductivity of surface is the most uncertain quantity of all.

Here we present a study of the YORP effect dependence on the thermal conductivity $K$. We used several bodies with precisely determined shapes and assumed they are on a circular orbit about the Sun with semimajor axis $a = 2.5\,\mathrm{AU}$. Other important quantities are listed in Table 3.2. The surface thermal conductivity varies from $10^{-9}\,\mathrm{W/m/K}$ to $10\,\mathrm{W/m/K}$.

| | |
|---|---|
| semimajor axis | 2.5 AU |
| period of rotation | 6 hours |
| bulk density | $2.5\,\mathrm{g/cm^3}$ |
| surface density | $1.7\,\mathrm{g/cm^3}$ |
| thermal capacity | $680\,\mathrm{J/kg/K}$ |
| albedo | 0.1 |
| emissivity | 0.9 |

Table 3.2: Orbital and physical parameters used for the study of the YORP $K$-dependence. The orbit is assumed circular and the thermal conductivity in the range $\langle 10^{-9}, 10^{1} \rangle\,\mathrm{W/m/K}$.

The computation was performed by a one-level scheme with a non-constant spatial step which is increasing as a geometrical series with a quotient $q = 1.0725$, and a time step $\Delta t = 500\,\mathrm{s}$ (it corresponds to $\sim 8^\circ$ of rotation phase). The computation of surface temperature along the orbit was made several times, until the temperature difference between the last two turns was less than 0.5 K. The lower boundary condition was applied in the depth $15\ell_s$, where $\ell_s$ is the penetration depth of seasonal temperature variations. For more details see Appendix A.

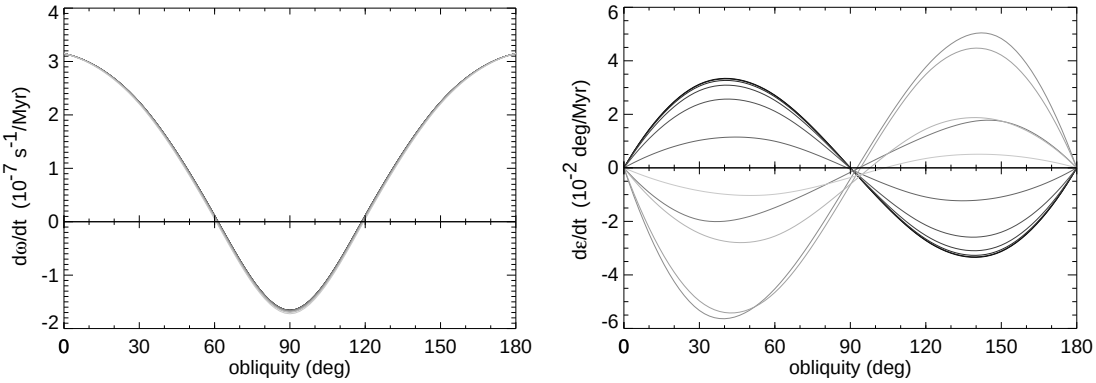


Figure 3.12: The orbit averaged rate of change of the angular velocity $\omega$ (left) and obliquity $\epsilon$ (right) due to the YORP effect for asteroid (433) Eros. Grey levels denote different surface thermal conductivities from $10^{-9}$ W/m/K (darkest, corresponding to the Rubincam's limit) to 10 W/m/K (lightest, corresponding to highly conductive material). For more discussion see the text.

### (433) Eros

The dependence of the YORP torque on the thermal conductivity for an Eros-shaped body is shown in Figure 3.12. There is a orbit-averaged rate of change $\langle d\omega/dt \rangle$ of angular velocity and a rate of change of the obliquity $\langle d\epsilon/dt \rangle$ due to the YORP effect.

It can be seen that the component of the YORP affecting the speed of rotation $\omega$ almost does not depend on the thermal conductivity in the studied interval of $K$. On the other hand, the YORP-induced obliquity change depends on the thermal conductivity $K$ very strongly. Low values of $K$ lead to the type I of the YORP classification. This means the spin axis would evolve toward the obliquity 90° and the rotation would decelerate. As $K$ increases, the amplitude of $\langle d\epsilon/dt \rangle$ decreases. For the conductivity $K \simeq 5 \times 10^{-4}$ W/m/K, the YORP changes to the Type II. In this case the spin axis is driven to 0° or 180° obliquity, but the rotation of the body will be accelerated in these states because $\langle d\omega/dt \rangle$ remains unaffected by the thermal conductivity. For higher $K$'s the amplitude of $\langle d\epsilon/dt \rangle$ increases with thermal conductivity and reaches the maximal value when $K \simeq 10^{-2}$ W/m/K. Subsequently, the amplitude decreases. Note that for high conductivities the symmetry of $\langle d\epsilon/dt \rangle$ with respect to $\epsilon = 90°$ is broken.

### (6489) Golevka

We can see $\langle d\omega/dt \rangle$ and $\langle d\epsilon/dt \rangle$ for Golevka in Figure 3.13. Like Eros, the component of the YORP effect changing the speed of rotation is nearly independent on the thermal conductivity in the studied interval, unlike the YORP component affecting the obliquity. Low values of $K$ lead to the type IV of the YORP classification. As $K$ increases, the amplitude of $d\epsilon/dt$ decreases and also the node moves slightly from $\epsilon \sim 60°$ towards zero obliquity[7]. For the conductivity $K \simeq 5 \times 10^{-4}$ W/m/K, the YORP changes to the type I. In this case, the spin axis is driven to obliquity 90° but the rotation of the body will be accelerated in this state, because $\langle d\omega/dt \rangle$ remains almost unaffected by thermal conductivity $K$. As $K$ further increases, the amplitude of $\langle d\epsilon/dt \rangle$ increases, reaches the maximum value for $K \simeq 10^{-2}$ W/m/K and then falls-off a little. The symmetry of $\langle d\epsilon/dt \rangle$ with respect to obliquity $\epsilon = 90°$ is broken again for higher conductivities.

[7] The node at 120° moves towards $\epsilon = 180°$.

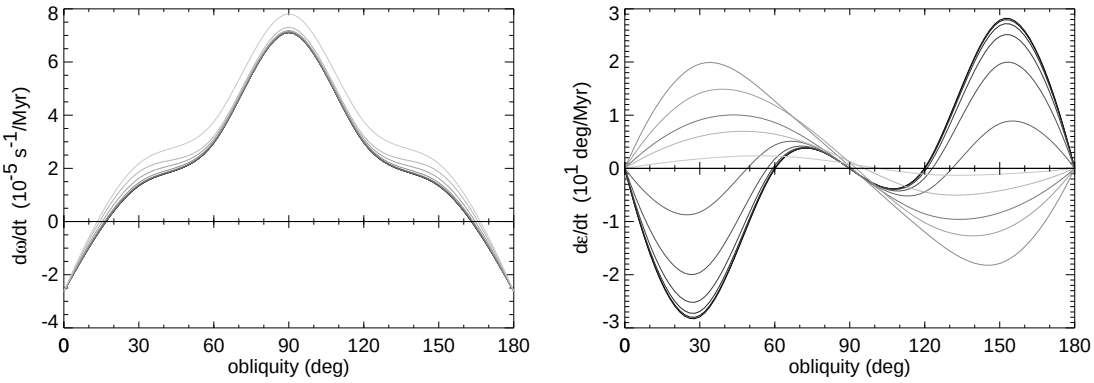


Figure 3.13: The orbit averaged rate of change of the angular velocity $\omega$ (left) and obliquity $\epsilon$ (right) due to the YORP effect for asteroid (6489) Golevka. Grey levels denote different surface thermal conductivities from $10^{-9}$ W/m/K (darkest, corresponding to the Rubincam's limit) to 10 W/m/K (lightest, corresponding to highly conductive material). For more discussion see the text.

### (243) Ida

Figure 3.14 shows the orbit-averaged rate of change $\langle d\omega/dt \rangle$ of angular velocity and rate of change $\langle d\epsilon/dt \rangle$ of the obliquity for asteroid (243) Ida. As in previous cases, $\langle d\omega/dt \rangle$ does not depend on $K$, while $\langle d\epsilon/dt \rangle$ does. The YORP type is II and increasing thermal conductivity only changes its amplitude. Up to $K \simeq 10^{-2}$ W/m/K the amplitude increases and for higher conductivities decreases.

### (25143) Itokawa

The dependence of the YORP effect on the surface thermal conductivity for asteroid Itokawa can be seen in Figure 3.15. This is the same case as Eros. The YORP component $\langle d\omega/dt \rangle$ is nearly independent on $K$, while $\langle d\epsilon/dt \rangle$ belongs to the Type I for low conductivities and to the Type II for high ones. The transition occurs for $K \simeq 5 \times 10^{-5}$ W/m/K.

### 1998 KY26

Figure 3.16 shows the orbit-averaged rate of change of angular velocity $\langle d\omega/dt \rangle$ and the rate of change of obliquity $\langle d\epsilon/dt \rangle$ due to the YORP effect. Again, we can see nearly $K$-independent YORP component affecting the speed of rotation and the YORP component changing the obliquity strongly dependent on $K$. In this case increasing thermal conductivity does not change the YORP type (which is I) but only decreases the amplitude of $\langle d\epsilon/dt \rangle$.

### Discussion

The study of the $K$-dependence of the YORP effect for several real shapes shows a strong dependence of $\langle T_\epsilon \rangle$ or $\langle d\epsilon/dt \rangle$ on thermal conductivity in the range $10^{-9}$ to $10^{1}$ W/m/K, like in the case of the artificial shapes. In most cases the YORP for realistic values of $K$ belongs to the Type II. The YORP component $\langle T_\omega \rangle$ or $\langle d\omega/dt \rangle$ is nearly independent on $K$.

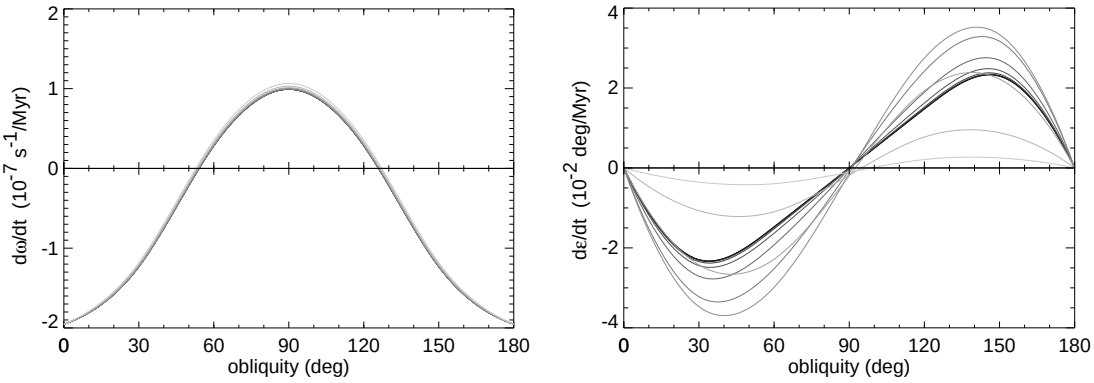


Figure 3.14: The orbit averaged rate of change of the angular velocity $\omega$ (left) and obliquity $\epsilon$ (right) due to the YORP effect for asteroid (243) Ida. Grey levels denote different surface thermal conductivities from $10^{-9}$ W/m/K (darkest, corresponding to the Rubincam's limit) to 10 W/m/K (lightest, corresponding to highly conductive material). For more discussion see the text.

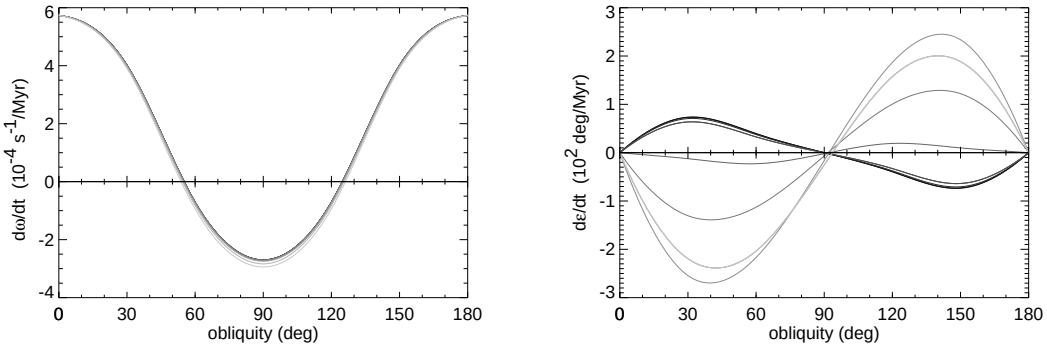


Figure 3.15: The orbit averaged rate of change of the angular velocity $\omega$ (left) and obliquity $\epsilon$ (right) due to the YORP effect for asteroid (25143) Itokawa. Grey levels denote different surface thermal conductivities from $10^{-9}$ W/m/K (darkest, corresponding to the Rubincam's limit) to 10 W/m/K (lightest, corresponding to highly conductive material). For more discussion see the text.

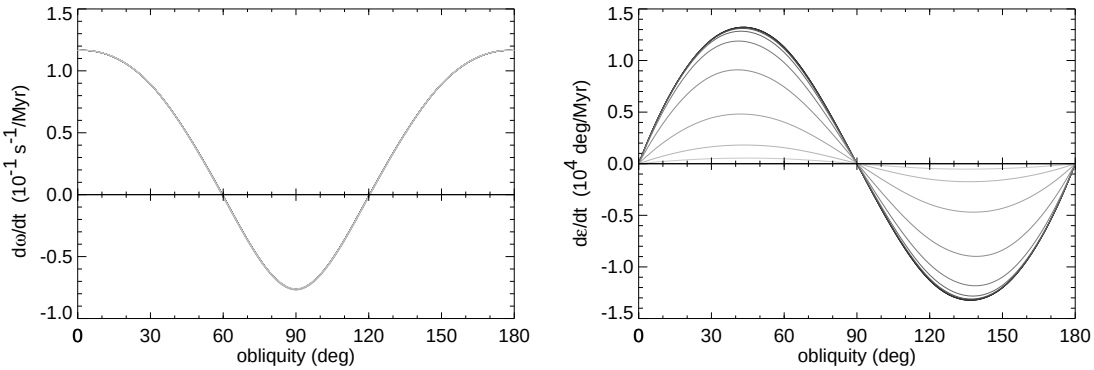


Figure 3.16: The orbit averaged rate of change of the angular velocity $\omega$ (left) and obliquity $\epsilon$ (right) due to the YORP effect for asteroid 1998 KY26. Grey levels denote different surface thermal conductivities from $10^{-9}$ W/m/K (darkest, corresponding to the Rubincam's limit) to 10 W/m/K (lightest, corresponding to highly conductive material). For more discussion see the text.

### 3.4.2 The YORP effect for real objects and their orbits

We computed the YORP effect for several asteroids with known orbits, shapes and spin parameters. The list of bodies and their orbital and physical parameters can be found in Table 3.3:

| | Eros | Geographos | Golevka | Ida | Itokawa | 1998KY26 |
|---|---|---|---|---|---|---|
| semimajor axis (AU) | 1.45823 | 1.24547 | 2.5065 | 2.816276 | 1.32274 | 1.23215 |
| excentricity | 0.222891 | 0.335416 | 0.604317 | 0.04616 | 0.279475 | 0.201462 |
| inclination (°) | 10.83 | 13.342 | 2.277 | 1.138 | 1.728 | 1.481 |
| arg. perihel. (°) | 178.645 | 275.8 | 66.06 | 108.55 | 161.021 | 209.181 |
| ascend. node (°) | 304.404 | 337.3 | 211.502 | 324.21 | 70.917 | 84.451 |
| pole of rotation $\lambda$, $\beta$ (°) | 17.2, 11.3 | 55, -46 | 202, -45 | 262, -68 | 355, -84 | |
| obliquity (°) | 89.1 | 150 | 134.6 | 157 | 172.3 | |
| period of rotation (h) | 5.27 | 5.23 | 6.03 | 4.63 | 12.13 | 0.17837 |
| precision of period determ. $\sigma$ | $1\times10^{-7}$ | $1.4\times10^{-7}$ | $1.7\times10^{-5}$ | $1.5\times10^{-6}$ | $5\times10^{-4}$ | $7\times10^{-6}$ |
| thermal conductivity (W/m/K) | 0.01 | 0.02 | 0.01 | 0.01 | 0.01 | 0.001 |
| thermal capacity (J/kg/K) | 680 | 680 | 680 | 680 | 800 | 680 |
| bulk density (g/cm$^3$) | 2.5 | 2.5 | 2.7 | 2.7 | 2.5 | 2.5 |
| surface density (g/cm$^3$) | 1.7 | 1.7 | 1.7 | 1.7 | 2.0 | 1.7 |
| albedo | 0.1 | 0.2 | 0.1 | 0.2 | 0.1 | 0.1 |
| emisivity | 0.9 | 0.8 | 0.9 | 0.8 | 0.9 | 0.9 |
| $\Delta t$ - first level (s) | 222 | 87 | 500 | | 192 | |
| $\Delta t$ - second level (s) | 4 | | 5 | | 10 | |

Table 3.3: Orbital and physical parameters of asteroids used for our study of the YORP. Orbital data was taken mainly from NeoDyS site `http://newton.dm.unipi.it` and AstDys `http://hamilton.dm.unipi.it`. Information about the spin state was taken from [Miller et al., 2002] for Eros, [Hudson and Ostro, 1999] for Geographos, [Hudson et al., 2000] for Golevka, [Davies et al., 1996] for Ida, [Kaasalainen et al., 2003] for Itokawa and [Ostro et al., 1999] for 1998KY26.

The surface temperature along the orbit was computed by a two-level scheme. The timestep was a few hundred seconds in the first level and several seconds in the second level (see Table 3.3). The initial spatial step was chosen in order to fulfill the von Neumann stability criterion. The precision of the surface temperature is typically better than 0.1 K. We computed components of the YORP torque in equally spaced right anomalies.

A possible direct detection of the YORP effect was also studied. For this purpose the most important quantity is the change of angular velocity $\omega$ and, especially, the phase of rotation $\phi$. These quantities are observable (while the change of the obliquity is too small). Moreover, $\langle T_\omega \rangle$ is nearly independent on the surface thermal conductivity, which is not known accurately. The angular velocity and the phase of rotation changes due to the YORP effect can be expressed as:

$$\omega_Y(t) = \omega_0 + \int_{t_0}^{t} \frac{T_\omega}{C} dt, \qquad \phi_Y(t) = \phi_0 + \int_{t_0}^{t} \omega_Y(t)\, dt.$$

where $\omega_0$ is the initial angular velocity at the time $t_0$ and the initial phase of rotation is assumed $\phi_0 = 0$. We can also express a fractional change of rotation period as $(dP/dt)/P = -(T_\omega/C)/\omega$. Using the orbit-averaged value of $T_\omega/C$, the angular velocity will change linearly with time, whereas the phase of rotation will change as a square of time (here we neglect an eccentricity of

an orbit):

$$\omega_Y(t) = \omega_0 + \left\langle \frac{T_\omega}{C} \right\rangle t, \qquad \left\langle \frac{P - P_0}{P_0} \right\rangle_Y = -\frac{1}{\omega_0} \left\langle \frac{T_\omega}{C} \right\rangle t, \qquad \phi_Y(t) = \omega_0 t + \frac{1}{2} \left\langle \frac{T_\omega}{C} \right\rangle t^2. \tag{3.20}$$

The phase $\phi$ is the most easily observable quantity that can be used for a detection of the YORP effect. At least three measurements of $\phi$ with appropriate time delay are necessary for a discovery of the quadratic time dependence of $\phi$, indicating the YORP effect. If we take into account that the period of rotation $P_0$ can be initially determined with an error $\delta P$, then this uncertainity propagates and causes apparent changes of $\omega$ and $\phi$:

$$\omega_{\delta P}(t) = \omega_0 \pm \omega_0 \frac{\sigma}{\sigma + 1}, \qquad \left\langle \frac{P - P_0}{P_0} \right\rangle_{\delta P} = \pm\sigma, \qquad \phi_{\delta P}(t) = \omega_0\, t \pm \omega_0 \frac{\sigma}{\sigma + 1}\, t, \tag{3.21}$$

where $\sigma = \delta P / P_0$ is a relative period error. The detection of the YORP effect via a phase shift is possible if it exceeds the effect of uncertainity. This happens after sufficient time interval:

$$t^\phi_{Y>\delta P} = \frac{\sigma}{\sigma + 1} \frac{2\omega_0}{\langle T_\omega / C \rangle}. \tag{3.22}$$

Moreover, the phase shift produced by an uncertainity of the rotation period must be less than $180°$. In other words, $|\phi_{\delta P} - \omega_0 t| < \pi$. It corresponds to the time

$$t^\phi_\pi = \frac{P_0}{2} \frac{\sigma + 1}{\sigma}. \tag{3.23}$$

In the case of a detection by a change of the rotation period, the required time interval is

$$t^P_{Y>\delta P} = \frac{\omega_0 \sigma}{\langle T_\omega / C \rangle}, \tag{3.24}$$

which is shorter than (3.22) by a factor $(\sigma+1)/2$ and moreover there is no restriction like (3.23).

### (433) Eros

Figure 3.17 shows the behaviour of the $T_\omega/C$ during one orbital period of Eros. The origin of time is chosen at an instant of perihelion passage. The mean value $\langle T_\omega/C \rangle = -1.48 \times 10^{-20}\,\mathrm{s}^{-2}$ corresponds to a doubling time 709 Myr. Eros's rotation is decelerated.

With this YORP torque and NEAR/Shoemaker data, rotation period $P = 5.27025547\,\mathrm{hr}$, $\sigma = 1 \times 10^{-7}$ ([Miller et al., 2002]), we have determined the change of rotational period and the phase from 1900 to 2020 as can be seen in Figure 3.18. The origin was chosen on Jan 1, 2001. The phase of rotation changed due to YORP effect by $\sim 4°$ during 100 years, while the uncertainity in rotation period makes phase shift $\sim 7°$ after the same time. In terms of the period, the YORP leads to a relative change of period $(P - P_0)/P_0 \simeq -1.5 \times 10^{-7}$ in 1900, which is slightly higher than uncertainity $\sigma$.

[Ďurech, 2005] compared photometric data of Eros from years 1901 – 1931 with a synthetic lightcurve derived from shape and rotation state obtained by NEAR/Shoemaker space probe. He found that $\langle d\omega/dt \rangle$ cannot be higher than $\sim 5 \times 10^{-20}\,\mathrm{s}^{-2}$. It is interesting, that the formal fit gives the value $\langle d\omega/dt \rangle = -1.4 \times 10^{-20}\,\mathrm{s}^{-2}$, which corresponds well to the value predicted by us, but the case is not statistically conclusive.

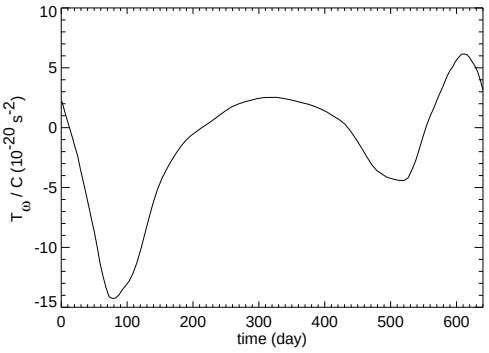


Figure 3.17: The YORP component affecting the angular velocity of (433) Eros during one revolution about the Sun. This was computed using data from Table 3.3.

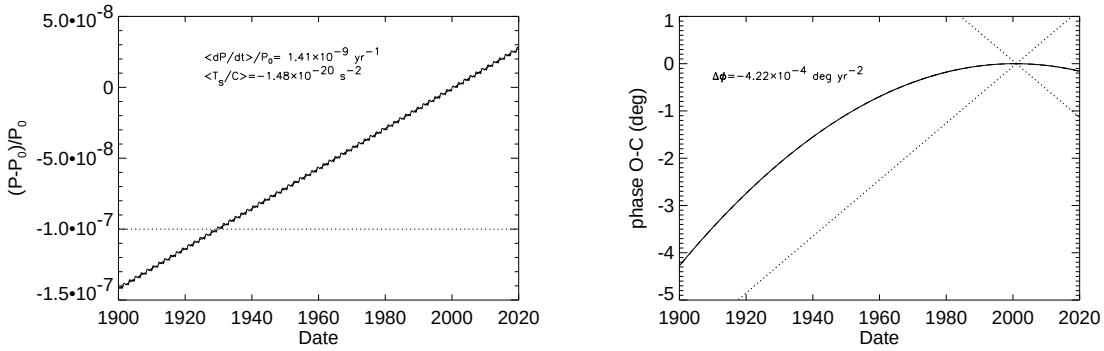


Figure 3.18: Left: The relative change of rotation period of Eros. Right: The corresponding change of the rotation phase. The results are referred to the value $P_0$ =5.27 hr on Jan 1, 2001. The dotted line corresponds to a change of period or phase of rotation due to an uncertain determination of the initial period $P_0$. The relative uncertainity is $\sigma = 1 \times 10^{-7}$. The solid one corresponds to the orbit-averaged YORP effect. Note a linear growth of $(P - P_0)/P_0$ and the corresponding quadratic dependence of phase $O - C$.

### (6489) Golevka

The time dependence of the YORP component $T_\omega/C$ that affects angular velocity of Golevka can be seen in Figure 3.19. The orbit-averaged value is $\langle T_\omega/C \rangle = 2.04 \times 10^{-18}$ s. This corresponds to a doubling time of only 4.5 Myr, the asteroid's rotation is accelerated in this state.

A possibility of a successful direct detection of the YORP can be seen in Figure 3.20: The mean value of the fractional change of rotation period is $\langle (dP/dt)/P \rangle = -2.2 \times 10^{-7}\,\mathrm{yr}^{-1}$. We used data obtained during the close encounter with the Earth in 1995 from [Hudson et al., 2000]: $P = 6.0289$, $\sigma = 1.7 \times 10^{-5}$, and chose an origin of integration on Jan 2, 1995. It can be seen, that the YORP (though relatively strong) does not exceed the effect of uncertainity of rotation period. Unfortunately, no usable photometric data was recorded during the close approach in 2003. Next opportunities will be in 2007, 2011, 2015 and 2019. Due to the large YORP effect on Golevka, the data from these future encounters may lead to a successful detection of the YORP.

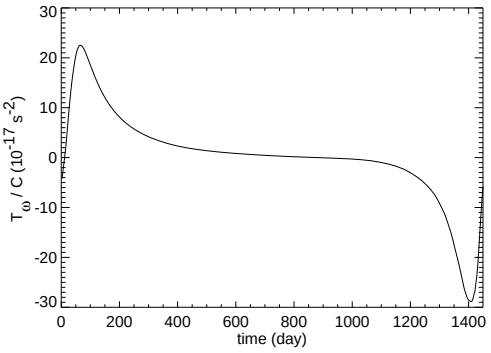


Figure 3.19: The YORP component $T_\omega/C$ affecting the angular velocity for (6489) Golevka during one revolution about the Sun. This was computed using data from Table 3.3.

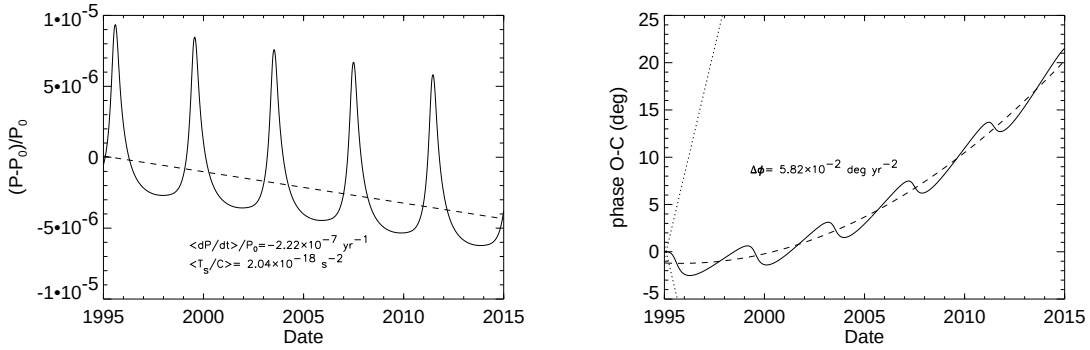


Figure 3.20: The same plots as in Figure 3.18 but for Golevka. The results are referred to the value $P_0$ =6.02667 hr on Jan 2, 1995.

### 1998 KY26

The asteroid 1998 KY26 has an unknown orientation of the spin axis. We can only scale the results obtained in the previous section. We assumed values listed in Table 3.3 and zero obliquity. Then the orbit-averaged YORP component changing the angular velocity is $\langle T_\omega/C\rangle = 1.52 \times 10^{-14}$ and the doubling time $t_d = 20\,400$ yr. This corresponds to a mean fractional change of rotation period $\langle (dP/dt)/P\rangle = 5\times10^{-5}\,\mathrm{yr}^{-1}$. Thus, we expect the possible successful detection of the YORP effect for this body during its next apparition is September 2013. (The determination of the pole orientation is also probable during this apparition.) Even more probable YORP effect detection will be during the close–Earth encounter in June 2024.

### (243) Ida

We do not compute YORP effect for the actual orbital configuration as listed in Table 3.3, but scaling the results from previous section, the orbit averaged component of YORP is $\langle T_\epsilon/C\rangle \simeq 3.5\times10^{-21}\,\mathrm{s}^{-2}$ and the doubling time $t_d \simeq 3.4$ Gyr. This is comparable to the age of the Koronis asteroid family and might have caused the evolution of spins discussed by [Vokrouhlický et al., 2003]. Nevertheless, for direct short-term detection, the YORP is too week.

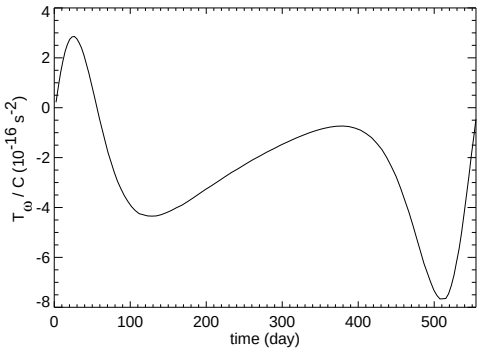


Figure 3.21: The YORP component affecting the angular velocity of (25143) Itokawa during one revolution about the Sun. This was computed using data from Table 3.3.

### (25143) Itokawa

[Vokrouhlický et al., 2004] computed the YORP effect strength for this asteroid and predicted the possible detection of the YORP effect by an observation of the ligtcurve maximum shift during its close encounter in 2004. Unfortunately, this conclusion was wrong: (i) we underestimated the uncertainity of the rotation period by a factor $2\pi$ and (ii) we used an incorrect component of the YORP torque ($T_\epsilon$ or $T_\psi$ instead of $T_\omega$) . This led to conclusion that the rotation of Itokawa is accelerated and a fractional change of Itokawa's rotation is $(dP/dt)/P =\simeq 1.5 - 3 \times 10^{-4}\,\mathrm{yr}^{-1}$. An attempt to detect it failed.

Using the correct data (see Table 3.3 and Appendix) we found that Itokawa's rotation is accelerated due to the YORP torque $\langle T_\epsilon/C\rangle = 6.6 \times 10^{-17}\,\mathrm{s}^{-2}$ and the value of the fractional change of spin period is $(dP/dt)/P = -1.45 \times 10^{-5}\,\mathrm{yr}^{-1}$. This corresponds to the doubling time $t_d \simeq 69\,000$ years. The phase shift due to the YORP effect then increases as $\Delta\phi = 1.89^\circ \left(\frac{t}{\mathrm{yr}}\right)^2$ and after three years it is $\sim 17^\circ$. Note that we obtained these results using convex-hull shape model of [Kaasalainen et al., 2003] based on radar and optical Earth-based observations.

Recently, [Scheeres et al., 2007] have used more reliable data of shape and rotation of Itokawa from Hayabusa mission to Itokawa and with aid of semianalytical theory of YORP effect they found Itokawa's spin rate deceleration $2.5 - 4.5 \times 10^{-17}\,\mathrm{s}^{-2}$, depending on the shape model used. They also discussed strong dependence of strength and sense of YORP on the shape model. Itokawa seems to be an exemplary case in this sense.

### (1620) Geographos

Using data from Table 3.3 we computed the YORP effect on the asteroid (1620) Geographos. In this case we faced a problem with the choice of the right shape model. Using the shape model derived from combination of the radar and optical observations (available at the website `http://www.psi.edu/pds/asteroid/`), we obtained the YORP torque (produced by thermal and reflected radiation) changing the spin rate $d\omega/dt = T_\omega/C = -4.4 \times 10^{-18}\,\mathrm{s}^{-2}$. In this model, the $z-$axis does not correspond to the axis of the maximal moment of inertia.

Then we made rotation of the body-fixed frame ($90^\circ$ about the $x-$axis) to the system of proper axes and achieved an agreement of $z-$axis orientation with the axis of maximal moment of inertia and also with the position of "north pole" in [Hudson and Ostro, 1999] (see Figure D.1). In this case, the change of spin rate is $d\omega/dt = 3 \times 10^{-19}\,\mathrm{s}^{-2}$.

Another shape model derived by Ďurech (personal communication) from ligtcurve analysis (see Figure D.2) gives a value $d\omega/dt = 2.4 \times 10^{-18}\,\mathrm{s}^{-2}$. Here we used the pole of the spin axis

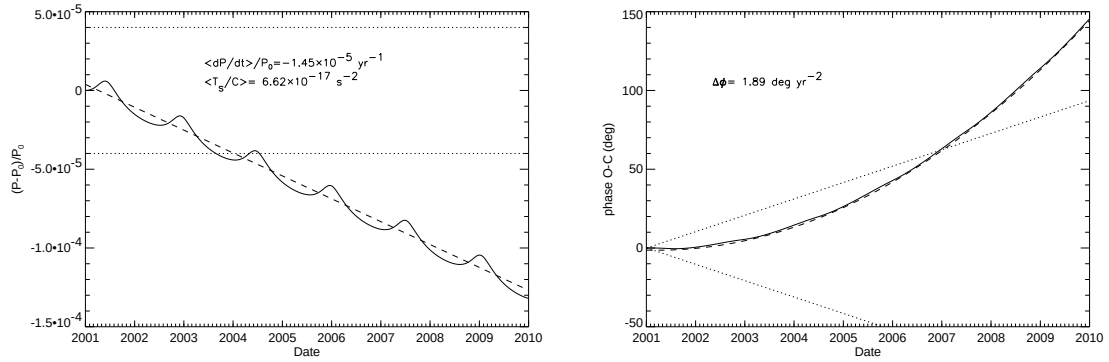


Figure 3.22: The same as 3.18 but for Itokawa. The results are referred to the value 12.134 hr on Jan 1. 2001.

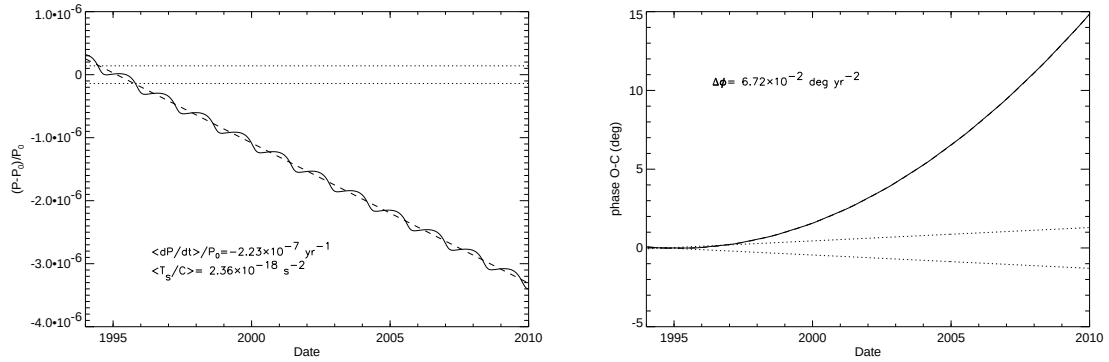


Figure 3.23: Left: Relative change of rotation period of (1620) Geographos. Right: Change of the rotation phase. The results are referred to the value $P_0$ =5.23 hr on September 15, 1994. The dotted line corresponds to the change of period or phase of rotation due to uncertain determination of the initial period $P_0$. The uncertainity of the spin period is $\sigma = 1.4 \times 10^{-7}$ (according to [Hudson and Ostro, 1999]). The dashed one corresponds to the orbit-averaged YORP effect. Note linear growing of $(P - P_0)/P_0$ and corresponding quadratic dependence of phase $O - C$.

derived by Ďurech: $\lambda = 51.5°$, $\beta = -57.3°$. The volume Ďurech's model was scaled to the same volume as model of [Hudson and Ostro, 1999]. Also, we made rotation of body-fixed frame to the system of principal axis of inertia tensor.

The possibility of detection of the YORP effect on (1620) Geographos is shown in Figure 3.23. Here we used the shape model of Ďurech. The next opportunity to observe Geographos during its approach will be in 2008. The YORP effect produces a phase lag $\sim 13°$ between 1994 and 2008. Thus, if the shape derived by Ďurech is the correct one[8], we can expect the successful detection in 2008.

### Discussion

We have shown that the YORP component $T_\omega$ causes the changes of the angular velocity $d\omega/dt$ (or the phase shift), which can be measured directly. Moreover, the YORP component $T_\omega$ does

[8]The shape of [Hudson and Ostro, 1999] leads to phase lag $\sim 1.3°$ between 1994 and 2008. This is not enough to successful detection in 2008.

not depend on thermal conductivity $K$. Thus the principal moment $C$ of inertia and the bulk density $\rho_b$ of the asteroid can be determined by measured $d\omega/dt$ together with the YORP effect model.

## 3.5 Summary

- The YORP effect affects both the spin period and the obliquity of the asteroids with certain amount of the windmill asymmetry. The shape and obliquity are the key quantities affecting the YORP effect.
- A typical YORP evolution timescales are shorter than collisional timescales (for asteroids smaller than several tens of kilometers in the Main Belt). The YORP effect can double the rotation period of 2 km Main Belt asteroid in $\approx$12 Myr.
- The obliquity-affecting YORP component $T_\epsilon$ depends on the thermal conductivity $K$ of surface material, while the component $T_\omega$, affecting the angular velocity, is almost $K$-independent.
- There is a wide variety of possible YORP evolution paths of the spin states. The most probably, the spin axis is driven to be perpendicular with respect to the orbital plane.
- The spin period can be both accelerated (maybe up to a bursting limit and possible formation of binary asteroids) or decelerated (to the state of very slow tumbling rotators).
- The spin period of bodies with obliquity $\epsilon \simeq 55^\circ$ and $\epsilon \simeq 125^\circ$ is not affected by the YORP effect.
- We computed the YORP effect for several asteroids, assuming their actual shape and orbital, rotational and physical configuration, and showed possibilities of a successful YORP effect detection via change of the rotation period or a phase shift of the lightcurve. We predict the successful direct detection of the YORP effect for (6489) Golevka, 1998 KY26, (25143) Itokawa and (1620) Geographos in the near future.

# Chapter 4

# The Yarkovsky effect

## 4.1 Introduction

### 4.1.1 The principle of the Yarkovsky effect

The Yarkovsky effect is a relatively weak non-gravitational force arising from anisotropic thermal emission from the surface of a body, which is heated by the absorption of the solar radiation. The principle of the effect can be explained as follows: Let us assume an asteroid orbiting about the Sun and rotating about the spin axis perpendicular to the orbital plane. The surface of the body absorbs solar radiation[1] which heats it up. Due to the finite thermal inertia of the surface material the temperature follows the insolation with some delay, as can be seen in Figure 4.1. This causes the "morning" hemisphere is cooler and the "evening" one is warmer. The surface emits thermal radiation which takes certain amount of momentum away. This causes a repulsive *thermal force*, which direction is somewhat shifted from the direction opposite to the Sun due to disbalance of temperature between the morning and evening hemispheres. The transverse component of this force, parallel to the velocity vector of the asteroid, then causes (according to the laws of celestial mechanics) a change of the semimajor axis of the orbit. If the body's rotation is prograde, its semimajor axis increases, if it is retrograde the semimajor axis decreases. (The body spirals inwards or outwards.) The above described effect is called the *Yarkovsky diurnal effect* (see Figure 4.2a). The strength of this effect depends on the distance from the Sun, the diameter of the body, its mass, thermal parameters of the surface (the thermal conductivity $K$, thermal capacity $c$, surface density $\rho_s$), the speed of rotation and the obliquity.

Another component of the Yarkovsky effect is connected with the orbital motion about the Sun and, consequently, it is called *seasonal*. It is independent on the rotation speed and always leads to the semimajor axis decay. It is caused by the effect of thermal inertia during the revolution about the Sun. The necessary condition is the obliquity not equal $0^\circ$ or $180^\circ$. Let us expect the Sun is shining on the northern hemisphere during the summer (see Figure 4.2b). In the autumn equinox the Sun illuminates both hemispheres equally, but due to the thermal inertia the northern one is warmer and then the resulting thermal force is shifted from the direction opposite to the Sun and against the direction of motion. A similar situation occurs in the spring equinox: The southern hemisphere is warmer than northern one and the thermal force again aims against the velocity vector. In real situations, the Yarkovsky effect is a combination of the above mentioned components.

[1] The momentum of this absorbed radiation together with the radiation reflected due to non-zero albedo give rise to the solar radiation pressure. But this force has direction opposite to the direction towards the Sun and its effect overall averaged over orbital period only decreases the solar gravitation force.

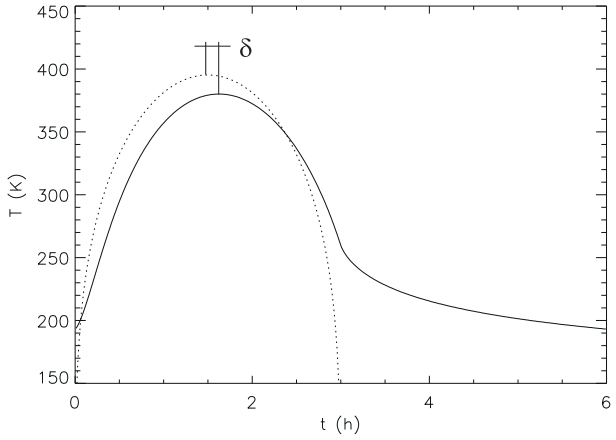


Figure 4.1: The delay $\delta$ between the maximal insolation (dotted line) and the maximal temperature (solid line) due to the thermal inertia of the surface material. The figure corresponds to an equatorial surface element during one rotation cycle lasting 6 hours.

### 4.1.2 The Yarkovsky effect in the Solar System

The Yarkovsky effect plays an important role in the dynamics of meter to multi-kilometer sized bodies in the Solar System. It helps us to explain many observed (and previously puzzling) facts. Some of them we shall briefly mention here.

**Delivery of meteorites to the Earth.** The first application of the Yarkovsky effect was an explanation of the meteorite transport from the Main Belt to the Earth's vicinity (e.g., [Öpik, 1951], [Peterson, 1976]). Recently the subject was studied for example by [Farinella et al., 1998] and [Vokrouhlický and Farinella, 2000]. According to the model of [Vokrouhlický and Farinella, 2000], the asteroidal fragments, ejected after the disruption of parent body, slowly spiral due to the Yarkovsky effect. A typical semimajor axis drift rate $da/dt$ is from $\sim 10^{-4}$ to $\sim 10^{-2}$ AU/Myr. It depends mainly on diameters of fragments, densities and thermal parameters of the surface. The obliquity also affects the strength and direction of Yarkovsky effect. During this stage (that can take from several Myr up to several 10 Myr) the fragments may secondary undergo collisions, causing changes of their spin axes or even further fragmentation. Finally the fragments reach a powerful gravitational resonance (3:1 mean motion resonance with Jupiter or $\nu_6$ secular resonance), where they are captured and their excentricity rapidly increases up to 1. This stage lasts only a few Myr. Most bodies then fall directly into the Sun and only less than 1% hit the Earth. There is a good agreement between the calculated transport timescales and the observed cosmic ray exposure times of various meteorite types (they differ for various materials), and it is also possible to explain the observed total meteorite flux.

**Delivery of small asteroids to the near Earth space.** It was recognized that most of the near-Earth asteroids originate in the Main Belt from where they are delivered to the Earth's vicinity via powerful resonances. [Bottke et al., 2002] estimated that approximately 220 objects per Myr with absolute magnitude $H < 18$ (i.e., with diameter $D \gtrsim 1$ km) must escape from the inner Main Belt in order the population of NEAs to be in steady state. Refilling of new asteroids to the resonances can be explained by a semimajor axis drift caused by the Yarkovsky effect. [Morbidelli and Vokrouhlický, 2003] studied the transfer of bodies towards $3:1$ and $\nu_6$ resonances, assuming random reorientation of spin axes due to collisions and the YORP effect. Their model gives the same flux as derived by [Bottke et al., 2002]. Moreover, due to the

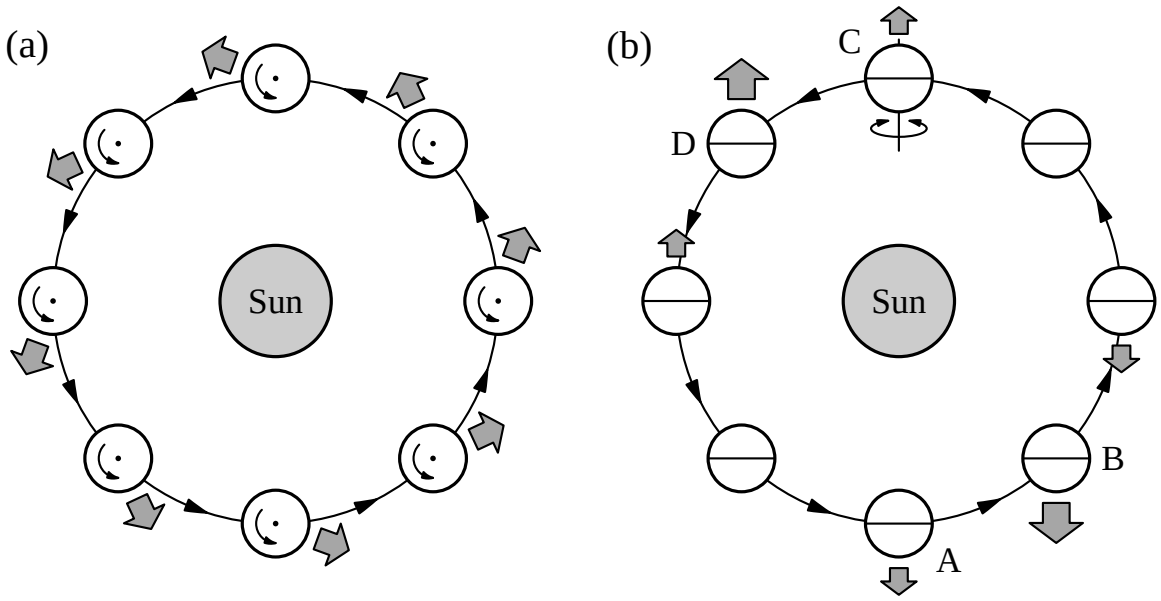


Figure 4.2: The principle of Yarkovsky effect: (a) diurnal and (b) seasonal component. More explanation in the text. (The autor of this figure is M. Brož)

Yarkovsky effect sensitivity on size, they are able to explain the difference between the cumulative size distribution of main belt asteroids $N(>D) \propto D^{-1.3}$ and thet of the near-Earth asteroids $N(>D) \propto D^{-1.75}$. [La Spina et al., 2004] also noticed the dominance of the Yarkovsky effect over collisions in injecting the bodies into resonances. They found that retrograde rotators[2] among NEA's are more numerous than the prograde ones. This is most probably caused by the fact that the $\nu_6$ resonance transport route is more effective than the $3:1$, and because the $\nu_6$ is located inside the Main Belt, the bodies have to drift inwards (and thus have retrograde spins).

**Evolution of asteroid families due to the Yarkovsky effect.** Asteroid families originate from a catastrophic collisions or cratering event of a parent body that produced fragments, which we can observed today as clusters in the space of proper elements $a_p$, $e_p$, $\sin i_p$; they also exhibit similar spectral properties. Subsequent evolution is driven by the Yarkovsky effect, mutual collisions of the fragments and planetary perturbations.

For example [Bottke et al., 2001] investigated the evolution of the Koronis family. They explain the observed shape in $(a, e, \sin i)$ space evolution in three steps. Firstly, the catastrophic disruption produces multi-kilometer fragments with random orientation of spin axes. Next, their semimajor axes evolve due to the Yarkovsky effect. The fragments also interact with numerous weak resonances, which results in the changes in eccentricity. The most important of them is the secular resonance $g + 2g_5 - 3g_6$, located at 2.92 AU, that typically increases the eccentricity of passing asteroids, producing the separation of Koronis family into two parts. Finally, if the body reaches the powerful resonances 5:2 or 7:3, its eccentricity and inclination rapidly increases, causing an ejection from the Solar System, an impact on the Sun or a planet.

[Vokrouhlický et al., 2006b] studied the structure of the Eos family. They found that after the primary collision, a compact family arose and it consequently have evolved by the Yarkovsky effect and by planetary perturbations. The fragments, which were driven by the Yarkovsky effect to the smaller semimajor axes and encounter $7:3$ mean motion resonance with Jupiter were

[2] 15 from 21 bodies with known obliquity rotates in a retrograde sense.

removed. This explains the sharp boundary of the family located exactly at the above mentioned resonance. On the other side the fragments driven outward from the Sun meet a bit weaker 9:4 resonance and only some of them pass it. By this scenario they are able to explain the asymmetric distribution of the family members with respect to the 9:4 mean motion resonance with Jupiter. They also estimated the age of this family to be $1.3^{+0.15}_{-0.2}$ Gyr.

[Vokrouhlický et al., 2006a] developed a method for determination of ages of asteroidal families on the basis of the Yarkovsky/YORP maturity. They determined the ages for families Astrid, Erigone, Massalia and Merxia, as well as their initial dispersion velocities of fragments after the primary collision.

**Detection of the Yarkovsky effect.** The first measurement of the Yarkovsky force was achieved by observations of the drag of satellite Lageos from 1976 to 1987 (e.g., [Rubincam, 1990]).

[Vokrouhlický et al., 2000] studied a possibility of direct detection of the Yarkovsky effect via precise orbit determination of near-Earth asteroids. Since the Yarkovsky perturbation accumulates quadratically with time, they predicted a successful detection on several asteroids (namely (6489) Golevka, (1620) Geographos, (1566) Icarus) with orbits determined by radar ranging during their next apparitions. In May 2003 the radar ranging of (6489) Golevka was made during its close encounter with the Earth and non-gravitational perturbation was detected [Chesley et al., 2003]. This perturbation corresponds to the predicted shift due to the Yarkovsky effect and allows to estimate the bulk density of Golevka as $2.7^{+0.4}_{-0.6}$ g/cm$^3$ and thermal conductivity as 0.01 W/m/K.

Further detections of the Yarkovsky effect for more near-Earth asteroids are expected in the near future [Vokrouhlický et al., 2005a]. An interesting opportunity to detect the Yarkovsky effect (both on the motion of centre of mass and on relative motion of components) appears in the case of near-Earth binary asteroids [Vokrouhlický et al., 2005b].

[Nesvorný and Bottke, 2004] studied the young Karin family, with age only 5.8±0.2 Myr, and on the basis of convergence of orbits they determined the Yarkovsky effect for its $\sim 70$ members. The magnitude of the measured Yarkovsky orbital drift agreed with the theoretical predictions. They also determine the surface conductivity of asteroidal fragments as $\sim 0.1$ W/m/K.

[Chesley et al., 2006] focused on the small near-Earth asteroid 1992 BF. Orbital calculations based on the observations from 1992–2005 poorly fit the pre-discovery observations from 1953, but with the Yarkovsky effect included into the force model they were able to fit the complete observational arc 1953–2002. The resulting semimajor axis drift is $da/dt = -(11 \pm 2) \times 10^{-4}$ AU/Myr, which corresponds to the Yarkovsky effect with a retrograde spin axis orientation with obliquity $120^\circ - 180^\circ$.

### 4.1.3 The theory of the Yarkovsky effect

The computation of the Yarkovsky effect usually consists of the determination of asteroid's surface temperature, the computation of the corresponding thermal force and the final determination of its effect on asteroid's orbit. The surface temperature $T$ is calculated from the heat diffusion equation (HDE for short) inside the body (see Appendix A)

$$\rho\, c\, \frac{\partial T}{\partial t} = \nabla(K \cdot \nabla T), \tag{4.1}$$

where the density $\rho$, the thermal capacity $c$ and the thermal conductivity $K$ describe the thermal properties of asteroid material. The HDE is connected with the surface boundary condition:

$$K\, \nabla T \cdot \mathbf{n} + \epsilon \sigma T^4 = (1 - A)\, \mathcal{E}. \tag{4.2}$$

Here, $\mathbf{n}$ denotes the outer normal to the surface, $\epsilon$ the emisivity, $\sigma$ the Stephan–Boltzmann constant, $A$ the albedo and $\mathcal{E}$ incident solar flux. This equation is essentially the energy conservation law: The first term represents the energy conducted from the surface to the interior of the body, the second one is the energy taken away by thermal radiation and the right hand side term represents the absorbed solar energy. The thermal force $\mathbf{f}_{\mathrm{th}}(t)$ acting on a body can be determined by Equation (2.11). Knowing the force we can obtain the change of the semimajor axis $a$ of asteroid's orbit due to the Yarkovsky effect by Gauss equation

$$\frac{da}{dt} = \frac{2}{n^2 a\, m}\, \mathbf{f}_{\mathrm{th}}(t) \;\cdot\; \mathbf{v}(t), \tag{4.3}$$

where $\mathbf{v}(t)$ denotes the velocity vector of the asteroid, $m$ its mass and $n$ the mean motion.

As mentioned in Section 4.1, the key phenomenon controlling the strength of Yarkovsky effect is an anisotropic thermal radiation from asteroid's surface caused by thermal lag due to non-zero thermal inertia of the asteroid's surface material. As we shall see, the Yarkovsky effect is not so sensitive to the asteroid's shape as the YORP effect.

The heat diffusion problem can be solved analytically or numerically. In analytical theories the boundary condition is often linearized (e.g. [Vokrouhlický, 1998a], [Vokrouhlický, 1999]). Moreover, the analytical theories assume (i) spherical objects, (ii) circular orbits, (iii) uniform rotation, (iv) constant thermal parameters. Several attempts to remove these constraints were made. For example [Vokrouhlický, 1998b] took into account the effects of non-sphericity for the Yarkovsky diurnal effect, [Vokrouhlický and Brož , 1999] computed the seasonal effect assuming a regolith layer above the higher conductive core and [Vokrouhlický and Farinella, 1999] presented a semianalytical theory of seasonal effect which is able to involve elliptical orbits.

The numerical approach allows to eliminate all the above mentioned constraints, but it may be very time-consuming (it depends on the precision and complexity of the model). The numerical model was used for prediction of Yarkovsky orbital drift of (6489) Golevka [Chesley et al., 2003]. In [Vokrouhlický et al., 2005a] the Yarkovsky effect on irregularly shaped (1620) Geographos and thumbling (4179) Toutatis was also computed numerically, as well as in the case of binary asteroid 2000 DP107 [Vokrouhlický et al., 2005b].

## 4.2 Yarkovsky diurnal effect on irregularly shaped objects

*This section is based on the poster [Čapek and Vokrouhlický, 2002] presented at the ACM conference 2002 in Berlin.*

Analytical theories of the Yarkovsky effect usually assume spherical objects and rely on linearized surface boundary condition of the HDE. Our goal is to remove both simplifying assumptions by solving the heat diffusion problem numerically for an arbitrarily shaped body. Here we present the comparison of results obtained by an analytic theory and those of numerical model. We proved that (i) the Yarkovsky effect is not very sensitive to the exact asteroid's shape and (ii) the linearized analytical theory is a good approximation.

### 4.2.1 Numerical model

Our approach can be briefly described in the following four steps:

1. For a body described by a polyhedron, with typically several thousands of triangular surface facets, we determine the insolation of a given surface element, including effects of self-shadowing between different surface elements (see Appendix B). The time step is 1 s, which corresponds to only $1'$ of rotation phase.

2. With this insolation, we solve the one-dimensional HDE during one rotation cycle from surface to depth of $15\ell_d$ (see Appendix A). The initial condition is derived from the mean insolation.

3. We repeat the previous scheme (with the initial condition corresponding to the temperature determined in the previous turn), until the convergence of the HDE solution is attained. Usually, we require the uncertainty of the surface temperature is less than 0.1 K.

4. With the converged solution we compute the corresponding mean Yarkovsky force acting on each surface element according to Equation (2.9). The Yarkovsky force is then given by a sum over all surface elements. The mean rate of change of the semimajor axis is given by the corresponding Gauss' equation

$$\frac{da}{dt} = \frac{2}{n}\,\mathbf{f}_{\rm th}\cdot\mathbf{e}_t \tag{4.4}$$

   Note that because of the assumption of zero eccentricity and obliquity, it is sufficient to evaluate the Yarkovsky effect at a single point only during its revolution around the Sun. Here, $n$ denotes mean motion, $\mathbf{e}_t$ the along-track vector of the orbit $\mathbf{f}_{\rm th}$ the Yarkovsky force per unit mass.

### 4.2.2 Analytical vs. numerical approach for a sphere

As a test of our method, we first computed the diurnal Yarkovsky drift on a sphere, both analytically and numerically. We assume a circular orbit with semimajor axis $a = 2.5$ AU, the rotation period 6 h, the radius 1 km, the bulk and surface density $\rho = 2500\,\mathrm{kg/m^3}$, thermal capacity $c = 680\,\mathrm{J/kg/K}$ and zero obliquity. Thermal conductivity of the surface regolith was varied from $10^{-9}$ to $10^{2}\,\mathrm{W/m/K}$. Analytical model was adopted from [Vokrouhlický, 1999]. Numerical approach uses a "sphere" consisting of 1004 surface triangular facets.

The resulting Yarkovsky orbital drift as a function of the thermal conductivity, computed by the analytical and numerical theory, can be seen in Figure 4.3. The most likely values of $K$ (as well as the peak of $da/dt$) inferred from infrared observations of small NEA's are in the interval

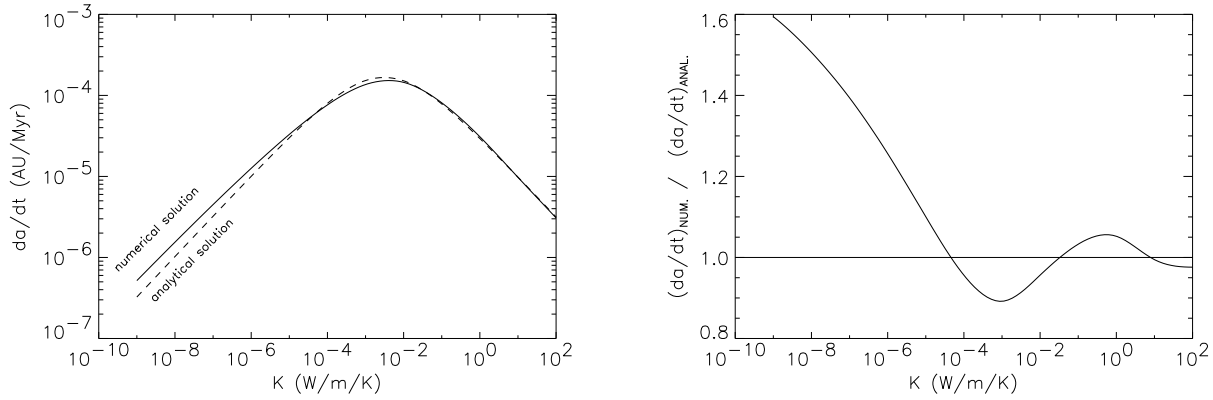


Figure 4.3: Left: The diurnal Yarkovsky orbital drift $da/dt$ as a function of the thermal conductivity $K$ for a sphere with radius 1 km and zero obliquity. The solid line corresponds to the numerical solution of the HDE and the dashed line to the analytical one. Right: The ratio between the Yarkovsky orbital drift computed numerically and analytically as a function of the thermal conductivity for the same sphere.

$0.001 - 0.1$ W/m/K [Delbò et al., 2006]. The results of numerical and analytical model is shown in Table 4.1.

A comparison of Yarkovsky orbital drift $da/dt$ computed numerically and analytically is shown in Figure 4.3 right. It can be seen that the amplitude of ratio of numerical and analytical results is decreasing with increasing thermal conductivity. This is caused by the fact, that due to great thermal variations in the case of low conductivity, the analytical linearization of HDE fails and produces wrong results. Nevertheless, the analytical results are only 1.6 times smaller for conductivity $10^{-9}$ W/m/K. For the realistic values of thermal conductivity ($K > 10^{-4}$) the difference is less than 10%.

### 4.2.3 Irregularly shaped bodies vs. sphere

We tested the calculations of the Yarkovsky effect for irregular bodies on a sample of 100 Gaussian random spheres (see Appendix), all having the same mass as a sphere with radius 1 km and density 2500 kg/m$^3$. We computed the Yarkovsky orbital drift assuming the thermal conductivity $10^{-3}$ and $10^{-2}$ W/m/K, keeping other parameters as above for the spherical body. The resulting distributions of $da/dt$ are shown in Figure 4.4.

The analytical result systematically overestimates the semimajor axis drift, both with respect to the numerical solution for a sphere and with respect to the mean value over the Gaussian spheres sample. Quantitative results are summarized in Table 4.1.

The analytical theory thus gives higher values by a factor of 1.25 or 1.19. Overall, however,

| K (W/m/K) | $10^{-3}$ | $10^{-2}$ |
|---|---|---|
| numerical model (the mean value for GRS) | $1.23\times10^{-4}$ | $1.27\times10^{-4}$ |
| numerical model (sphere) | $1.36\times10^{-4}$ | $1.45\times10^{-4}$ |
| analytical model (sphere) | $1.53\times10^{-4}$ | $1.52\times10^{-4}$ |

Table 4.1: The diurnal Yarkovsky semimajor axis drift $da/dt$ in the units of (AU/Myr) computed by numerical and analytical model. See the text.

this difference is comfortably small so that the results of the linearized analytical theory can be used for modelling statistical parameters of the meteorite transport, the origin of NEAs, evolution of asteroid families and for simillar applications.

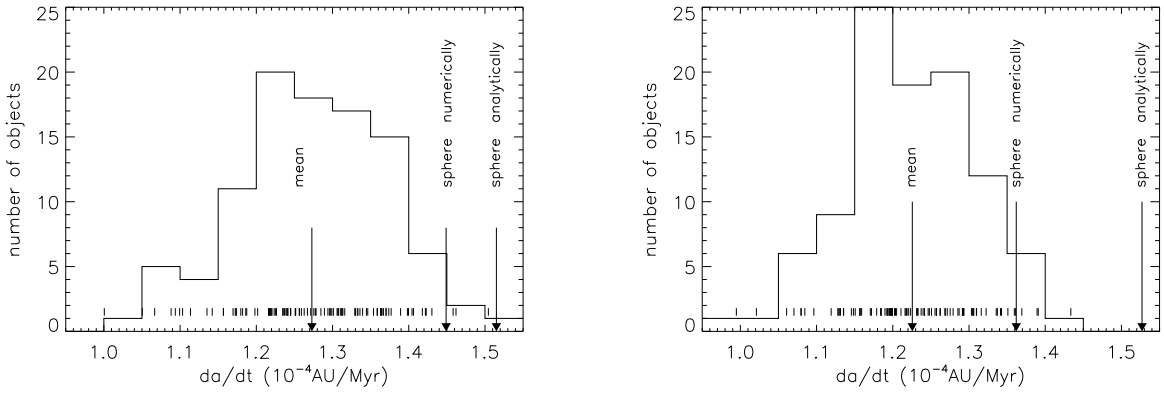


Figure 4.4: The distribution of the diurnal Yarkovsky orbital drift computed for 100 Gaussian random spheres with zero obliquity. Left plot corresponds to the thermal conductivity 0.01 W/m/K and right one to 0.001 W/m/K. The symbols at the bottom of the plot represent actual individual values of $da/dt$.

## 4.3 Yarkovsky effect on individual bodies

### 4.3.1 (6489) Golevka – the direct detection of the Yarkovsky effect

*In the following text we describe our computations which were used for the prediction and detection of the Yarkovsky effect on asteroid (6489) Golevka ([Chesley et al., 2003]).*

(6489) Golevka (1991 JX) is a $\sim 500\,\mathrm{m}$ size Apollo-type object with an orbit close to the $3:1$ mean motion resonance with Jupiter and also near to the $1:4$ resonance with the Earth. It was discovered during a close encounter with the Earth on May 10, 1991 [Helin et al., 1991]. A large international observing campaign during its apparition in 1995 allowed to determine the spin vector, period of rotation, shape model and other physical properties, as well as precise orbit [Mottola et al., 1997], [Hudson et al., 2000].

[Vokrouhlický et al., 2000] investigated a possibility of detecting of the Yarkovsky effect via precise orbit determination of near-Earth asteroids. They showed that such a detection is possible only using an accurate radar astrometry at several apparitions. The radar observations must cover sufficiently long time span to accumulate Yarkovsky perturbations, which depend quadratically on the time. In the case of Golevka they predicetd the Yarkovsky orbital drift $da/dt \simeq -6\times10^{-4}\,\mathrm{AU/Myr}$ (assuming thermal conductivity $K = 0.01\,\mathrm{W/m/K}$) and corresponding displacement of 15.2 km, with respect to the purely gravitational model of orbital evolution, during time interval between apparition in 1991 and 2003. On the basis of known astrometric observations they determined the initial state vector and its uncertainity. Then they propagated it using the pure gravity model and also the model that included the Yarkovsky force. For the time of the close encounter in 2003 they determined $3\sigma$ uncertainity ellipses in the range ($R$) vs. range-rate ($dR/dt$) plane. (These quantities are directly observable by radar.) They showed that the ellipsoids corresponding to standard and Yarkovsky-included model are shifted by $\sim 15\,\mathrm{km}$ and are well separated. They concluded that the Yarkovsky effect could be dected by radar ranging during 2003 approach.

On the basis of this prediction, Golevka was observed by radar facility of Arecibo on May 24, 26 and 27 2003 and the Yarkovsky semimajor axis drift effect was successfully detected [Chesley et al., 2003]. In this case the Yarkovsky effect was modeled by our numerical method for various thermal parameters as is described below. In the propagation of the uncertainity ellipses, they took into account uncertainities of astrometric measurements, planetary and small bodies masses and Yarkovsky modeling. The resulting $3\sigma$ uncertainity ellipses were well separated again. With the best fitting values of the surface conductivity and bulk density[3] $K = 0.01\,\mathrm{W/m/K}$, $\rho_b = 2.7\,\mathrm{g/cm^3}$, the actual Arecibo astrometry of Golevka falls into the ellipse corresponding to Yarkovsky model (the offset of $\sim 15\,\mathrm{km}$ in $R$ and $\sim 5\times10^{-6}\,\mathrm{km/s}$ in $dR/dt$). In what follows we give some more details about the Yarkovsky model used in [Chesley et al., 2003].

#### The model

Unlike [Vokrouhlický et al., 2000], we have used fully numerical model which is able to take into account eccentric orbit, irregularly shaped surface of a body and precise solution of heat diffusion problem without any linearization [Chesley et al., 2003]. Some specific features of our model are described in detail in Appendices.

The shape model of Golevka represented by a 4092-hedron (see Appendix D) was taken from [Hudson et al., 2000]. We determined the insolation of all surface elements along whole elliptical orbit, including effects of self-shadowing between different surface elements (see Appendix B).

[3] $K$ and $\rho$ are fully correlated.

With this insolation, we solved the one-dimensional HDE by a two-level scheme, during one orbital period, from surface to depth of $15\ell_s$ (see Appendix A). We usually made several iterations until the surface temperature precision was better than 0.1 K. The timestep in the first level was $\sim 500$ s while in the second one only $\sim 5$ s. The spatial steps increase with the depth according to $\Delta x_k = \Delta x_0 \exp(0.1\,k)$. The initial spatial step was $\sim 0.76\,\ell_d$ in the first level and $\sim 0.0076\,\ell_d$ in the second one. Here $\ell_d$ represents penetration depth of diurnal temperature variations.

| K (W/m/K) | $10^{-4}$ | $10^{-3}$ | $10^{-2}$ | $10^{-1}$ |
|---|---|---|---|---|
| $\ell_s$ (cm) | 4.2 | 13.1 | 41.5 | 131.3 |
| $\ell_d$ (mm) | 0.5 | 1.7 | 5.4 | 17.3 |

Table 4.2: Penetration depths of seasonal ($\ell_s$) and diurnal ($\ell_d$) temperature waves as functions of the thermal conductivity $K$. The surface density was assumed 1.7 g/cm$^3$, the thermal capacity 680 J/kg/K and the period of rotation 6 h.

With the converged solution of surface temperature we computed the corresponding Yarkovsky force acting on each surface element according to Equation (2.9). The total Yarkovsky force $\mathbf{f}_{\rm th}$ is then given by a sum over all surface elements (Eq. 2.11). The mean rate of change of the semimajor axis is given by the corresponding Gauss' equation (4.3).

We used the following orbital parameters: semimajor axis $a = 2.5065$ AU, excentricity $e = 0.604317$, inclination $i = 2.277°$, argument of perihelion $\omega = 66.06°$, longitude of ascending node $\Omega = 211.502°$. The pole of rotation was $l = 202°$, $b = -45°$ (ecliptical coordinates) and corresponding obliquity $\epsilon = 134°$. Period of rotation $P_{rev} = 6.0264$ h was slightly modified to $P_{rev} \simeq 6.02666$ h in order the fraction $P_{rev}/P_{orb}$ to be an integer number[4]. The thermal capacity was $c = 680$ J/kg/K, the surface density[5] $\rho_s = 1.7$ g/cm$^3$, the bulk density $\rho_b = 2.5$ g/cm$^3$, Bond albedo $A = 0.1$ and emisivity $\epsilon = 0.9$. We assumed the thermal conductivity $K$ from $10^{-4}$ to $10^{-1}$ W/m/K.

### Results

For the given material parameters $K$, $c$ and $\rho_s$ we computed components of the Yarkovsky thermal force with respect to the inertial frame and corresponding semimajor axis drift $da/dt$. Figure 4.5 shows an example of $da/dt$ behaviour during one orbital period for $K = 0.01$ W/m/K. The orbit-averaged $da/dt$ as a function of surface thermal conductivity is shown in Figure 4.6. We also present results obtained by an analytical theory [Vokrouhlický, 1999]. We can see that both numerical and analytical approaches lead to almost the same averaged value of the Yarkovsky orbital drift for Golevka.

Due to a priori unknown thermal conductivity of the surface material, we had to compute the Yarkovsky orbital drift for a wide range of possible $K$'s from $10^{-4}$ to $10^{-1}$ W/m/K (see the discussion in Section 3.4.1).

[4] In this case $P_{rev}/P_{orb} = 5772$. Such change of the period do not affect the results, but it allows to use a simpler approach.

[5] We also made a few computation assuming the surface density 1 g/cm$^3$ and 2.5 g/cm$^3$.

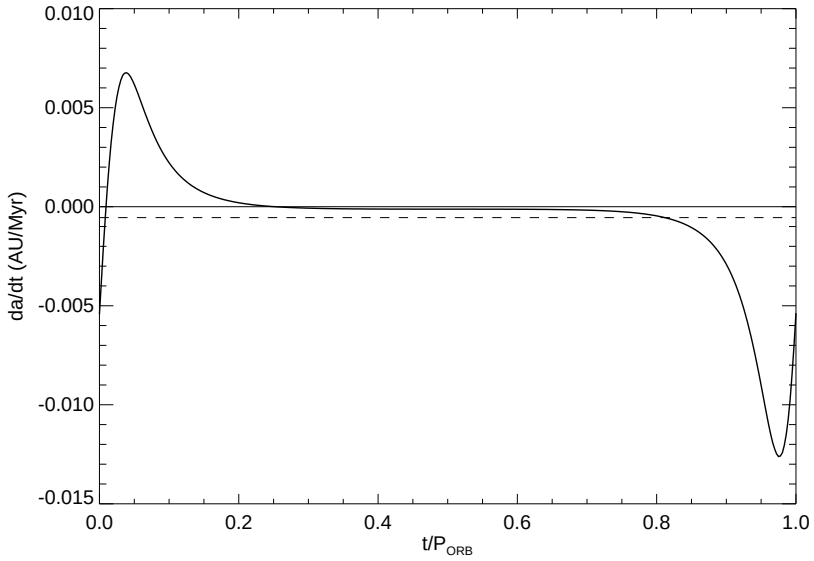


Figure 4.5: The Yarkovsky orbital drift as a function of the orbital phase ($t/P_{orb}$). The origin of time is chosen at the perihelion passage. The solid curve was computed for $K = 0.01\,\mathrm{W/m/K}$, $c = 680\,\mathrm{J/kg/K}$, $\rho_b = 1.7\,\mathrm{g/cm^3}$. The dashed one represents the average value $\langle da/dt \rangle = -5.5 \times 10^{-4}\,\mathrm{AU/Myr}$.

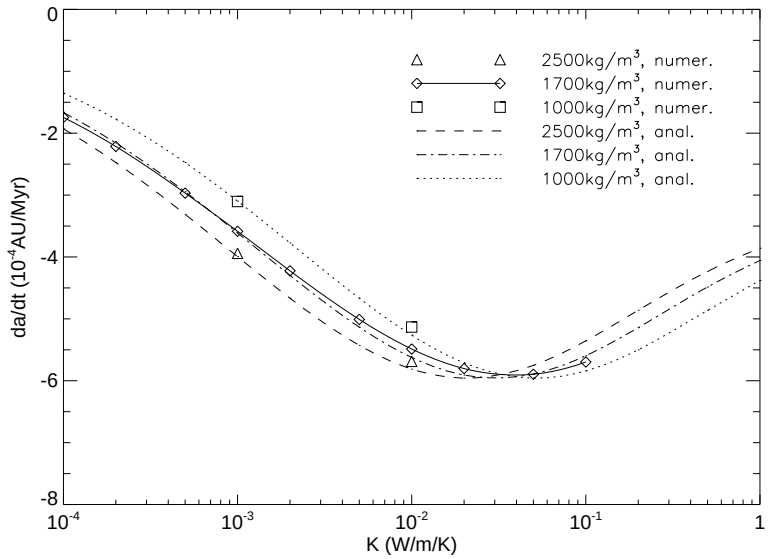


Figure 4.6: The Yarkovsky semimajor axis drift $da/dt$ according to the numerical and analytical theory as a function of the surface conductivity $K$. The solid line (with diamond symbols indicating the actually determined values) represents $da/dt$ determined by the numerical method, expecting the density of the surface material $1.7\,\mathrm{g/cm^3}$. The dash-dotted line is computed by the analytical theory, with the same density assumed. The dotted and dashed curves were computed analytically, assuming the surface density $1\,\mathrm{g/cm^3}$ and $2.5\,\mathrm{g/cm^3}$ respectively. The square and triangle symbols denote numerical results for densities $1\,\mathrm{g/cm^3}$ and $2.5\,\mathrm{g/cm^3}$ respectively.

### 4.3.2 (6489) Golevka – plausible constraints on its surface layer

*This section is based on the poster [Čapek and Vokrouhlický, 2005b] presented at the conference ACM 2005 in Búzios, Brazil.*

We improved our numerical model of Yarkovsky/YORP effect (which was used for example in [Chesley et al., 2003]) by taking into account spatial and temperature dependence of the thermal capacity $c$ and thermal conductivity $K$. As a result we can derive constraints on the surface properties such as regolith thickness for this asteroid.

#### The model

We assumed the same spin, orbital and shape parameters of Golevka as in Section 4.3.1. The main differences are in the thermal parameters: we assumed a the high-conductive core, composed from fresh basalt covered by a layer with low thermal conductivity ("regolith"). Moreover, we allow for temperature dependence of thermal parameters. This is discussed in detail in Section A.1.3. We adopt the temperature dependence of the thermal capacity $c$ from [Urquhart and Jakosky, 1997] as

$$c = (-0.037 + 1.19 \times 10^{-3}\,T - 1.96 \times 10^{-6}\,T^2 + 1.24 \times 10^{-9}\,T^3) \times 4186.05 \quad (\mathrm{J/kg/K}),$$

where $T$ (in Kelvins) is the temperature. The thermal capacity for a given temperature is almost the same for a wide range of stony materials. But due to the temperature dependence it can vary from $\sim 400$ to $\sim 800$ J/kg/K at aphelion and perihelion of Golevka, respectively.

The temperature dependence of the thermal conductivity $K$ was assumed as

$$K = A + B\,T^3, \tag{4.5}$$

where the term $A$ corresponds to a heat transfer by conduction and $B\,T^3$ represents a radiative heat transfer. The second term is important in materials like regolith containing voids. In the case of Golevka, the second term plays only a minor role.

The density is not affected by temperature variations. The thermal conductivity and density of the core and regolith used in our model are summarized in Table 4.3.

| | $A$ (W/m/K) | $B$ (W/m/K$^4$) | $\rho_s$ (g/cm$^3$) |
|---|---|---|---|
| regolith | $0.001 - 0.1$ | $2 \times 10^{-11}$ | 1.7 |
| core | 2.5 | 0 | 2.5 |

Table 4.3: The thermal parameters used in our model of Golevka. The $B$ term of regolith corresponds to the lunar regolith (Table 1 in [Cremers, 1972]).

The solution of the heat diffusion equation was more difficult due to the dependence of thermal parameters on the temperature. We had to modify the Crank-Nicolson scheme and find an appropriate combination of spatial and time steps (see Appendix A). This scheme is much more time consuming. We computed the Yarkovsky effect only for regolith depths $h = 1\,\mathrm{mm}$, $1\,\mathrm{cm}$, $10\,\mathrm{cm}$ and for conductivities $A = 0.001$, $0.01$, $0.1\,\mathrm{W/m/K}$. We again assumed exponentially increasing spatial step (the initial one was $0.01\,\mathrm{mm}$) and timestep $300\,\mathrm{s}$ and used polyhedral shape of Golevka (4092 surface elements).

### Results

Our results are summarized in Figures 4.7 and 4.8. Figure 4.7 shows the dependence of $da/dt$ on the regolith depth for three values of its conductivity[6] ($K = 0.1,\ 0.01,\ 0.001\,\mathrm{W/m/K}$). Focusing on the right side panel we can see the Yarkovsky effect is similar for the three conductivity values. For large regolith thickness ($h > 10\,\ell_d$) the semimajor axis drift approaches the value corresponding to infinite regolith depth, while for $h$ small (compared to $\ell_d$) it approaches the zero regolith depth limit ($-3 \times 10^{-4}\,\mathrm{AU/Myr}$ corresponding to uniform composition with $K = 2.5\,\mathrm{W/m/K}$). There is transition zone between these two limit cases, characterized by a peak of $da/dt$ for $h \simeq 4\,\ell_d$ and local minimum at $h \simeq 1/2\,\ell_d$. The left panel shows the same dependence, but the $x-$axis is in the metric units. We can notice the horizontal line corresponding to measured orbital drift $\langle da/dt\rangle \simeq 5.5 \times 10^{-4}\,\mathrm{AU/Myr}$. This measurement is consistent with our model only for some particular combinations of the regolith depth $h$ and the thermal conductivity $K$: 1.3 cm or 3 cm for $K = 0.01\,\mathrm{W/m/K}$ and 3 cm or 13 cm for $K = 0.1\,\mathrm{W/m/K}$.

More complex constraints on combination's of the regolith's depth $h$ and the thermal conductivity $K$ can be inferred from Figure 4.8, where we plot a 2D function $da/dt(h, K)$.

The measured value of $da/dt$ for Golevka is $-5.5 \times 10^{-4}\,\mathrm{AU/Myr}$ ([Chesley et al., 2003]). We assumed 10% uncertainity of this value (or our model) and marked the corresponding area (upper right part of the figure) by dots. This area denotes plausible combinations of the regolith depth $h$ and its thermal conductivity $K$, which are consistent both with our model and with measured value of non gravitational $da/dt$. We can conclude:

- If Golevka has a high-conductive (basalt) core, the thickness of the low-conductive surface layer is larger than 1 cm and its thermal conductivity is larger then $0.004\,\mathrm{W/m/K}$.
- The radiative term $BT^3$ in the thermal conductivity (Eq. 4.5) has a negligible effect on the resulting $da/dt$ for Golevka.

### Future improvements

In reality, many asteroids seems to be covered by both regolith and fresh rock. Recently we took this fact into account and developed a model with thermal parameters dependent both on depth under the surface and on the position on the asteroid's surface. Only facets with the slope[7] smaller than the angle of repose of regolith have a regolith layer above the fresh rock core; others are assumed to be regolith-free fresh rock. (See Figure 4.9.)

For example, we assumed the angle of repose 30°. Regolith parameters were: depth $h$ =1 mm, thermal conductivity $K_{\mathrm{regolith}} = (0.1 + 2 \times 10^{-11}\,T^3)\,\mathrm{W/m/K}$ and density $\rho_{\mathrm{regolith}} = 1.7\,\mathrm{g/cm^3}$ and fresh rock parameters were: $K_{\mathrm{rock}} = 2.5\,\mathrm{W/m/K}$, $\rho_{\mathrm{rock}} = 2.5\,\mathrm{g/cm^3}$ Other quantities were the same as in [Čapek and Vokrouhlický, 2005b]. We obtained the semimajor axis drift $-3.2 \times 10^{-4}\,\mathrm{AU/Myr}$. If we chose the regolith depth 100 times larger (0.1 m), we obtained the semimajor axis drift $\langle da/dt\rangle = -5.4 \times 10^{-4}\,\mathrm{AU/Myr}$. Details of this model need to be developed in the future work.

[6] In fact, it is the conductivity parameter $A$ in Equation (4.5).

[7] defined as the angle between outer normal and vector of local gravity + centrifugal acceleration

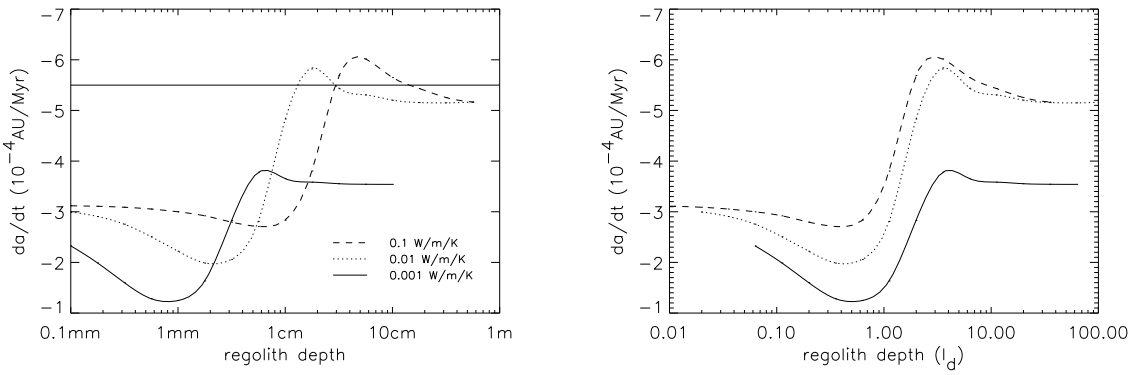


Figure 4.7: The Yarkovsky semimajor axis drift dependence on regolith depth for three values of thermal conductivity. The dashed curve corresponds to $K = 0.1\,\mathrm{W/m/K}$, dotted one to $0.01\,\mathrm{W/m/K}$ and solid one to $0.001\,\mathrm{W/m/K}$. The $x$-axis in the left panel represents the depth of regolith in metric units and horizontal line indicates the actually measured $da/dt$ on Golevka by [Chesley et al., 2003]. The right panel has $x$-axis in the units of penetration depth of diurnal temperature variations $\ell_d$. See the text for discussion.

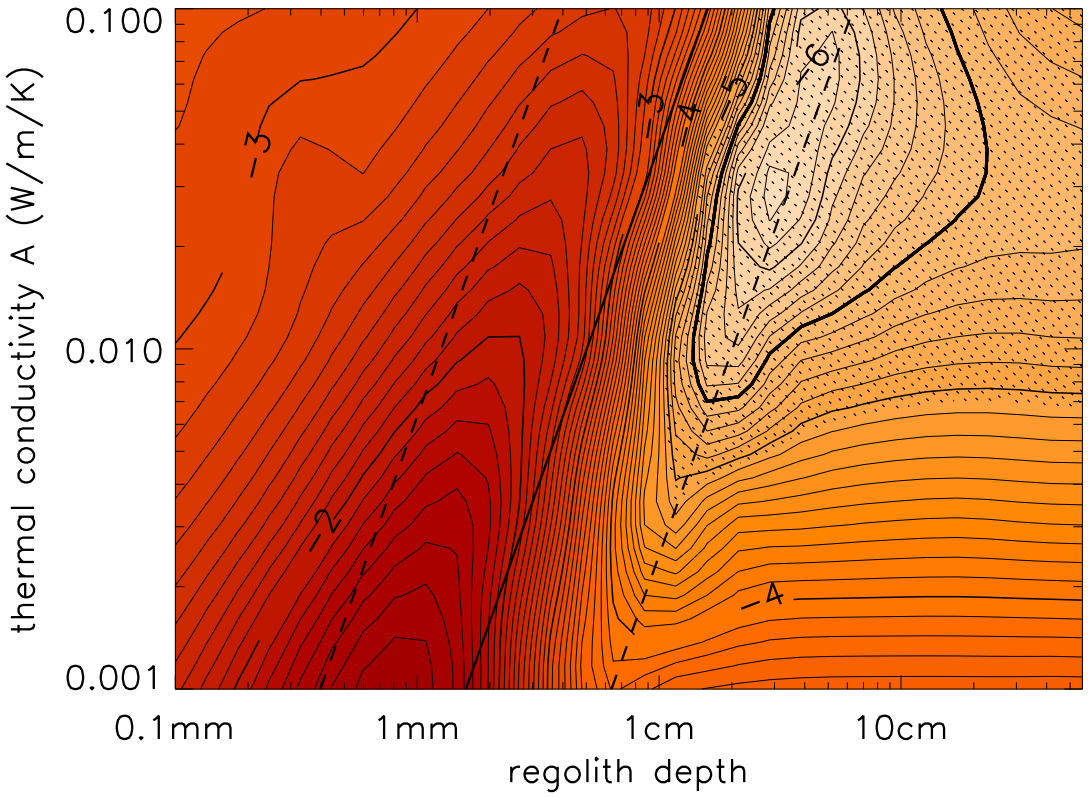


Figure 4.8: The dependence of the Yarkovsky semimajor axis drift on the depth of the regolith layer ($x$-axis) and its thermal conductivity ($y$-axis). The thick solid straight line represents the penetration depth of diurnal temperature variations $\ell_d$, while dashed ones correspond to $1/4\,\ell_d$ and $4\,\ell_d$. The thick contour corresponds to a value $-5.5 \times 10^{-4}\,\mathrm{AU/Myr}$ and dotted area indicates a 10% interval of its uncertainity.

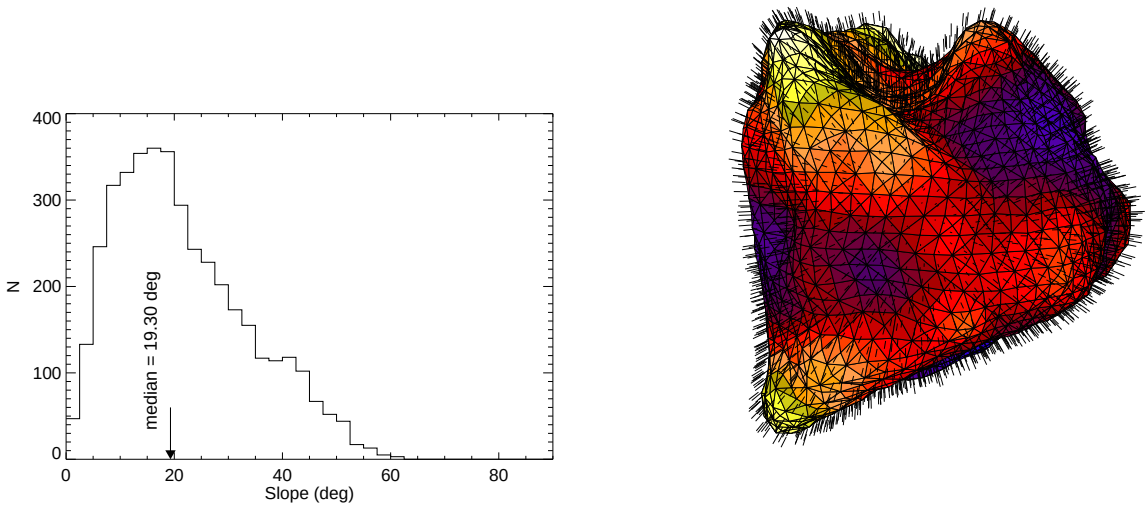


Figure 4.9: Left: The abundance of slopes for the asteroid (6489) Golevka. Right: The distribution of gravitational plus rotational acceleration across the surface of asteroid Golevka. The short lines correspond to directions and the colors to magnitudes of accelerations on the surface. (White color corresponds to the lowest value ($g_{\min} = 1.35 \times 10^{-4}\,\mathrm{m/s^2}$) and blue color to the highest value($g_{\max} = 1.86 \times 10^{-4}\,\mathrm{m/s^2}$).)

### 4.3.3 (4179) Toutatis - an asteroid with non-principal axis rotation

*This section is based on the investigation presented in [Čapek and Vokrouhlický, 2005a] and [Vokrouhlický et al., 2005a].*

(4179) Toutatis, a body with dimensions $\sim 4.6\times2.4\times1.9$ km, is an Apollo-type asteroid in the 3:1 mean motion resonance with Jupiter and in the 1:4 mean motion resonance with the Earth. During its frequent close encounters to the Earth, radar observations revealed its irregularly elongated shape [Hudson et al., 2003], non-principal axis spin state [Hudson and Ostro, 1995] and precisely determined its orbit.

[Vokrouhlický et al., 2000] studied a possibility of the Yarkovsky effect detection on this body, but several mistakes occurred in their calculations. [Vokrouhlický et al., 2005a] corrected the older results, taking into account the right shape, dimensions, the non-principal axis rotation, and solved the HDE numerically. In the following text we shall briefly describe our method used in [Vokrouhlický et al., 2005a].

#### The model

We have used a reduced shape model determined by [Hudson et al., 2000]. This model consists of 12796 surface facets (see Appendix D).

The main problem, we faced in this case, was the non-principal axis rotation of Toutatis. In the body-fixed frame, the spin axis wobbles about the long principal axis with a period of 5.367 days and this axis precedes about the angular momentum axis with period 7.420 days [Ostro et al., 1999]. The orientation of such a freely rotating body never exactly reaches the initial orientation. It can pose a problem for the HDE solution, since we do not dispose with a condition of its exact periodicity.

We first determined the orientation of Toutatis by a numerical solution of Euler equations (see [Kryszczyńska et al., 1999]):

$$A\,\dot{\omega}_A + (C-B)\,\omega_B\,\omega_C = 0, \tag{4.6}$$
$$B\,\dot{\omega}_B + (A-C)\,\omega_C\,\omega_A = 0, \tag{4.7}$$
$$C\,\dot{\omega}_C + (B-A)\,\omega_A\,\omega_B = 0, \tag{4.8}$$

$$\dot{\phi} = \frac{\omega_A \sin\psi + \omega_B \cos\psi}{\sin\theta}, \tag{4.9}$$
$$\dot{\psi} = \omega_C - \frac{\cos\theta}{\sin\theta}(\omega_A \sin\psi + \omega_B \cos\psi), \tag{4.10}$$
$$\dot{\theta} = \omega_A \cos\psi - \omega_B \sin\psi, \tag{4.11}$$

where $\phi$, $\psi$ and $\theta$ denote Euler's angles, $A < B < C$ principal moments of inertia and $\omega_A$, $\omega_B$ and $\omega_C$ are projections of spin vector to the principal axes ($A$ is the longest axis and $C$ the shortest one). The first set of equations solves for the spin axis vector with respect to the body frame whereas the second one solves for the orientation of the body with respect to the inertial frame.

We used the initial conditions listed in Table 4.4 and propagated them for one orbital period[8]. Then we determined deviations of the body axes from the initial position as a function of time and searched for the best agreement with the initial orientation. We found that Toutatis reaches

[8]The angles had been transformed due to a different orientation of our shape model.

| | | | |
|---|---|---|---|
| $\phi_0$ | $-103°$ | $\omega_A$ | $20.7°/\text{day}$ |
| $\psi_0$ | $-134°$ | $\omega_B$ | $31.3°/\text{day}$ |
| $\theta_0$ | $97°$ | $\omega_C$ | $98.0°/\text{day}$ |

Table 4.4: Initial conditions of the Toutatis's rotation taken from [Ostro et al., 1999], Table VII. The data corresponds to the date Dec 11, 1992, 9:21 UTC.

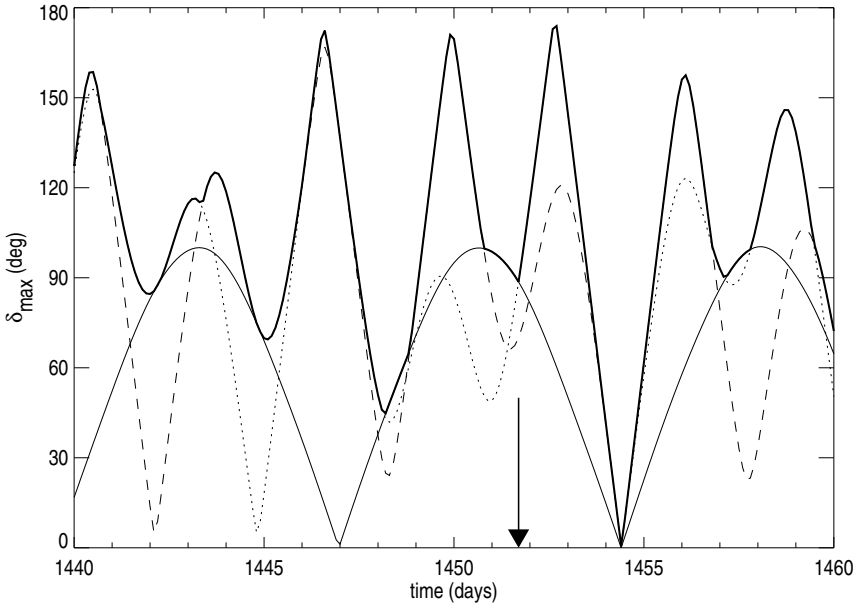


Figure 4.10: Angular deviations of the $x$ (thin solid curve), $y$ (dotted curve), and $z-$axis (dashed curve) from initial orientation in space as a function of time for asteroid (4179) Toutatis. Here we show only a short segment of 20 days near one revolution period of the asteroid. The thick solid curve denotes the maximal angular deviation. Almost the same orientation as the initial one is reached after 1454.4 days, which is very close to the orbital period 1451.7 days, denoted by the arrow.

a nearly identical orientation in the space with a period 1454.4 days, which is close to the orbital period $P_{orb} = 1451.7$ days (see Figure 4.10). This result is very surprising and we have no explanation for this fact yet. In any case, this circumstance greatly helps the HDE solution because we may use the near periodicity of Toutatis' orientation in space as a boundary condition in the time coordinate.

The semimajor axis of Toutatis' orbit was then slightly changed in order the orbital period to be exactly 1454.4 d (due to the periodic initial condition). We assumed these orbital parameters: semimajor axis $a = 2.5123$ AU, excentricity $e = 0.64038$, inclination $i = 0.466°$, argument of perihelion $\omega = 276.2°$ and ascending node $\Omega = 126.6°$.

With known orientation in space, we determined the insolation of each facet. (Including effects of self-shadowing between different surface elements – see Appendix B.) For the surface temperature determination we chose the following thermal parameters: thermal capacity $c = 800\,\text{J/kg/K}$, surface density $\rho_s = 2\,\text{g/cm}^3$, bulk density $\rho_b = 2.6\,\text{g/cm}^3$, Bond albedo $A = 0.08$ and the emisivity $\epsilon = 0.92$. We assumed values of the thermal conductivity $K$ from $5 \times 10^{-4}$ to $5 \times 10^{-1}$ W/m/K.

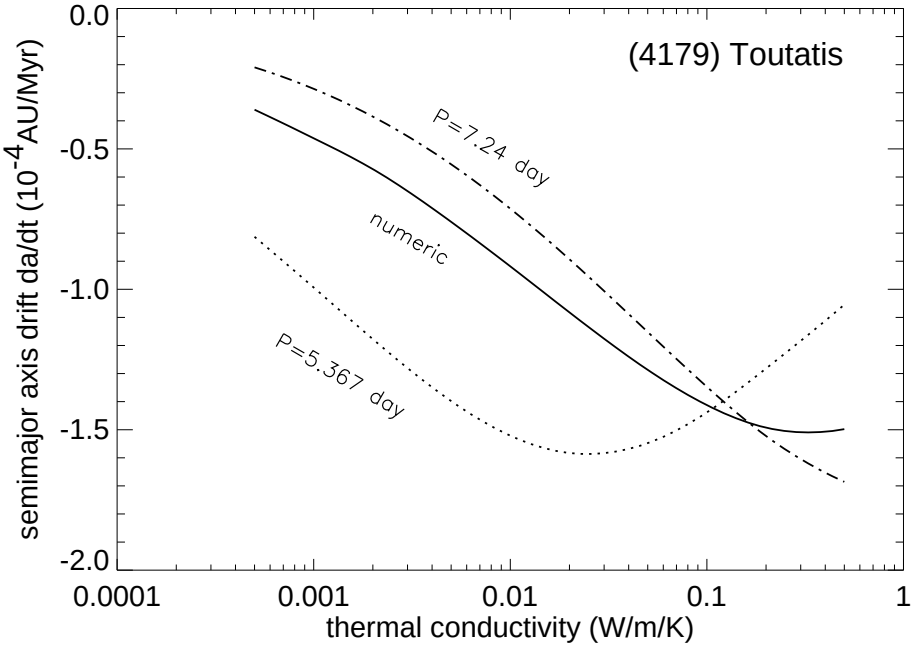


Figure 4.11: The orbit averaged semimajor axis drift for asteroid (4179) Toutatis as a function of the thermal conductivity. The thick solid line represents the result obtained by a precise numerical method, while the other two curves correspond to simplified analytical approaches. For more information see the text.

Thanks to Toutatis' slow rotation, we can solve the one-dimensional HDE by a one-level scheme, during orbital period, from the surface to the depth of $15\ell_s$ (see Appendix A). We made 5 iterations, leading to the temperature precision better than $0.009 - 0.04\,\mathrm{K}$, depending on the thermal conductivity. The timestep was 125 s (62 s in the case of $K = 5 \times 10^{-4}\,\mathrm{W/m/K}$). The spatial steps increased with the depth according to $\Delta x_k = \Delta x_0 \exp(0.1\,k)$, where the initial spatial step was $1/200\,\ell_s$.

With the converged solution of the surface temperature and the known orientation of the body we computed the corresponding Yarkovsky effect by the same way as in the case of Golevka (Section 4.3.1).

**Results**

The resulting orbit-averaged semimajor axis drift can bee seen in Figure 4.11. We compared this result with an estimation by a simplified analytical method (solving the linearized HDE). In the analytical approach, Toutatis was represented by a sphere of the same mass as real asteroid. Moreover, we assumed regular rotation about the vector of Toutatis angular momentum which has the pole $\ell = 180°$, $b = -52°$ in ecliptical coordinates. We chose two periods: 7.24 d and 5.367 d. The result of the analytical method (solving linearized HDE) with the period 7.24 d is in a surprisingly good agreement with the more sophisticated numerical theory.

We predicted the range[9] offset $+40\,\mu$s between Yarkovsky and non-Yarkovsky orbit during its encounter with Earth in October 2004, giving a good perspective of a second direct detection of the Yarkovsky effect.

Unfortunately, the detection failed so far. The measurement of the range offset led to the

[9]The Range means the quantity $2\Delta R/c$, where $\Delta R$ is the distance from the Earth (radar) to the asteroid, and $c$ is the speed of light.

value $(-23.5 \pm 4)\,\mu$s. According to [Vokrouhlický and Chesley, personal communication], this was caused by several facts: (i) the Yarkovsky force was badly incorporated into the software computing the orbit. The correct value of the Yarkovsky range offset should have been $(+16 \pm 5)\,\mu$s (instead of $+40\,\mu$s) on October 7th 2004. (ii) More importantly, the effects of asteroid perturbers, and their poorly known masses, were not taken into account, though they are very important. Thus the combination of the Yarkovsky and asteroidal perturbations leads to the range offset $(-41 \pm 18)\,\mu$s. Then the observation $(-23.5 \pm 4)\,\mu$s fits into the predicition but the difference between the "Yarkovsky" and "non-Yarkovsky" models is not statistically significant yet (due to the large uncertainities). It is yet to be determined if data from the 2008 radar ranging will allow a clear detection of the non-gravitational signal.

### 4.3.4 2000 DP107 – a binary system

*The section is based on the investigation presented in [Čapek and Vokrouhlický, 2005a] and [Vokrouhlický et al., 2005b].*

Radar observations of 2000 DP107 ([Margot et al., 2002]) revealed this object is a binary system consisting of a primary with diameter $\sim 800\,\mathrm{m}$ and a secondary with diameter $\sim 300\,\mathrm{m}$. The orbital period of the pair is $P_2 = 1.755\,\mathrm{day}$, the rotation period of the primary is $P_1 = 2.77536\,\mathrm{h}$, while the secondary has a synchronous rotation. [Margot et al., 2002] also estimated the parameters of the relative orbit: semimajor axis $a = 2622\,\mathrm{m}$, excentricity $e = 0.01$, inclination $i = 17°$, argument of perihelion $\omega = 7°$ and ascending node $\Omega = 10°$ with a large error in $\omega$ due to almost circular orbit. Binary nature of this body helped to determine the mass of the system $M = 4.6 \times 10^{11}\,\mathrm{kg}$ and corresponding bulk density of the primary component as $1.7\,\mathrm{g/cm^3}$ (we expected the same density of the secondary). The heliocentric orbit of the whole system is characterized by the semimajor axis $a = 1.3662\,\mathrm{AU}$, excentricity $e = 0.376863$, inclination $i = 8.663°$, argument of perihelion $\omega = 289.687°$ and ascending node $\Omega = 358.829°$.

We studied this system [Čapek and Vokrouhlický, 2005a], [Vokrouhlický et al., 2005b] as an example of the Yarkovsky effect influence on binary asteroid. In this cases the Yarkovsky force affects both the motion of the center of mass (COM for short) of the system and the relative motion of the components.

#### The model

Most parameters of the relative orbit and orbit of the COM were taken as above. The only exception was the semimajor axis of the COM and primary's rotation period that were changed[10] slightly, in order to the ratios between orbital period $P_{orb}$ of COM, rotation period of secondary $P_2$ and rotation period of primary $P_1$ were integers: $P_{orb} : P_2 = 332 : 1$ and $P_{orb} : P_1 = 5034 : 1$.

Next we expected the spin axes of both components are perpendicular to the plane of mutual motion. The corresponding pole in ecliptical coordinates is $\ell = 280°$ and $b = 73°$. We modeled both components as spheres with appropriate diameters, which were approximated by regular polyhedrons with 1004 triangular facets. In contrast to other studied bodies, the self shadowing of the asteroid's surfaces plays only a minor role here, but the mutual shadowing of both components during the revolution about the COM is very important and we had to incorporate this phenomenon into our model.

The thermal capacity was assumed $c = 800\,\mathrm{J/kg/K}$, the bulk and surface density $\rho_b = \rho_s = 1.7\,\mathrm{g/cm^3}$, the albedo $A = 0.1$ and emisivity $\epsilon = 0.9$. We computed the Yarkovsky effect for thermal conductivities in the range from $0.001\,\mathrm{W/m/K}$ to $1\,\mathrm{W/m/K}$.

We solved the HDE by a one-level scheme (see Appendix A) with an exponentially increasing spatial step. The exponent was 0.1 and the initial step $\Delta x_0 = 0.36\,\ell_d$ for the primary, and $\Delta x_0 = 0.18\,\ell_d$ for the secondary, where $\ell_d$ represents the penetration depth of diurnal temperature variations. The lower boundary condition lied in the depth $15\ell_s$, where $\ell_s$ is penetration depth of the seasonal temperature variations. The time step was 50 s for the primary and 200 s for the secondary. We determined the Yarkovsky acceleration $\mathbf{f}_1$ for primary and $\mathbf{f}_2$ for the secondary separately. The Yarkovsky acceleration of the whole system (COM) is given by

$$\mathbf{f}_{\mathrm{COM}} = \frac{\mathbf{f}_1 M_1 + \mathbf{f}_2 M_2}{M_1 + M_2} \tag{4.12}$$

and the Yarkovsky perturbation of the relative motion is given by:

[10] to the values $a = 1.365264\,\mathrm{AU}$ and $P_1 \simeq 2.7779\,\mathrm{h}$.

$$\delta\mathbf{f} = \mathbf{f}_2 - \mathbf{f}_1. \tag{4.13}$$

**Results**

Firstly, we focus on Yarkovsky perturbations of the COM motion. Figure 4.12 shows the orbit averaged semimajor axis drift due to the Yarkovsky effect. We also computed the Yarkovsky effect only for primary - both analytically and numerically. We can see that the contribution of the secondary to the whole effect is negligible for low conductivities and its significance increases with thermal conductivity. This can be explained by the fact that the Yarkovsky effect for the primary decreases with increasing $K$ more quickly than for the secondary due to the rapid rotation of the primary, and thus vanishing diurnal temperature variations for high $K$. We can also see the disagreement of the linearised analytical solution with the numerical one for low $K$, due to higher temperature variations, causing the HDE linearization to fail.

The time dependence of the absolute value of Yarkovsky acceleration is shown in Figure 4.13. We can see deep minima of the secondary's acceleration due to its eclipses. The eclipses are total near the perihelion and apohelion and they are partial near the quadratures. Eclipses of the primary are only partial and minima of the acceleration of this component are smaller. After the main minimum we can observe oscillations with decreasing amplitude and a period equal to the rotational period of the primary. This phenomenon is caused by the rotation of a cold spot arose from the passage of the secondary's shadow and its subsequent warming.

The Yarkovsky perturbation of the relative motion is caused by $\delta\mathbf{f}$. The most important is the component parallel to the relative motion $\delta f_\tau$. In the long time scales this component produces a linear increase of the mutual distance and a quadratic advance of the longitude in the relative orbit. The orbit averaged $\langle\delta f_\tau\rangle$ as a function of the surface thermal conductivity is shown in Figure 4.14.

The time dependence of the along-track component is shown in Figure 4.15. During a shadowing of the secondary, $\delta f_\tau$ temporarily increases. This is because the shadow at first reaches the morning side of the secondary and then this side is colder than the evening one, causing an increase of the along-track component of the Yarkovsky force. An opposite situation occurs during an emersion from the shadow. Due to thermal relaxation after occulations, the along-track component $\delta f_\tau$ does not average to zero (like the solar radiation pressure) and can produce observable effects [Vokrouhlický et al., 2005b].

We demonstrated the Yarkovsky effect is able to produce both perturbations of a heliocentric orbit of the COM and perturbations of a relative orbit of components about the common COM. Both these effects can serve to a detection of the Yarkovsky effect, but in the case of 2000 DP107, the effect on the relative motion is too small to be detected. Detection of Yarkovsky effect via its influence on the COM motion can be successful in 2016 if radar observations in 2008 are successful.

Our model is able to describe the Yarkovsky effect on binary asteroids but in this particular case, the approach is very simplified. This is mainly due to unknown orientation of spin axes, unknown shapes and due to an uncertain evolution of the rotational states and the relative orbit by tides. In the future we plan an application to better characterized systems, such as (66 391) 1999 KW4 [Ostro et al., 2006].

### 4.3.5 Discussion

We are able to determine the Yarkovsky effect for a wide variety of asteroids: simple cases of spherical bodies with semimajor axis rotation, as well as irregularly shaped bodies, tumbling

asteroids or binaries. Our model realistically describes the thermal behaviour of the surface material (the temperature and spatial dependence of the thermal parameters).

The knowledge of the Yarkovsky effect is necessary for the prediction of the asteroid's orbit. For instance, the precise knowledge of the orbit is important in the case of potential Earth impactors.

The Yarkovsky and YORP effect can be also used for determination of the thermal conductivity of the asteroid's surface and its bulk density $\rho_b$ and consequently the mass, porosity and type of the surface material (the fresh rock, regolith or mixture of them).

The independent measurement of the bulk density via direct detection of the Yarkovsky effect alone is not possible, because bulk density is coupled with the surface thermal conductivity $K$ as $\rho_b K$. However, if the Yakrovsky and the YORP effect are measured together, the independent determination of $\rho_b$ and $K$ is possible. (See Chapter 3.)

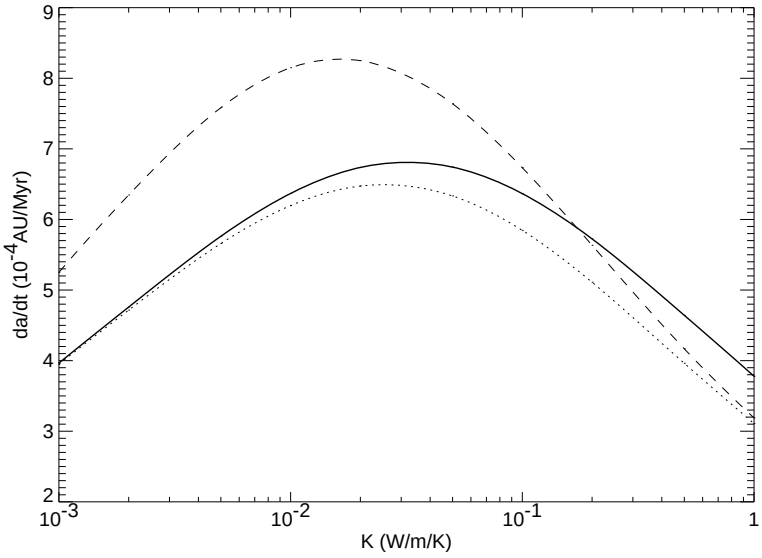


Figure 4.12: The orbit averaged semimajor axis drift $da/dt$ for 2000 DP107. The solid line represents numerical results for the whole system, while the dashed one is computed for the primary alone. The dotted line corresponds to the analytical results for a solitary primary.

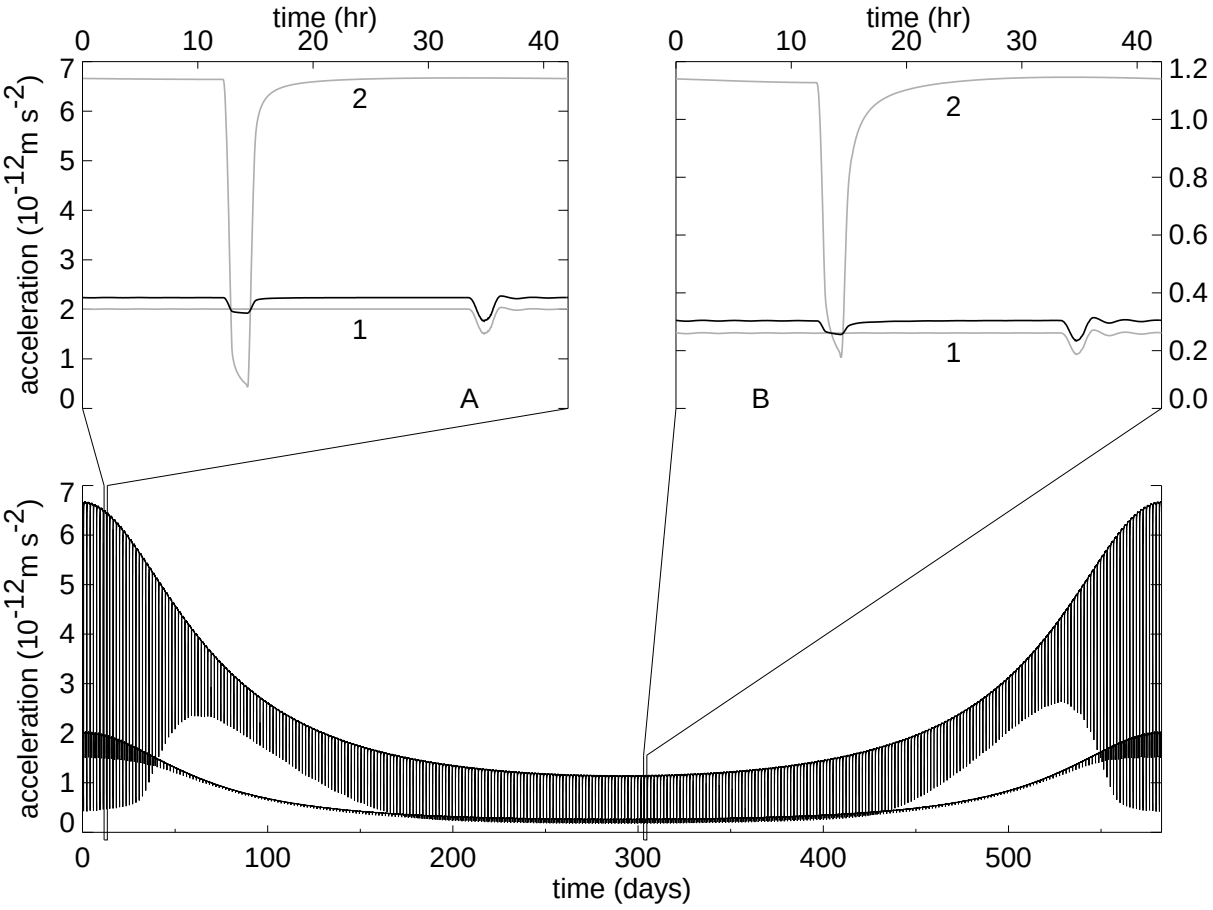


Figure 4.13: The absolute value of the Yarkovsky acceleration of 2000 PD107 as a function of time for the thermal conductivity $K = 0.01\,\mathrm{W/m/K}$. Lower figure shows the acceleration of the primary (the curve with a smaller amplitude) and the secondary (the larger amplitude) during one revolution about the Sun. Upper figures show in detail the situation near the perihelion (left) and aphelion (right) during one revolution of the components about the COM. Here the upper grey curve denoted by "2" represents the secondary, the lower denoted by "1" the primary and the black curve corresponds to the acceleration of the COM (according to Equation (4.12)). More explanation in the text.

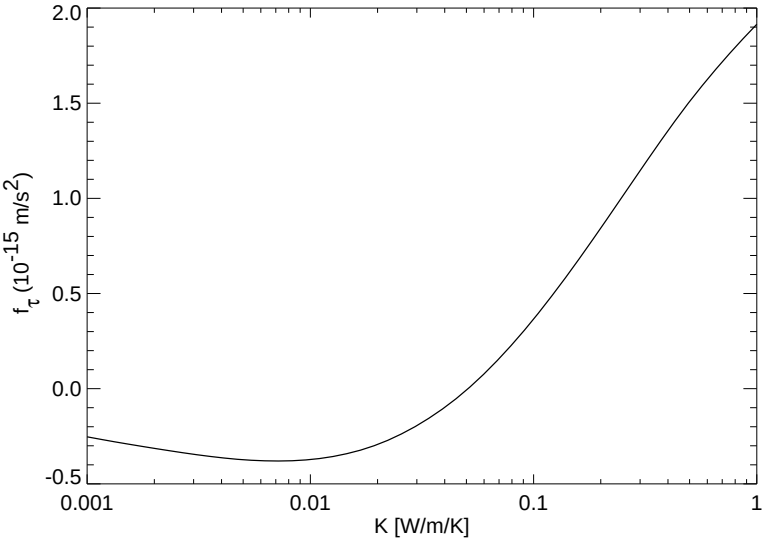


Figure 4.14: The orbit averaged along-track component $f_\tau$ as a function of the surface thermal conductivity $K$.

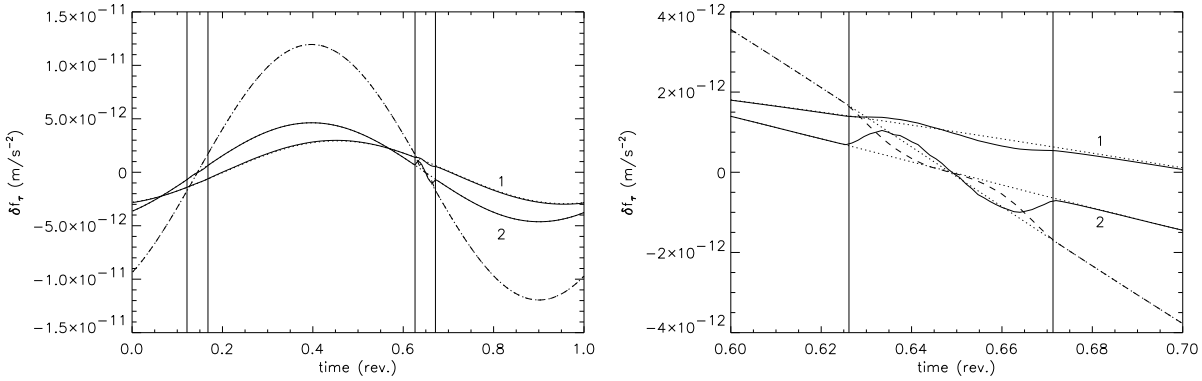


Figure 4.15: The long-track component of $\delta\mathbf{f}$ as a function of time. Left plot shows the dependence during one revolution about the COM. The vertical lines correspond to the entry and exit of occulations. The first is the occulation of the primary and the second the partial occulation of the secondary. The dashed line denotes an effect of the solar radiation pressure, the solid curve denoted by "1" corresponds to the thermal conductivity $K = 1\,\mathrm{W/m/K}$ and the solid curve denoted by "2" to $K = 0.001\,\mathrm{W/m/K}$. Right plot zooms the occulation of the secondary. Dotted curves correspond to a situation when no occulations occur.

## 4.4 Summary

- Our numerical model was used succesfully for the prediction and the following detection of the Yarkovsky effect on asteroid (6489) Golevka. It was the first direct detection of this phenomenon effect on a natural body.
- We also computed the Yarkovsky effect and estimated possibilities of the detection for several other asteroids. We are able to describe highly eccentric orbits, non-principal axis rotation (e.g., (4179) Toutatis), or mutual shadowing in components of binary systems (e.g., 2000 DP107).
- On the basis of the detected Yarkovsky orbital drift for (6489) Golevka and our model involving depth and temperature dependence of thermal parameters, we estimated the depth and thermal conductivity of the surface regolith layer.
- We compared the results of the analytical theory with our sophisticated numerical model and concluded that the analytical model mostly gives very similar results as the numerical one.
- In contrast to the YORP effect, where the shape plays a key role, we showed near complete independence of the Yarkovsky effect on the detailed shape of the body.
- As a by-product, we revealed an interesting agreement between the orbital period of the tumbling asteroid (4179) Toutatis and the period needed to its return to the initial orientation with respect to the inertial system (i.e., its "rotational" period).

# Appendix A

# The heat diffusion equation

This chapter deals with a problem of the determination of the asteroid's surface temperature, which is necessary for the calculation of the Yarkovsky force and the YORP torque. We will assume that the asteroid is thermally relaxed, this means the temperature variations are caused by insolation only. Neither radiogenic nor other sources of heat are taken into account.

## A.1 Introduction

### A.1.1 Derivation of the Heat Diffusion Equation

Any gradient of the temperature $\nabla T$ inside a body is connected with the heat flow $\mathbf{q}$ according to Fourier's law:

$$\mathbf{q} = -K\,\nabla T, \tag{A.1}$$

where $K$ $[\mathrm{W\,m^{-1}\,s^{-1}}]$ is the thermal conductivity. This heat flow through the closed surface $S$ increases an energy of the enclosed volume $V$ of a body after time $dt$ by

$$\delta\,\mathcal{Q} = -\oint_S \mathbf{q}\cdot d\mathbf{S}\,dt = \int_V \nabla\cdot(K\,\nabla T)\,dV\,dt, \tag{A.2}$$

The second law of thermodynamics is[1] (e.g. [Svoboda and Bakule, 1992]):

$$\delta\,\mathcal{Q} = T\,ds = T\frac{\partial s}{\partial t}\,dt,$$

and for the volume $V$:

$$\delta\,\mathcal{Q} = \int_V T\,\frac{\partial s}{\partial t}\,dt\,dV, \tag{A.3}$$

where $s$ is density of entropy. Together with equation (A.2) we have (assuming there is no deformation):

$$T\frac{\partial s}{\partial t} = \nabla\cdot(K\,\nabla T). \tag{A.4}$$

If there are no heat sources, as a decay of radioactive elements, and no deformations (i.e., constant volume) we can write

$$\frac{\partial s(T)}{\partial t} = \frac{\partial s}{\partial T}\frac{\partial T}{\partial t} = \rho\,\frac{c_v}{T}\frac{\partial T}{\partial t},$$

[1] We use the notation $\delta Q$ instead of $dQ$, because $Q$ depends on the integration path between initial and final state, i.e., $\delta Q$ is not a total differential.

where $c_v$ [J kg$^{-1}$ K$^{-1}$] is the specific heat capacity[2] for constant volume. Finally, together with (A.4) we can obtain the heat diffusion equation (HDE for short)

$$\rho c_v \frac{\partial T}{\partial t} = \nabla \cdot (K \nabla T), \tag{A.5}$$

which is a second order partial differential equation of parabolic type for the temperature $T(\mathbf{r}, t)$ as a function of position $\mathbf{r}$ and time $t$. Due to simplicity, we are using the notation "$c$", but it always means "$c_v$".

### A.1.2 Initial and boundary conditions

The uniqueness of the solution of the HDE requires additional equations constraining the temperature field. These are called initial and boundary conditions.

An initial condition defines temperature field in a given time $\tau$: $T(t = \tau, \mathbf{r}) = f_1(\mathbf{r})$; alternately, the initial condition can be sometimes replaced by periodic boundary condition $T(t, \mathbf{r}) = T(t + P, \mathbf{r})$, where $P$ is the constant period.

boundary condition describes the behavior of the temperature at the boundaries of the body. Here we list a few examples of the most common boundary conditions (e.g., [Isachenko et al., 1969], [Vitásek, 1987]).

- If the temperature is predefined at the boundary as a function of time, $T(t, \mathbf{r}) = f_2(t, \mathbf{r})$ for $\mathbf{r} \in \Sigma$, then it is called *the Dirichlet condition.*
- *The Neumann condition* specifies the gradient of the temperature at the boundary: $\nabla T(t, \mathbf{r}) = f_3(t, \mathbf{r})$ for $\mathbf{r} \in \Sigma$ and actually represents a contact with a defined thermal flux.
- Another type of boundary condition describes a cooling or heating of the body by a surrounding reservoir. Then the heat flux is proportional to heat-transfer coefficient $\alpha$ (W/m$^2$) and the difference between the temperature of the body's surface $T(t, \mathbf{r} \in \Sigma)$ and temperature of the reservoir $T_\rho$: $-K\nabla T(t, \mathbf{r} \in \Sigma) = \alpha(T(t, \mathbf{r} \in \Sigma) - T_\rho)$. In fact, this is a combination of Dirichlet and Newmann boundary condition.

All these boundary conditions are linear in the temperature. In the following sections we face a more complicated non-linear boundary condition, which stems from the energy conservation law on the surface, where the heat transfer by the radiation and the conduction occurs.

### A.1.3 Thermophysical parameters

In a solid material with a non-zero porosity the heat is transferred by the conduction and by the thermal radiation in the voids. The thermal conductivity $K$ can be divided into the conduction term $K_a$ and temperature-dependent radiative term $K_b T^3$:

$$K = K_a + K_b T^3. \tag{A.6}$$

The typical values of both terms for various materials are shown in Table A.1.

The thermal capacity $c$ also depends on temperature. This dependence is often approximated by a power law. [Winter and Saari, 1969] derived a model, that is appropriate for a wide range of materials (Ca-feldspar, magnesium silicate, quartz, basalt, diorite, granite) and for temperatures from few tens to $\sim 500$ K:

$$c(T) = -0.034\,T^{1/2} + 0.008\,T - 0.0002\,T^{3/2}. \tag{A.7}$$

[2] Sometimes called *thermal capacity.*

| Material | $K_a$ (W/m/K) | $K_b$ (W/m/K$^3$) |
|---|---|---|
| Moon's regolith | $0.001 - 0.002$ | $\sim 2 \times 10^{-11}$ |
| Basalt powder | $0.002 - 0.005$ | $\sim 4 \times 10^{-12}$ |
| Fresh basalt | 2.56 | 0 |

Table A.1: Typical thermal conductivities ([Urquhart and Jakosky, 1997])

[Urquhart and Jakosky, 1997] use another model for lunar materials in the range from 70 K to 400 K:

$$c(T) = -0.037 + 4.98 \times 10^{-3}\, T - 8.21 \times 10^{-6}\, T^2 + 5.19 \times 10^{-9}\, T^3. \tag{A.8}$$

The thermal capacity $c(T)$ for both models can be seen in Figure A.1.

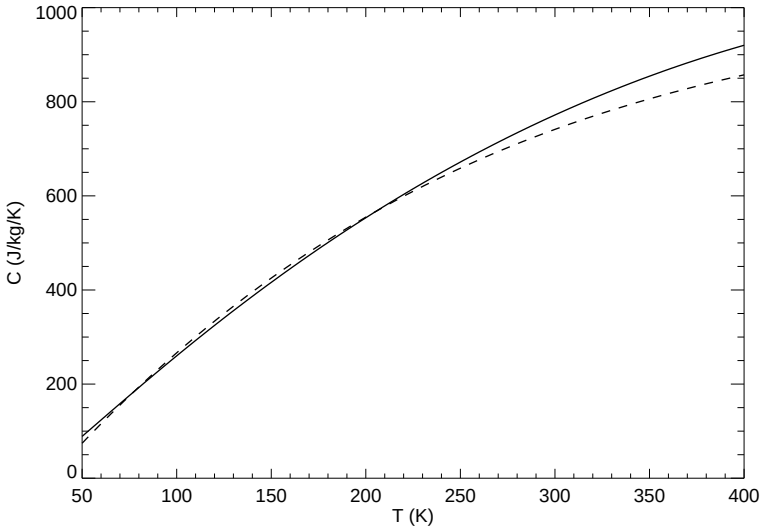


Figure A.1: Dependance of the thermal conductivity $c$ on the temperature according to [Winter and Saari, 1969] (solid) and [Urquhart and Jakosky, 1997] (dashed).

We shall demonstrate the importance of these variable thermal parameters on the example of asteroid (6489) Golevka. In the perihelion (0.99 AU), the mean temperature at the equator (for zero albedo) is approximately 297 K and the corresponding thermal capacity $c \sim 800$ J/kg/K. The mean temperature in the aphelion (4.01 AU) is 148 K, which corresponds to $c \sim 400$ J/kg/K. The value of the thermal capacity does not depend on the chemical composition of the material and it changes solely due to temperature dependence by $\sim \pm 33\%$.

If we turn our attention to the thermal conductivity, we can see that its value depends especially on the type of material, rather then on temperature. Material like Moon's regolith has $K \sim 0.00106$ W/m/K and 0.0015 W/m/K at the aphelion and perihelion respectively. For different materials the value of $K$ may differ by 3 orders of magnitude (see Table A.1).

We can conclude that the material dependence of the thermal conductivity is the most important. The knowledge of surface material and especially its $K$ is a crucial factor for correct determination of the temperature and consequently the Yarkovsky/YORP effect.

Except for the laboratory measurements of lunar or terrestrial materials ([Cremers, 1972], [Winter and Saari, 1969], [Urquhart and Jakosky, 1997]), we mention several more ways how to estimate surface thermal properties of asteroids: laboratory studies of their meteorite equivalents

[Yomogida and Matsui, 1983], direct measurements of the Yarkovsky effect [Chesley et al., 2003], or infrared observations of asteroids [Delbò et al., 2007].

For the purpose of this section we shall to introduce very useful quantity describing the thermal wave propagation, which is *penetration depth of the temperature variations*

$$\ell = \sqrt{\frac{K}{\rho c \omega}}. \tag{A.9}$$

Here $\omega$ denotes a frequency of variations of the temperature[3]. In fact, this represents a depth, where the amplitude of the surface temperature variations decreases by a factor $1/e$.

## A.2 One dimensional approach

[Vokrouhlický, 1999] presented an analytical solution of the linearized HDE in three dimensions for a spherical body. Unfortunately, the analytical solution of the HDE for irregularly shaped objects is not known. Moreover, the numerical solution of the HDE in three dimensions is unacceptably time-consuming (and computer's memory-intensive) in our applications. Fortunately, there are possibilities how to avoid the solution of the complete HDE (A.5).

If several conditions are fulfilled, the surface temperature of irregularly shaped asteroids can be determined by separate solutions of one dimensional-HDE for each surface element individually. We assume the surface of an asteroid is approximated by a polyhedron composed of a large number of triangular facets. Next we assume that

- the temparature of each surface element does not significantly affect its neighbouring elements,
- depth of the layer thermally affected by solar radiation is much smaller than size of the asteroid.

If this is fulfilled, we can determine the temperature of any surface elements separately, using one-dimensional form of the HDE:

$$\rho c \frac{\partial T}{\partial t} = \frac{\partial}{\partial z}\left(K \frac{\partial}{\partial z} T\right), \tag{A.10}$$

where $z$ coordinate represents depth below the surface[4]. This approach can be quantitatively tested by means of penetration depth of seasonal temperature variations $\ell_n$, which corresponds to Equation (A.9) with frequency equal to the mean motion $n$. The thermal variations must occur only in a relatively thin layer close to the surface, which is thin compared to the dimension of the asteroid.

Figure A.2 shows, how the depth $\ell_n$ depends on surface thermal conductivity $K$. If a main belt body ($a = 2.5\,\mathrm{AU}$) has a regolith layer with $K = 0.001 - 0.01\,\mathrm{W/m/K}$, then this depth is several tens of cm. For s body with a fresh surface ($K = 1 - 10\,\mathrm{W/m/K}$), $\ell_n$ may be several meters. The penetration depth of the diurnal temperature wave (assuming rotational period 6 hours) is about 100 times smaller than seasonal. So, our one-dimensional approach can be used for regolith covered bodies larger than several meters and regolith free bodies larger than several tens of meters.

The two boundary conditions complement the HDE. The first one arises from the energy conservation at the surface ($z = 0$):

[3] Usually diurnal and seasonal frequency, i.e., rotation frequency or the mean motion about the Sun.

[4] Its value increases from the surface into the centre of the body.

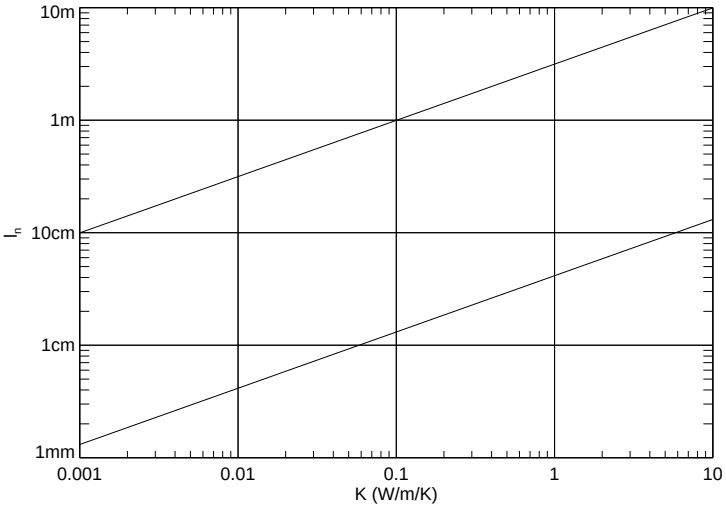


Figure A.2: The dependence of the seasonal temperature penetration depth on the thermal conductivity. The upper line corresponds to the orbital period 3.95 yr, that is appropriate for bodies with the semimajor axis $a = 2.5\,\mathrm{AU}$. The lower one denotes the penetration depth of daily temperature variations ($P = 6\,\mathrm{hr}$). The thermal capacity is assumed $800\,\mathrm{J/kg/K}$ and the density $2500\,\mathrm{kg/m^3}$.

$$-K\frac{\partial T(t,0)}{\partial z} + \epsilon\sigma T^4(t,0) = (1-A)\mathcal{E}(t)\,. \tag{A.11}$$

Here $\sigma = 5.6697 \times 10^{-8}\mathrm{JK}^{-4}$ is the Stephan–Boltzmann constant, $\epsilon$ the infrared emisivity, $A$ the Bond albedo and $\mathcal{E}(t)$ the insolation of the surface element. The first term on the left hand side represents the energy conducted into core, the second term (which is usually linearized in analytical theories) is the energy thermally radiated into space and the right hand side term describes the absorbed solar energy. The second boundary condition corresponds to the assumption of the isothermal core of the asteroid

$$\lim_{z\to\infty}\frac{\partial T(t,z)}{\partial z} = 0\,. \tag{A.12}$$

We also use the periodic initial condition arising from the assumption that the body is thermally relaxed:

$$T(t,z) = T(t+P,z), \tag{A.13}$$

where $P$ is usually the orbital period.

## A.3 Linearized analytical solutions

### A.3.1 Infinite regolith depth

In this section we shall assume the case of material parameters $K$, $c$, $\rho$ which depend neither on depth nor temperature. Then the heat diffusion Equation (A.10) reads

$$\rho c\frac{\partial T}{\partial t} = K\frac{\partial^2 T}{\partial z^2}. \tag{A.14}$$

We introduce new variables according to [Vokrouhlický, 1998a], which are appropriate for solving this equation. Instead of time $t$ we use $\zeta = \exp(int)$, where $n$ is a mean motion, and the depth is replaced by $x = z/\ell$. Next we assume the temperature can be split into constant and variable component and we express it in terms of mean temperature $T_\star$ as $T = T_\star(1 + \delta T')$. The mean temperature $T_\star$ follows from the balance between the emmited and the absorbed energy,

$$\epsilon\sigma T_\star^4 = (1 - A)\mathcal{E}_\star,$$

where $\mathcal{E}_\star = \langle \mathcal{E}(t) \rangle$ is the mean value of the insolation at the given surface element. With these variables, the heat diffusion equation (A.14) has a form

$$i\zeta \frac{\partial}{\partial \zeta} \delta T'(\zeta, x) = \frac{\partial^2}{\partial x^2} \delta T'(\zeta, x). \tag{A.15}$$

If $\delta T' \ll 1$ then $T^4 = T_\star^4(1+4\delta T' + \mathcal{O}(\delta T'^2))$ and we can linearize the surface boundary condition (A.11), which now reads:

$$-\theta \frac{\partial}{\partial x} \delta T' + 4\delta T' + 1 = \mathcal{E}', \tag{A.16}$$

where $\mathcal{E}' = \mathcal{E}/\mathcal{E}_\star$ and

$$\theta = \frac{\sqrt{\rho c K n}}{\epsilon\sigma T_\star^3}. \tag{A.17}$$

Note, that $\theta$ is the only dimensional-less quantity left in the heat diffusion problem; it is often called *the thermal parameter* (e.g. [Spencer et al., 1989]). The boundary condition (A.12) in the core of an asteroid reads

$$\lim_{x \to \infty} \frac{\partial}{\partial x} \delta T' = 0 \, . \tag{A.18}$$

If the insolation term can be written as a sum of Fourier coefficients

$$\mathcal{E}' = \sum_{k=-\infty}^{+\infty} f_k \zeta^k, \tag{A.19}$$

and consequently the temperature variations will have simillar form

$$\delta T'(\zeta, x) = \sum_{k=-\infty}^{+\infty} a_k(x) \zeta^k. \tag{A.20}$$

Substitution these expressions to (A.15) and comparison of terms with the same power of $\zeta$ leads to a set of second order linear differential equations

$$\frac{d^2}{dx^2} a_k(x) - ika_k(x) = 0, \tag{A.21}$$

which has general solution

$$a_k(x) = A_k \exp(\sqrt{ik}x) + B_k \exp(-\sqrt{ik}x).$$

Since $\sqrt{\pm i\,|k|} = \sqrt{|k|/2}\,(i \pm 1)$, we have

$$\begin{aligned} a_0 &= A_0 + B_0 x \\ a_{k>0}(x) &= A'_k \exp\left(\sqrt{|k|/2}\,(i+1)\,x\right) + B'_k \exp\left(-\sqrt{|k|/2}\,(i+1)\,x\right), \\ a_{k<0}(x) &= A'_k \exp\left(\sqrt{|k|/2}\,(i-1)\,x\right) + B'_k \exp\left(-\sqrt{|k|/2}\,(i-1)\,x\right). \end{aligned}$$

The cases with $k \neq 0$ can be collected into a single expression

$$a_{k\neq 0}(x) = A_k \exp(-\psi_k x) + B_k \exp(\psi_k x), \tag{A.22}$$

where

$$\psi_k = \sqrt{|k|/2}\,(1 + i \operatorname{sgn} k). \tag{A.23}$$

The $B_k$ coefficients must be zero due to the constant temperature in the large depth (A.18). The $A_k$ coefficients can be expressed by the substitution (A.22) and (A.20) into to surface boundary condition (A.16):

$$-\theta \sum_{k=-\infty}^{+\infty} A_k\,\psi_k\,\exp(-\psi_k x)\,\zeta^k + 4 \sum_{k=-\infty}^{+\infty} A_k\,\exp(-\psi_k x)\,\zeta^k + 1 = \sum_{k=-\infty}^{+\infty} f_k\,\zeta^k.$$

Comparison of the terms with the same power of $\zeta$ leads to

$$A_k = \frac{f_k}{4 + \theta\,\psi_k}$$

for $k \neq 0$. Since $A_0 = (f_0 - 1)/4$ and $f_0 = 1$ the coefficient $A_0 = 0$. Finally, we have

$$T(t,z) = T_\star \left(1 + \sum_{k=-\infty}^{+\infty} \frac{f_k}{4 + \theta\,\psi_k} \exp(-\psi_k \frac{z}{\ell} + ikn t)\right). \tag{A.24}$$

Since $\mathcal{E}'$ is a periodic real function then $f_k = f_{-k}$ for $k = 2l$ and $f_k = -f_{-k}$ for $k = 2l+1$. Moreover $f_{2l}$ is a real number, while $f_{2l+1}$ is an imaginary number. After a little algebra we end up with the expression for the temperature:

$$\begin{aligned} T = \quad T_\star \Bigg[ & 1 + \frac{1}{2} \sum_{k=2,4,\ldots}^{\infty} f_k\,\exp\left(-\sqrt{\frac{k}{2}}\,x\right)\,[(1+\lambda_k)\cos\phi_k + \lambda_k \sin\phi_k] \\ & + \frac{1}{2} \sum_{k=1,3,\ldots}^{\infty} i\,f_k\,\exp\left(-\sqrt{\frac{k}{2}}\,x\right)\,[\lambda_k \cos\phi_k - (1+\lambda_k)\sin\phi_k] \Bigg], \end{aligned} \tag{A.25}$$

where $\lambda_k = \theta\sqrt{k/32}$ and $\phi_k = -\sqrt{k/2}\,x + knt$. From this expression we can conclude, that the amplitude of the temperature variations decreases with increasing depth below the surface as $\mathrm{e}^{-\sqrt{k/2}x}$. There is also a thermal lag (given by the combination of trigonometric functions in (A.25)).

### A.3.2 Finite regolith depth

Here we assume a more general model for a body which surface is covered by a regolith layer of depth $h$, with the density $\rho_1$, thermal capacity $c_1$ and thermal conductivity $K_1$, while the core has the material parameters $\rho_2$, $c_2$, $K_2$. We also assume these constants do not depend on temperature. (A similar model for a spherical body was derived by [Vokrouhlický and Brož , 1999].) Similarly as in the previous section we introduce new variables. In the regolith layer $x_1 = z/\ell_1$, $\ell_1 = \sqrt{K_1/(\rho_1\, c_1 n)}$ and temperature $T_1 = T_\star(1+\delta T_1')$, in the core $x_2 = z/\ell_2$, $\ell_2 = \sqrt{K_2/(\rho_2\, c_2 n)}$ and $T_2 = T_\star(1 + \delta T_2')$. Then the heat diffusion Equation (A.14) has a form

$$i\zeta \frac{\partial}{\partial \zeta}\delta T_1'(\zeta, x_1) = \frac{\partial^2}{\partial x_1^2}\delta T_1'(\zeta, x_1) \tag{A.26}$$

in the regolith layer and

$$i\zeta \frac{\partial}{\partial \zeta}\delta T_2'(\zeta, x_2) = \frac{\partial^2}{\partial x_2^2}\delta T_2'(\zeta, x_2) \tag{A.27}$$

in the core. The surface boundary condition is similar to (A.16)

$$-\theta \frac{\partial}{\partial x_1}\delta T_1' + 4\delta T_1' + 1 = \mathcal{E}', \tag{A.28}$$

as well as the requirement of the constant temperature in large depth, corresponding to (A.18)

$$\lim_{x_2 \to \infty} \frac{\partial}{\partial x_2}\delta T_2' = 0\ . \tag{A.29}$$

Compared to the case of homogeneous material, discussed in the previous section, here we have two additional conditions on the regolith-core boundary. The first stems from the assumption of the temperature continuity[5]

$$\lim_{x_1 \to h_1^-} \delta T_1' = \lim_{x_2 \to h_2^+} \delta T_2', \tag{A.30}$$

and the second one corresponds to the thermal flux continuity

$$\lim_{x_1 \to h_1^-} \theta_1 \frac{\partial}{\partial x_1}\delta T_1' = \lim_{x_2 \to h_2^+} \theta_2 \frac{\partial}{\partial x_2}\delta T_2'. \tag{A.31}$$

Here $h_1 = h/\ell_1$ and $h_2 = h/\ell_2$. Using the same technique as in the case of homogeneous material, we obtain the temperature in the regolith layer as

$$\delta T_1'(\zeta, x_1) = \sum_{k=-\infty}^{+\infty} a_k(x_1)\zeta^k, \tag{A.32}$$

where

[5]Note that $x_1 \to h_1^-$ means that $x_1$ approaches $h_1$ from lower values of $x_1$ and $x_1 \to h_1^+$ means that $x_1$ approaches $h_1$ from higher values of $x_1$.

$$a_{k\neq 0}(x_1) = A_k \exp(-\psi_k x_1) + B_k \exp(\psi_k x_1) \tag{A.33}$$

and $a_0 = A_0 + B_0\, x_1$. Let us recall that $\psi_k$ is defined by Equation (A.23). Temperature in the core is

$$\delta T_2'(\zeta, x_2) = \sum_{k=-\infty}^{+\infty} b_k(x_2)\zeta^k, \tag{A.34}$$

where

$$b_{k\neq 0}(x_b) = C_k \exp(-\psi_k x_2) + D_k \exp(\psi_k x_2) \tag{A.35}$$

and $b_0 = C_0 + D_0\, x_2$. The four boundary conditions mentioned above can be used to express the coefficients $A_k$, $B_k$, $C_k$ and $D_k$. The assumption of constant temperature in the large depth (A.29) can be satisfied only if $D_k = 0$ (but note that $B_k \neq 0$). At first, we discuss coefficients with $k \neq 0$. The energy balance on the surface (A.28) leads to

$$(\theta_1\psi_k + 4)A_k - (\theta_1\psi_k - 4)B_k = f_k. \tag{A.36}$$

The temperature continuity on the regolith-core boundary (A.30) reads

$$\exp(-\psi_k h_1)\, A_k + \exp(\psi_k h_1)\, B_k - \exp(-\psi_k h_2)\, C_k = 0, \tag{A.37}$$

and the thermal flux continuity on the same boundary (A.31) reads

$$-\exp(-\psi_k h_1)\, A_k + \exp(\psi_k h_1)\, B_k + \frac{\theta_2}{\theta_1}\exp(-\psi_k h_2)\, C_k = 0. \tag{A.38}$$

Putting these results together we obtain

$$A_k = \frac{f_k}{\Xi_k}\left(\frac{\theta_2}{\theta_1} + 1\right), \tag{A.39}$$

$$B_k = -\frac{f_k}{\Xi_k}\left(\frac{\theta_2}{\theta_1} - 1\right)\exp(-2\psi_k h_1), \tag{A.40}$$

$$C_k = 2\,\frac{f_k}{\Xi_k}\,\frac{\theta_2}{\theta_1}\,\exp\left[\psi_k(h_2 - h_1)\right], \tag{A.41}$$

where

$$\begin{aligned}\Xi_k = {} & \frac{\theta_2}{\theta_1}\left[\theta_1\psi_k\left(1 + e^{-2\psi_k h_1}\right) + 4\left(1 - e^{-2\psi_k h_1}\right)\right] \\ & + \left[\theta_1\psi_k\left(1 - e^{-2\psi_k h_1}\right) + 4\left(1 + e^{-2\psi_k h_1}\right)\right].\end{aligned} \tag{A.42}$$

For $k = 0$, the conditions (A.28), (A.30) and (A.31) lead to

$$-\theta_1 B_0 + 4A_0 + 4B_0 + 1 = f_0,$$

$$A_0 + B_0 h_1 = C_0 + D_0 h_2,$$

$$\theta_1 B_0 = \theta_2 D_0 = 0,$$

and consequently

$$A_0 = B_0 = C_0 = D_0 = 0.$$

Finally, in the regolith layer ($z < h$) we have

$$T = T_\star \left\{ 1 + \sum_k \frac{f_k \exp(iknt)}{\Xi_k} \left[ \left( \frac{\theta_2}{\theta_1} + 1 \right) \exp(-\psi_k x_1) - \left( \frac{\theta_2}{\theta_1} - 1 \right) \exp(\psi_k x_1 - 2\psi_k h_1) \right] \right\}, \tag{A.43}$$

and in the core ($z > h$)

$$T = T_\star \left\{ 1 + 2\frac{\theta_2}{\theta_1} \sum_k \frac{f_k}{\Xi_k} \exp[\psi_k (h_2 - h_1 - x_2) + iknt] \right\}. \tag{A.44}$$

All the sumations are made from $k = -\infty$ to $k = \infty$, without $k = 0$.

We can see, that these expressions for temperature inside a two-layered body approach the expression (A.24), describing the temperature in a homogeneous body. In particular, (A.43) approaches (A.24) when $h \to \infty$, (A.43) approaches (A.24) when $h \to 0$ and both (A.43) and (A.44) approach (A.24) when $c_1 \to c_2$ and $K_1 \to K_2$ and $\rho_1 \to \rho_2$.

## A.4 A numerical method for constant material parameters

The linear analytical theories are valid when the temperature variations are relatively small; for larger variations the linearization fails. Moreover, present analytical theories are derived on the basis of several simplifications (e.g., the temperature independence of thermal parameters). In this section we shall derive a numerical model that uses non-linearized boundary condition. This model can be used even for cases with large temperature variations.

If the depth $z$ is scaled by $\ell_n$ and time by orbital period $P$, then the heat diffusion equation (A.14) has a form

$$\frac{\partial T}{\partial t} = \frac{\partial^2 T}{\partial x^2}, \tag{A.45}$$

where $t \in (0,\ 1)$ and $x = z/\ell_n$. The energy conservation law on the surface (A.11) reads

$$-\theta \frac{\partial T(t,0)}{\partial x} + \epsilon\sigma T^4(0,t) = (1 - A)\mathcal{E}(t) \tag{A.46}$$

and the lower boundary condition (A.12)

$$\lim_{x\to\infty} \frac{\partial T(t,x)}{\partial x} = 0. \tag{A.47}$$

Derivatives must be expressed in terms of finite differences. We suppose constant time step $\Delta t = 1/L$, where $L$ is the number of time intervals. Time will be denoted by an upper index $l = 1 \ldots L$. Since analytical theory predicts exponential decrease of amplitude of temperature variations, we chose exponentially spatial step exponentially increasing with depth (like [Hamilton and Matson, 1987]) as $\Delta x_j = x_{j+1} - x_j = \Delta x_0 \exp(\alpha j)$ with $j = 0 \ldots h_{max} - 1$. Lower index will denotes spatial coordinate. Then partial derivatives of the temperature according to time or depth are

$$\left(\frac{\partial T}{\partial t}\right)_j^l = \frac{T_j^{l+1} - T_j^l}{\Delta t}, \qquad \left(\frac{\partial T}{\partial x}\right)_j^l = \frac{T_{j+1}^l - T_j^l}{\Delta x_j}, \tag{A.48}$$

$$\frac{\partial^2 T}{\partial x^2} = \frac{1}{\Delta x_j}\left[\left(\frac{\partial T}{\partial x}\right)_j^l - \left(\frac{\partial T}{\partial x}\right)_{j-1}^l\right] = \frac{1}{\Delta x_j}\left[\frac{T_{j+1}^l - T_j^l}{\Delta x_j} - \frac{T_j^l - T_{j-1}^l}{\Delta x_{j-1}}\right]. \tag{A.49}$$

Using these expressions, the HDE (A.45) reads

$$T_j^{l+1} = T_j^l + \frac{\Delta t}{\Delta x_j}\left(\frac{T_{j+1}^l - T_j^l}{\Delta x_j} - \frac{T_j^l - T_{j-1}^l}{\Delta x_{j-1}}\right), \tag{A.50}$$

which represents an explicit formula for the temperature at time $l$. Here $j = 1 \ldots J-1$ and $l = 1 \ldots L$. Selection of the time step and initial spatial step is restricted by von Newmann stability criterion[6]

$$\Delta t/(\Delta x_0)^2 < 1/2.$$

The surface boundary condition (A.46) in terms of finite differencies is

$$\left(T_0^l\right)^4 + \frac{\sqrt{\rho c K n}}{\sigma\epsilon}\frac{1}{\Delta x_0}T_0^l - \left(\frac{1-A}{\sigma\epsilon}\mathcal{E}^l + \frac{\sqrt{\rho c K n}}{\sigma\epsilon}\frac{1}{\Delta x_0}T_1^l\right) = 0. \tag{A.51}$$

This equation needs to be solved numerically, for instance by the method of Laguerre (e.g. [Press et al., 1992], online version `http://www.nrbook.com/a/bookfpdf.php`). Finally, lower boundary condition reads

$$T_N^l = T_{N-1}^l. \tag{A.52}$$

These equations together with some suitable initial temperature allow to determine the temperature in any time $t^l$ and any depth $x_j$.

Now we will briefly describe the algorithm how to compute the surface temperature of a single facet of an asteroid.

1. Determine the insolation function $\mathcal{E}$ of the given facet. This is discussed in (Appendix B).
2. Chose the initial temperature so that $T_j^0 = \sqrt[4]{(1-A)\langle\mathcal{E}\rangle/(\epsilon\sigma)}$.
3. Chose the appropriate time step $\Delta t$ and the spatial step $\Delta x$ in order the von Neumann criterion of stability is satisfied: $\Delta x_0 = 2\sqrt{\Delta t}$
4. Find the temperatures $T_j^l$ using Equations (A.50), (A.51) and (A.52) for $j = 0, \ldots, J$, $l = 1, \ldots, L$, i.e., during the whole orbital period.
5. The second choice of the initial temperature $T_j^0$ is done by averaging of the surface temperature $T_0^l$ over the whole orbit (i.e., for $l = 1, \ldots, L$): $T_j^0 = \langle T_0^l\rangle$. The temperature is computed again according to 4.

[6] Since $\Delta x_i > \Delta x_0$ for $i > 0$, then von Neumann stability criterion is fulfilled in all depths.

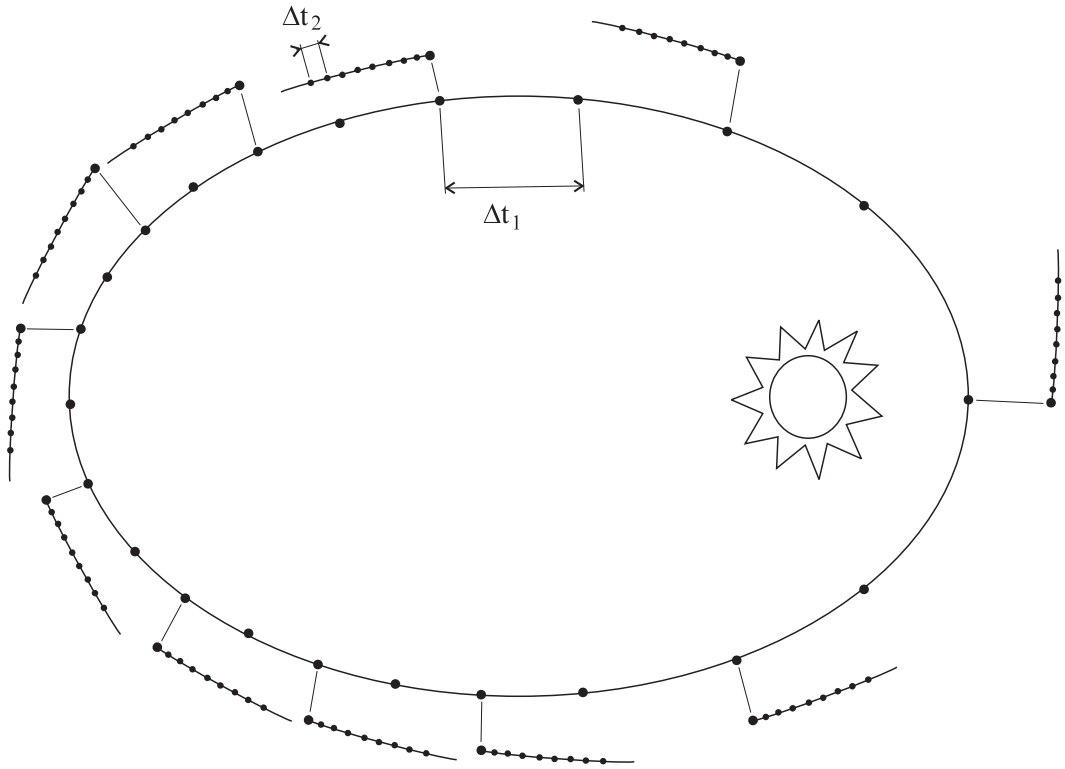


Figure A.3: A "two-level scheme": In the first level we solve the HDE with a longer timestep $\Delta t_1$ along the orbit and save the temperature profiles. In the second level we choose an appropriate amount of time instants and solve the HDE with a shorter timestep $\Delta t_2$ for several tens of rotational periods. Here we use initial temperature profile determined in the first level.

6. The third and following choices of initial temperature are done by $T_j^0 = T_j^L$ and new temperature is again computed according to 4. This is repeated until the required relaxation of temperature is reached.

The time step $\Delta t$ must be chosen small enough, in order the time delay between the maximal temperature and the "noon" is sufficiently covered.

A problem arises, when the rotational period is small compared to the orbital period. In this case, the necessary number of time steps is so high, that the requirements on computer's memory and computational time are unacceptable. We begin with a longer timestep and save the temperature (their depth profiles) in an appropriate amount of time instants (usually 100). Than we integrate temperature during several tens of rotational periods after these time instants and we use the saved temperatures as the initial ones. The integration with the rough timestep gives a sufficient determination of the sesonal temperature profile, whereas the integration with the fine time step gives a precise diurnal temperature variations. We call this technique a "two–level scheme", whereas the former a "one–level scheme". See Figure A.3.

## A.5 Numerical method for non-constant material perameters

In this section we will deal with the case, when material parameters depend both on depth and temperature. The dependance on depth follows namely from a possible existence of surface regolith layer, which has several orders of magnitude lower thermal conductivity than a fresh rock beneath.

### A.5.1 Modification of the Crank-Nicholson scheme

We can not use the explicit numerical scheme (A.50) here, because it would be very difficult to fulfill the von Neumann stability criterion due to thermal dependence of material parameters. So, we have to modify implicit Crank-Nicholson method which is unconditionally stable and moreover it is of second order in $\Delta t$. The one-dimensional heat diffusion Equation (A.10) for non-constant material parameters is

$$\rho\, c\, \frac{\partial T}{\partial t} = \frac{\partial K}{\partial z}\frac{\partial T}{\partial z} + K\frac{\partial^2 T}{\partial z^2}.$$

Expressing the partial derivatives in the terms of finite differencies, we obtain

$$T_j^{l+1} - T_j^l = \frac{\Delta t}{\Delta x_j \rho_j^l c_j^l}\left[\frac{K_{j+1}^l}{\Delta x_j}T_{j+1}^l - \left(\frac{K_{j+1}^l}{\Delta x_j} + \frac{K_j^l}{\Delta x_{j-1}}\right)T_j^l + \frac{K_j^l}{\Delta x_{j-1}}T_{j-1}^l\right], \tag{A.53}$$

which allows to solve the HDE explicitely with non-constant material parameters. If the partial derivatives with respect the time are expressed in the time $n+1$, instead of $n$, then we obtain purely implicit scheme:

$$T_j^{l+1} - T_j^l = \frac{\Delta t}{\Delta x_j \rho_j^{l+1} c_j^{l+1}}\left[\frac{K_{j+1}^{l+1}}{\Delta x_j}T_{j+1}^{l+1} - \left(\frac{K_{j+1}^{l+1}}{\Delta x_j} + \frac{K_j^{l+1}}{\Delta x_{j-1}}\right)T_j^{l+1} + \frac{K_j^{l+1}}{\Delta x_{j-1}}T_{j-1}^{l+1}\right]. \tag{A.54}$$

The sum of (A.53) and (A.54) gives

$$\begin{aligned} &T_{j+1}^{l+1}[b_j^{l+1}a_j^{l+1}] + T_j^{l+1}[-2 - a_j^{l+1}(b_j^{l+1} + b_{j-1}^{l+1})] + T_{j-1}^{l+1}[a_j^{l+1}b_{j-1}^{l+1}] = \\ &= -2T_j^l - a_j^l[b_j^l T_{j+1}^l - (b_j^l + b_{j-1}^l)T_j^l + b_{j-1}^l T_{j-1}^l], \end{aligned} \tag{A.55}$$

where

$$a_j^l = \frac{\Delta t}{\Delta x_j \rho_j^l c_j^l}, \qquad b_j^l = \frac{K_{j+1}^l}{\Delta x_j}$$

for $j = 0 \ldots J-1$. This, together with the lower boundary condition (bottom row), can be expressed in the matrix notation

$$\mathbb{D}\,\mathbf{T}^{l+1} = \mathbf{R},$$

or

$$\begin{pmatrix} B_1^{l+1} & C_1^{l+1} & & & & \\ A_2^{l+1} & B_2^{l+1} & C_2^{l+1} & & & \\ & A_3^{l+1} & B_3^{l+1} & C_3^{l+1} & & \\ & & \cdots & \cdots & \cdots & \\ & & & A_{J-1}^{l+1} & B_{J-1}^{l+1} & C_{J-1}^{l+1} \\ & & & & 1 & -1 \end{pmatrix} \begin{pmatrix} T_1^{l+1} \\ T_2^{l+1} \\ T_3^{l+1} \\ \cdots \\ T_{J-1}^{l+1} \\ T_J^{l+1} \end{pmatrix} = \begin{pmatrix} R_1^l - A_1^{l+1}T_0^{l+1} \\ R_2^l \\ R_3^l \\ \cdots \\ R_{J-1}^l \\ 0 \end{pmatrix}, \tag{A.56}$$

where

$$\begin{aligned} &A_j^l = a_j^l b_{j-1}^l, \quad B_j^l = -2 - a_j^l b_j^l - a_j^l b_{j-1}^l, \quad C_j^l = a_j^l b_j^l, \\ &R_j^l = -C_j^l T_{j+1}^l + (-4 - B_j^l)T_j^l - A_j^l T_{j-1}^l \end{aligned}$$

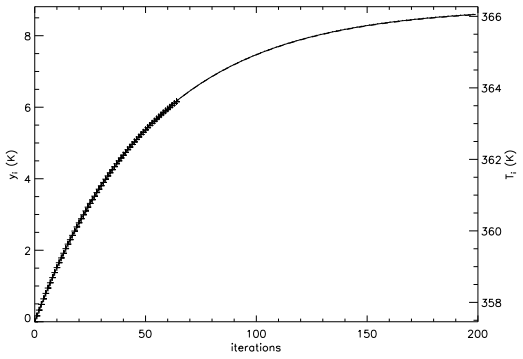


Figure A.4: A typical example of slow convergence of surface temperature. The cross symbols denote iterated temperatures (65 iterations), the solid curve is temperature computed analytically from the first four iterations. The limit temperature $T_\infty$ is represented by the top margin of the $y-$axis. It can be seen, that more than 200 iterations would be necessary for good relaxation of the right value. Here, the analytical estimation of $T_\infty$ is needed.

for $j = 1 \ldots J-1$. ($A_J^l = 1$, $B_J^l = -1$.) The temperature in the time $l+1$ can be expressed from the equation system (A.56) and the surface boundary condition:

$$(T_0^{l+1})^4 + \frac{K_0^{l+1}}{\epsilon\sigma\Delta x_0} T_0^{l+1} - \frac{1}{\epsilon\sigma}\left[(1-A)\mathcal{E}^{n+1} + \frac{K_0^{l+1}}{\Delta x_0} T_1^{l+1}\right] = 0. \tag{A.57}$$

System (A.56) represents a modified Crank-Nicholson scheme, which is unconditionally stable and thus there are no restrictions on spatial or time step from the stability point of view.

### A.5.2 Improvement of the convergence

The main trouble is that the matrix $\mathbb{D}$ as well as the right hand side $\mathbf{R}$ depends non-linearly on the unknown temperature $\mathbf{T}^{l+1}$. (Matrix $\mathbb{D}$ is expressed in the time $l+1$ and contains coefficients $A_i^{l+1}$, $B_i^{l+1}$ and $C_i^{l+1}$ which are functions of the temperature dependent material parameters $K$ and $c$. The same situation is in the case of right hand side $\mathbf{R}$.) This problem can be solved iteratively so that initially we determine $\mathbb{D}$ and $\mathbf{R}$ using $\mathbf{T}^l$ instead of $\mathbf{T}^{l+1}$. Then we obtain the first iteration $\mathbf{T}^{l+1}|_0$ and use it again instead of $\mathbf{T}^{l+1}$. This would be repeated until a difference between $i$-th and $(i+1)$-th iteration will be smaller than a given precision. However, our experience shows that sometimes a huge number of iterations is necessary to reach a right value of $\mathbf{T}^{l+1}$. Thus we had to develop a technique which accelerates the convergence of $\mathbf{T}^{l+1}$, and we describe it below.

Let $T_i$ denotes the $i$-th iteration of the temperature $\mathbf{T}^{l+1}$. We expect that iterations exponentially approach a limit $T_\infty$ which means that $T_\infty - T_i = y_\infty a^{-i}$. We shall try to estimate this limit from the first few iterations. (See Figure A.4.)

A difference between the zeroth and $i$-th iteration is $y_i = T_i - T_0$. Then $y_i = y_\infty(1-a^{-i})$ and $y_j = y_\infty(1-a^{-j})$. After some algebra we obtain $y_i - y_j = y_i a^{-j} - y_j a^{-i}$. Assuming $j = ki$ and substituting $t = a^{-i}$ we have

$$y_i t^k - y_j t + (y_j - y_i) = 0.$$

For $k = 2$ the solution is

$$t_{1,2} = \frac{y_j \pm |y_j - 2y_i|}{y_i},$$

which leads to the single value[7] $t = (y_j - y_i)/y_i$. This means that[8] $a = \left(\frac{y_i}{y_j - y_i}\right)^{\frac{1}{i}}$ and $y_\infty = \frac{y_i^2}{2y_i - y_j}$, or by means of the temperature iterations

$$a = \left(\frac{T_i - T_0}{T_{2i} - T_i}\right)^{\frac{1}{i}}, \qquad y_\infty = \frac{(T_i - T_0)^2}{2T_i + T_0 - T_{2i}}.$$

The limit temperature is then

$$T_\infty = T_0 + \frac{(T_i - T_0)^2}{2T_i + T_0 - T_{2i}}. \tag{A.58}$$

If $i = 2$, the limit temperature can be determined from four iterations as

$$T_\infty = T_0 + \frac{(T_2 - T_0)^2}{2T_2 + T_0 - T_4}.$$

Here, a special care must be taken if the denominator is zero or nearly zero. This indicates, that temperature iterations converge too slowly and due to small differences between them they seem to change linearly and not exponentially. In this case, we substitue $i = 4$, 8, 16, etc. until the exponential convergence (or large number of iterations) is reached. Finally, we substitute the limit temperature $T_\infty$ into (A.56) and verify it does not differ from $\mathbf{T}^{l+1}$.

Let us to estimate the number of iterations necessary to reach a good approximation of $y_\infty$. Let $p = y_i/y_\infty$. Then $a^{-i} = 1 - p$ and $i = -\ln(1-p)/\ln(a)$. For example, if we want $y_i$ to be 99% of $y_\infty$, we need roughly $-\ln(0.01)/\ln(a)$ iterations.

### A.5.3 The algorithm

Our algorithm for the computation of the surface temperature on a facet of an asteroid is the following:

1. Determine the insolation function $\mathcal{E}(t)$ for the given facet. This is discussed in (B).
2. Chose the initial temperature so that $T_j^0 = \sqrt[4]{(1-A)\langle\mathcal{E}\rangle/(\epsilon\sigma)}$.
3. Chose appropriate initial time step $\Delta t_0$ and spatial steps $\Delta x_i$. (See the example in Section A.6.)
4. Solve the temperature $T_j^l$, during the whole orbital period, by equations (A.56), (A.57) using method described in Section A.5.2.
5. The second choice of initial temperature $T_j^0$ is given by the averaging of the surface temperatures $T_0^l$ over the whole orbit (i.e., for $l = 1, \ldots, L$): $T_j^0 = \langle T_0^l \rangle$, and the temperature is further computed[9] according to 4.
6. The third and following choices of the initial temperature are performed simply by $T_j^0 = T_j^L$ and the temperature is again computed according to 4. The time step can be smaller and smaller in the subsequent turns. This is repeated until a satisfactory relaxation of temperature is reached.

[7] rejecting the solution $t = 2$

[8] The fraction is always positive because if $y_j > y_i$ then $y_i > 0$ and if $y_j < y_i$ then $y_i < 0$

[9] Optionally, with a smaller time step $\Delta t_1$

## A.6 A simple example of temperature behaviour

Here we shall present an example of the temperature behaviour computed by different techniques described before. Let us suppose the situation described in Figure A.5. The body is at a circular orbit, 1 AU from the Sun. We shall focus on surface element $dS$ at the equator. Its insolation $\mathcal{E}(t)$ can be express as

$$\mathcal{E}(t) = \begin{cases} A \sin 2\pi t/P, & t < P/2 \\ 0, & t \geq P/2, \end{cases}$$

with the amplitude $A = 1366\,\mathrm{W/m^2}$ (corresponding to the flux at 1 AU distance from the Sun) and period $P = 6\,\mathrm{hr}$. The along-track component of the thermal force corresponding to the temperature $T$ is

$$f_\tau(t) = \frac{2\epsilon\sigma}{3c} T^4(t) \sin(2\pi t/P).$$

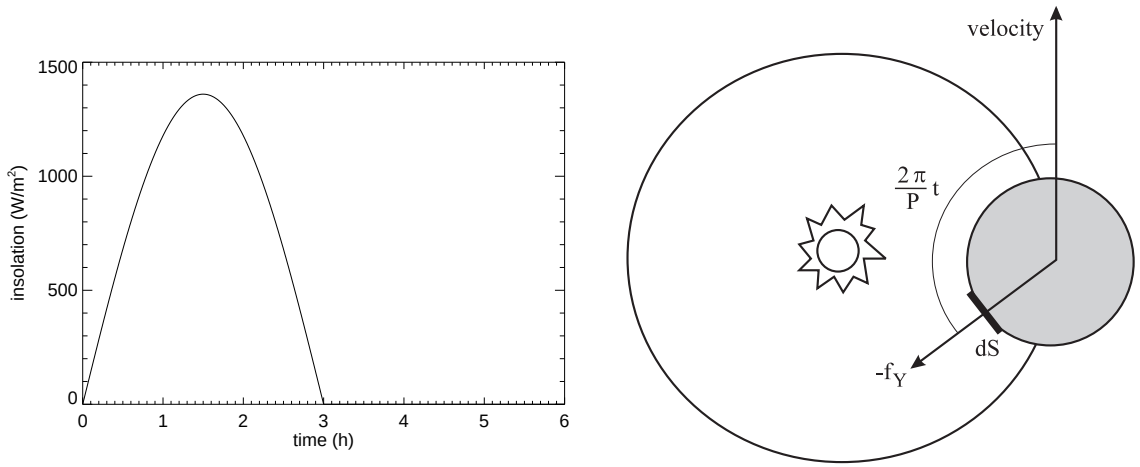


Figure A.5: Left: The insolation as a function of time. An amplitude is $1366\,\mathrm{W/m^2}$. Right: geometry of the problem. More explanation in the text.

In the following figures A.6–A.8 we present the solution of the surface temperature corresponding to the insolation $\mathcal{E}(t)$,depicted in Figure A.5. A detailed discussion can be found in the figure captions of particular figures.

In Figure A.6 we deal with a problem of the right choice of spatial and time steps (for homogeneous body). We found that the results (temperature and the Yarkovsky force) are almost independent on the time step (6 s – 600 s). If the initial spatial step is less than $\Delta x_0 =\sim 0.1\ell_d$, the results do not depend neither on the spatial step.

In A.7 we show the dependence of temperature and the Yarkovsky force on the spatial step and the regolith depth. We found the results are nearly independent on spatial step.

Finally, in Figure A.8, we compare the results (time dependence of the temperature, thermal lag and the Yarkovsky force) of the analytical and numerical model.

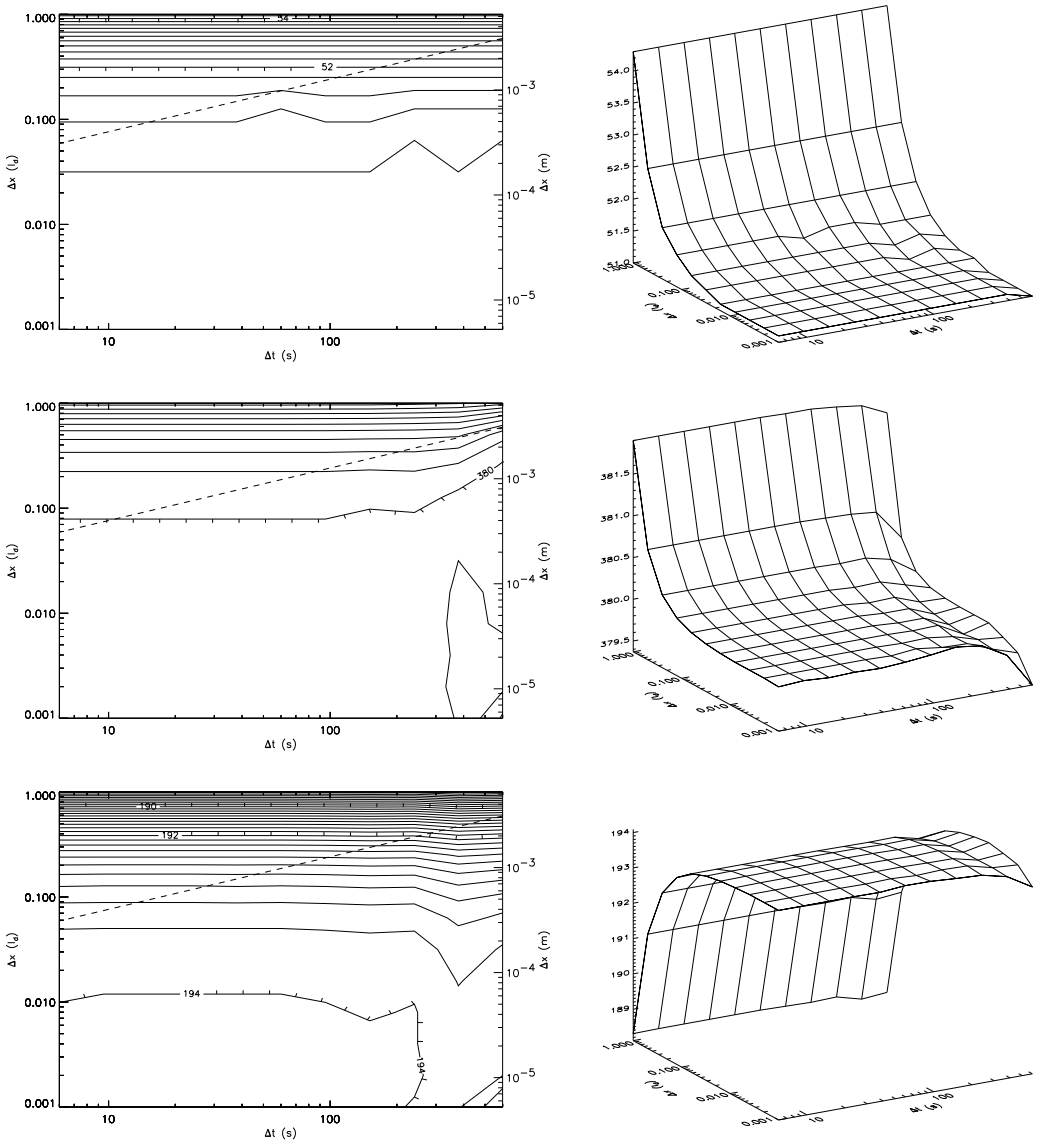


Figure A.6: The dependence of the numerically (modified Crank-Nicolson scheme) computed Yarkovsky force and the surface temperature on chosen initial spatial step $\Delta x_0$ and time step $\Delta t$. The **upper row** represents the resulting spin-averaged along-track component of the thermal force in $10^{-8}$ N/m units. The **middle row** corresponds to the maximal surface temperature and the **lower one** to minimal surface temperature in K. The left column is a countour plot (here, the dashed line divides the figure to upper-left area, where the von-Neumann criterion is fulfilled and lower-right one where it is not fulfilled) while the right one is a surface plot. These results correspond to the insolation from Figure A.5. Here, we assume the thermal parameters to be independent both on temperature and spatial coordinates (but the results with temperature dependent material parameters are quite similar). The thermal conductivity is assumed $K = 0.01\,\mathrm{W/m/K}$, the thermal capacity $c = 735\,\mathrm{J/kg/K}$ and the density $\rho = 1.7\,\mathrm{g/cm^3}$. We can see a near independence on time step in the range from 6 to 600 s. However, the initial spatial step is more important quantity. We found that $\Delta x_0$ should be smaller than $\sim 0.1\,\ell_d$ or $0.01\,\ell_d$. We can also see that the usage of the modified Crank-Nicolson scheme allows us to prevent a very short time step $< 6$ s which should be used in an explicit scheme together with $\Delta x_0 < 0.1\,\ell_d$ (due to von Neuman criterion of stability).

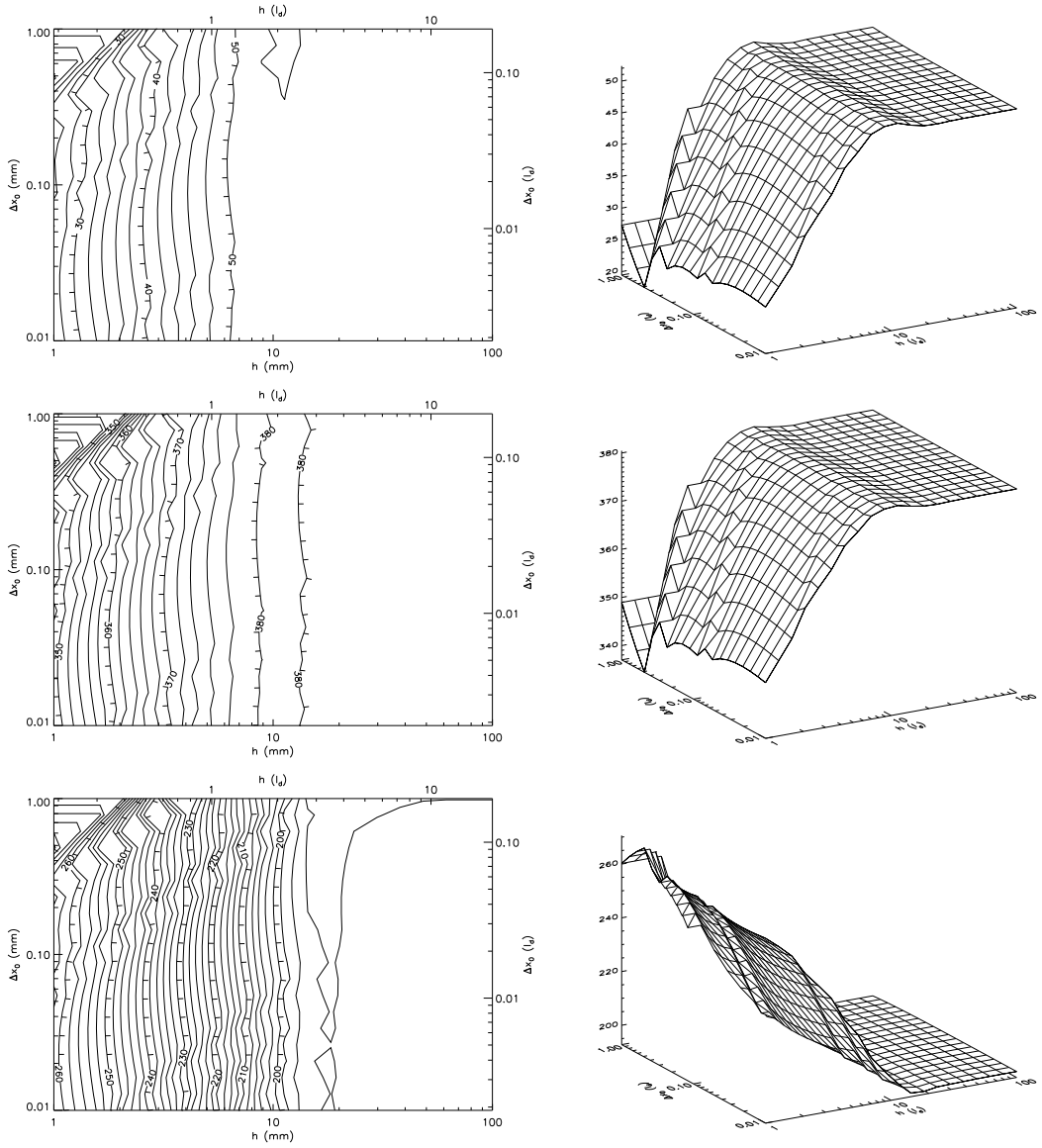


Figure A.7: The Dependence of the numerically computed Yarkovsky force and the surface temperature on the chosen initial spatial step $\Delta x_0$ for various regolith depths. As in Figure A.6, the **upper row** represents the resulting spin-averaged along track component of the thermal force in $10^{-8}\,\mathrm{N/m}$. The **middle row** corresponds to the maximal and the **lower one** to the minimal surface temperature in K. The left column is a countour plot while the right one is a surface plot. These results correspond to the insolation from Figure A.5. Here we assume (unlike in Figure A.6) the thermal parameters dependent both on temperature and space: The regolith layer is characterized by the thermal conductivity $K = 0.01 + 2 \times 10^{-11} (T/\mathrm{K})^3\,\mathrm{W/m/K}$ and the thickness from 1 to 100 mm, while the core has $K = 2.6\,\mathrm{W/m/K}$. The thermal capacity (A.8) and the density $\rho = 1.7\,\mathrm{g/cm^3}$ are the same for regolith and core. The results are again nearly independent on a timestep. The dependence on $\Delta x_0$ is fortunately also weak, though it is better to use $\Delta x_0 < 0.1\,\ell_d$ again.

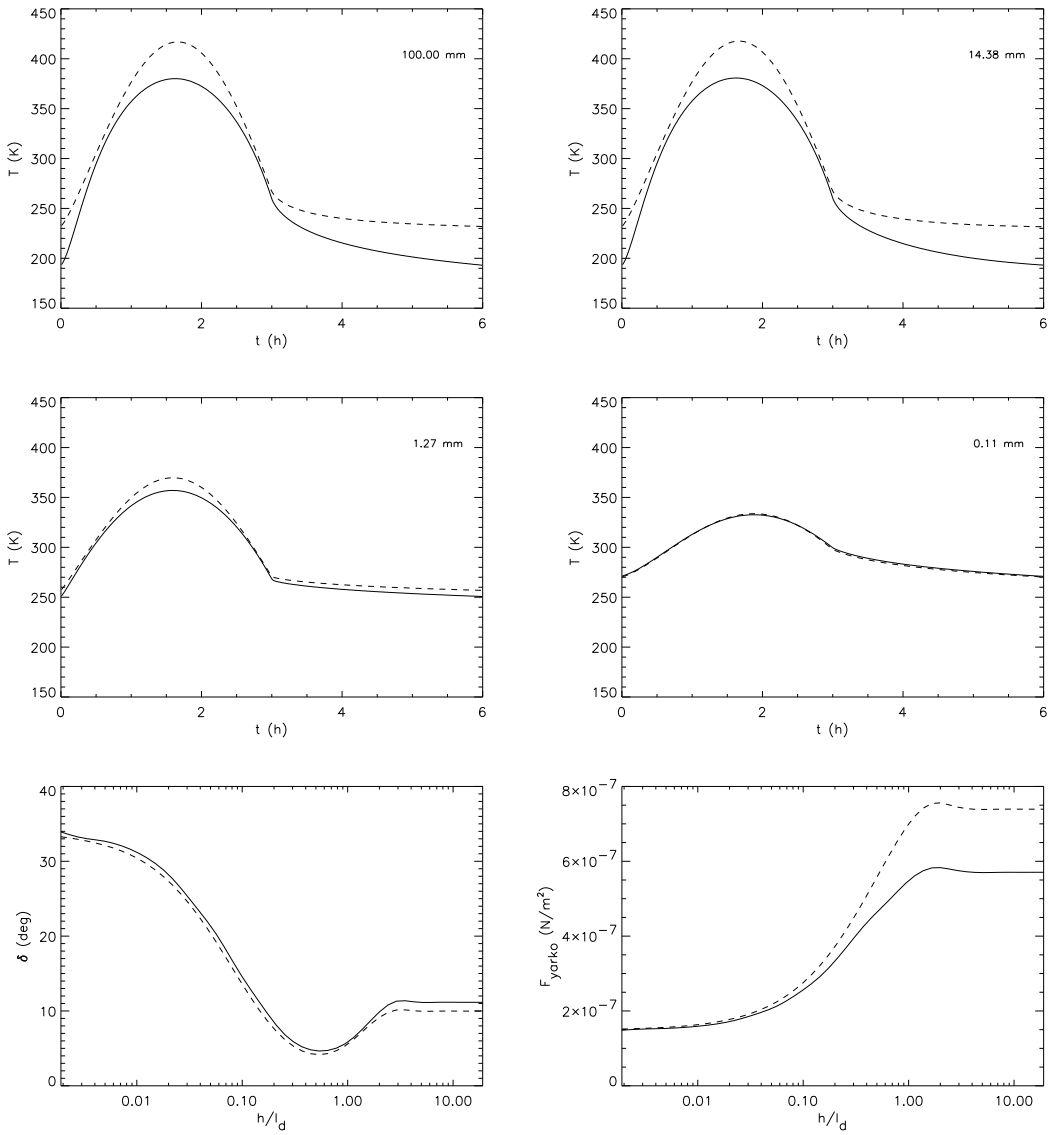


Figure A.8: A comparison of results of the numerical theories (solid curves) and the analytical theories (dashed curves, according to A.43) for various depths for regolith layer. **Upper two rows** show the time dependence of the temperature for regolith thickness denoted in upper right corner of each plot. It can be seen that there is quite well agreement between the numerical and the analytical theory for small regolith depths. In this case the amplitude of the temperature variations are small (due to highly conductive core) and the linearization in analytical theory works well. The **lower left figure** shows the dependence of the angle $\delta$, between the direction opposite to the Sun and the thermal Yarkovsky force. The **lower right figure** shows the dependence of the along-track component of the thermal force on regolith depth. These results again correspond to the insolation from Figure A.5. Here we assume thermal parameters dependent both on the temperature and space: The regolith layer is characterized by the thermal conductivity $K = 0.013\,\mathrm{W/m/K}$ and the thickness from 0.01 to 100 mm, while the core has $K = 1\,\mathrm{W/m/K}$. The thermal capacity $c$ is the same for the core and the regolith layer. It is (A.8) for the numerical method and $750\,\mathrm{J/kg/K}$ for the analytical method. The density of the core and regolith is $\rho = 1.7\,\mathrm{g/cm^3}$.

# Appendix B

# Shape representation

In our work, the shapes of all bodies (both artificial and real) are modeled by polyhedrons with thousands of triangular facets. The bodies are represented by a list of vectors, describing the vertices, and by a list of mutual identification (which of the vectors form a triangle). This representation is able to describe complicated irregular shapes of small solar system bodies, including craters, mountains or valleys on the surface (e.g., [Simonelli et al., 1993]).

For each polyhedron we need to know the volume $V$ (mass), inertia tensor $\mathbf{I}$ (principal moments $A$, $B$, $C$, eigenvectors of $\mathbf{I}$) as well as centers $\mathbf{r}_i$, outer normal $\mathbf{n}_i$ and areas $S_i$ for each surface facet.

Moreover, we need to transform the coordinate system into the one having the origin in the center of mass and with axes corresponding to the eigenvectors of inertia tensor ($x$-axis corresponding to the longest axis of $\mathbf{I}$, $z$-axis to the shorter one).

Here we present a procedure, how to determine these quantities and insolation (including self-shadowing of the surface) of such a body.

Fortunately, any polyhedron (with triangular facets) can be divided into tetrahedrons (surface triangular facet forms the base and some point inside the polyhedron represents vertex). We use the procedure published by [Dobrovolskis, 1996] and generalize it slightly, in order to describe the case of non-convex bodies (with respect to the origin of coordinate system). We call the body as "non-convex with respect to the origin", if there exist such a half-line going from the origin, which intersects the surface in more than one point (see Figure B.1).

## B.1 Basic characteristics of the polyhedron and its facets

Consider the vertices of tetrahedron, which can be described by four position vectors $\mathbf{E}_i$, $\mathbf{F}_i$, $\mathbf{G}_i$ and $\mathbf{0}$, which coincides with the origin of coordinate system (see Figure B.1 left). The center of the surface triangular facet $i$, defined by the vectors $\mathbf{E}_i$, $\mathbf{F}_i$ and $\mathbf{G}_i$, is

$$\mathbf{t}_i = \frac{1}{3}(\mathbf{F}_i + \mathbf{E}_i + \mathbf{G}_i). \tag{B.1}$$

The center of mass of the tetrahedron is

$$\mathbf{r}_i = \frac{1}{4}(\mathbf{E}_i + \mathbf{F}_i + \mathbf{G}_i). \tag{B.2}$$

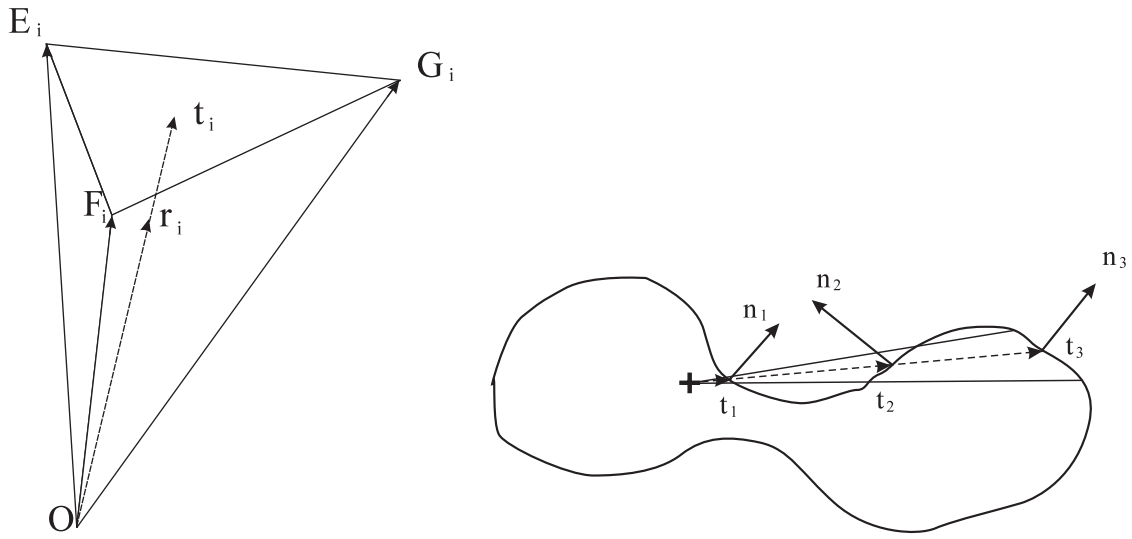


Figure B.1: Left: The tetrahedron with the position vectors $\mathbf{E}_i$, $\mathbf{F}_i$, $\mathbf{G}_i$ of the vertices, vector pointing to the center of surface facet $\mathbf{t}_i$ and the center of mass $\mathbf{r}_i$. Right: a body which is non-convex with respect to the center of mass (denoted by the cross). This plot illustrates how the sign of $\mathbf{n}_i \cdot \mathbf{t}_i$ depends on the number of intersections of $\mathbf{t}_i$ with the surface (if the number is odd, the dot product is negative).

Then we determine the number of intersections[1] of the line $\mathbf{0} - -\mathbf{t}_i$ with the surface. We denote this number as $\nu_i$. In the case of a body convex with respect to the origin, $\nu_i = 0$.

The outer normal to the triangular facet is given by

$$\mathbf{n}_i = \frac{1}{2}(\mathbf{F}_i - \mathbf{E}_i) \times (\mathbf{G}_i - \mathbf{E}_i) \tag{B.3}$$

and $\mathbf{n}_i \cdot \mathbf{t}_i > 0$ must be fulfilled if $\nu_i$ is even while $\mathbf{n}_i \cdot \mathbf{t}_i < 0$ if $\nu_i$ is odd (see Figure B.1 right). The area of the facet can be expressed as $S_i = |\mathbf{n}_i|$ and the whole area of a body is

$$S = \sum_i S_i = \sum_i |\mathbf{n}_i| \tag{B.4}$$

The volume of the tetrahedron is given by

$$V_i = \frac{1}{3}(-1)^{\nu_i} |\mathbf{E}_i \cdot \mathbf{n}_i|. \tag{B.5}$$

Note that for $\nu_i$ odd the volume $V_i$ is negative. The whole volume can be expressed as

$$V = \sum_i V_i, \tag{B.6}$$

[1] In other words, we have to find a number of facets $j \neq i$ which are intersected by the vector $\mathbf{t}_i$. This means we solve the equation

$$\mathbf{E}_j\, a + \mathbf{F}_j\, b + \mathbf{G}_j\, c = \mathbf{t}_i,$$

where the vectors $\mathbf{E}_j$, $\mathbf{F}_j$, $\mathbf{G}_j$ describe the $j-$th facet. If $\min(a, b, c) > 0$, then the vector $\mathbf{t}_i$ intersects the facet $j$.

where the summation is made over all the tetrahedron volumes (both positive and negative). Assuming a uniform density $\rho$, the center of mass of the whole polyhedron is given by

$$\mathbf{r} = \frac{1}{V} \sum_i V_i \, \mathbf{r}_i. \tag{B.7}$$

Finally, the tensor of inertia of the tetrahedron can be expressed in cartesian coordinates as (according to [Dobrovolskis, 1996]):

$$I_{xx} = P_{yy} + P_{zz}, \qquad I_{yz} = -P_{yz} \tag{B.8}$$
$$I_{yy} = P_{zz} + P_{xx}, \qquad I_{xz} = -P_{xz} \tag{B.9}$$
$$I_{zz} = P_{xx} + P_{yy}, \qquad I_{xy} = -P_{xy}, \tag{B.10}$$

where

$$P_{jk} = \frac{\rho V}{20}(2E_jE_k + 2F_jF_k + 2G_jG_k + E_jF_k + E_kF_j + E_jG_k + E_kG_j + F_jG_k + F_kG_j). \tag{B.11}$$

Due to simplicity we do not write the index $i$ of the tetrahedron. The inertia tensor of the whole polyhedron is given by

$$\mathbf{I} = \sum_i \mathbf{I}_i. \tag{B.12}$$

After the translation of the coordinate system into the center of mass ($\mathbf{r} = 0$), we can proceed with the determination of the principal moments of inertia $A \leq B \leq C$ and the corresponding eigenvectors according to [Dobrovolskis, 1996].

## B.2 Insolation and shadowing

Next we shall describe a procedure we use to determine the insolation $\mathcal{E}$ (W/m$^2$) of a facet. There are three possible cases:

**Facet pointing away from the Sun.** The facet $i$ is in the shadow and the insolation is zero when the outer normal $\mathbf{n}_i$ and the direction to the Sun $\mathbf{s}$ fulfills the relation

$$\mathbf{s} \cdot \mathbf{n}_i < 0. \tag{B.13}$$

**Sunward facet shadowed by another facet.** The facet $i$ is pointing towards the Sun, if

$$\mathbf{s} \cdot \mathbf{n}_i > 0. \tag{B.14}$$

However, even this sunward facet can be shadowed in case of non-convex shape of polyhedron. We must test every surface facet $j \neq i$ whether it casts shadow on the facet[2] $i$: The facet $i$ is shadowed by another facet $j$ if the ray[3], defined by the center of facet $\mathbf{t}_i$ and the vector $\mathbf{s}$, lies inside a tetrahedron defined by vertices $\mathbf{r}_i$, $\mathbf{E}_j - \mathbf{r}_i$, $\mathbf{F}_j - \mathbf{r}_i$ and $\mathbf{G}_j - \mathbf{r}_i$. This means that we solve the set of 3 linear equations

[2] It is necessary for sunward facets only.
[3] This ray can be described as $\mathbf{r}_i + q\mathbf{s}$, where $q$ is positive.

$$(\mathbf{E}_j - \mathbf{r}_i)\, a + (\mathbf{F}_j - \mathbf{r}_i)\, b + (\mathbf{G}_j - \mathbf{r}_i)\, c = \mathbf{s}, \tag{B.15}$$

for three unknowns $a$, $b$, $c$. The facet $i$ is shadowed by the facet $j$ if

$$\min(a, b, c) > 0. \tag{B.16}$$

Again, the insolation of this facet is $\mathcal{E} = 0$.

**Non-shadowed sunward facet.** If the facet $i$ obeys (B.14) and moreover there is no facet $j \neq i$ that obeys (B.15) with (B.16), we can say the facet $i$ is insolated and its insolation is

$$\mathcal{E} = \Phi\, \mathbf{s} \cdot \mathbf{n}_i, \tag{B.17}$$

where $\Phi$ is the solar flux.

This procedure is very CPU time consuming so we had to accelerate it somehow. We describe vector $\mathbf{s}$ by spherical coordinates $\varphi$ and $\vartheta$, conected with body-frame. For any $\varphi = 0 \ldots 360^\circ$ and $\vartheta = +90 \cdots -90$ (with a $1^\circ$ step) we determined all sunward facets which are self-shadowed and stored their indices into a file.

The computation of the insolation of a polyhedron along its orbit about the Sun is made in several steps. At first we determine the position of the Sun $\mathbf{s}$ with respect to the body frame. Then the insolation (B.17) is calculated for sunward facets (B.14). Finally, the insolation of shadowed sunward facets corresponding to the vector $\mathbf{s}$ (described by $\varphi$, $\vartheta$), whose indices has been stored in the file, is set to zero.

# Appendix C

# Gaussian random spheres

Due to a limited number of precisely determined shapes of asteroids we turn our attention to artificially generated shapes by the technique of Muinonen (e.g., [Muinonen, 1996], [Muinonen, 1998], [Muinonen and Lagerros, 1998]). These shapes are called Gaussian random spheres. The radius of such a body in the direction given by spherical angles $\theta$ and $\phi$ may be expressed as

$$r(\theta,\phi) = \frac{a}{\sqrt{1+\sigma^2}} \exp\left[s\left(\theta,\phi\right)\right] \ , \tag{C.1}$$

where $a$ is the scaling factor and $\sigma$ is the variance of $r$. The "logradius" $s(\theta,\phi)$ is given by a spherical harmonic development

$$s(\theta,\phi) = \sum_{\ell=0}^{\infty} \sum_{m=0}^{\ell} P_\ell^m(\cos\theta) \left(a_{\ell m}\cos m\phi + b_{\ell m}\sin m\phi\right) \ . \tag{C.2}$$

Here the coefficients $a_{\ell m}$ and $b_{\ell m}$ are independent Gaussian random variables with zero mean, and variance reading

$$\beta_{\ell m}^2 = (2-\delta_{\ell 0})\,\frac{(\ell-m)!}{(\ell+m)!}\,c_\ell\,\beta^2 \ , \tag{C.3}$$

where $\beta^2 = \ln(1+\sigma^2)$ and $\delta_{\ell 0}$ is the Kronecker symbol. The model then depends on the scaling factor $a$, the variance $\sigma$ of the distribution of surface heights, and a set of parameters $c_\ell$ from Equation (C.3).

[Muinonen and Lagerros, 1998] analysed accurately known shapes of 14 asteroids and they obtained best estimates of the parameters $\sigma$ and $c_\ell$ for their sample of asteroids. These parameters, determined for 7 smallest and 7 largest bodies, slightly differ. The most useful data for our purpose are those for smallest bodies[1]. The standard deviation $\sigma$ of radius is then 0.245 and the coefficients $c_\ell$ are listed in Table C.1.

We used these parameters to generate a set of 1000 Gaussian random spheres. These bodies are scaled to have the same volume as the sphere with radius 10 km. Figure C.1 shows the distribution of the dynamical ellipticity $(C-(A-B)/2)/C$ and triaxiality parameter $A/B$ for the set of 1000 Gaussian random spheres. The quantities $A < B < C$ denote the principal moments of inertia. Diamond symbols in the figure denote the values for several real objects (not used in Muinonen and Lagerros' analysis).

[1] Namely: (4769) Castalia, (4179) Toutatis, (1620) Geographos, (915) Gaspra, Phobos, Deimos, (243) Ida.

| $\ell$ | $c_\ell$ | $\ell$ | $c_\ell$ |
|---|---|---|---|
| 0 | $9.5431 \times 10^{-3}$ | 6 | $6.7379 \times 10^{-3}$ |
| 1 | $2.1972 \times 10^{-1}$ | 7 | $2.6938 \times 10^{-3}$ |
| 2 | $6.2665 \times 10^{-1}$ | 8 | $2.8687 \times 10^{-3}$ |
| 3 | $8.3670 \times 10^{-2}$ | 9 | $5.6931 \times 10^{-4}$ |
| 4 | $3.1648 \times 10^{-2}$ | 10 | $3.9023 \times 10^{-4}$ |
| 5 | $1.5512 \times 10^{-2}$ | | |

Table C.1: The coefficients $c_\ell$ from Equation (C.3). Adapted from table 5, column "Small" in [Muinonen and Lagerros, 1998], computed for seven smallest bodies under study (see the text).

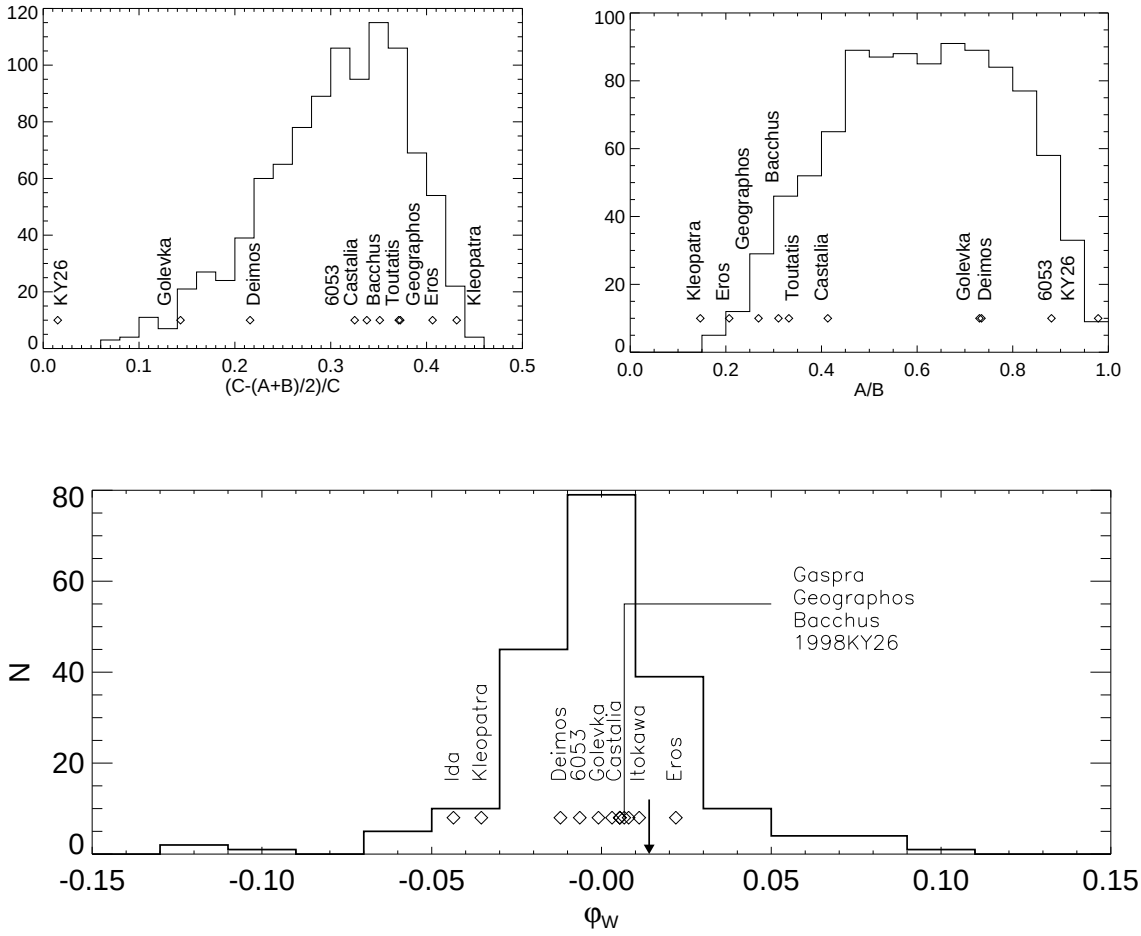


Figure C.1: Shape characteristics for 1000 artificially generated Gaussian random spheres. Upper left (a): Distribution of the dynamical elipticity $(C-(A+B)/2)/C$. Upper right (b): triaxiality parameter $A/B$. Lower figure (c): the windmill factor $\varphi_w$. The arrow denotes the median of absolute values, which is 0.014, and the diamond symbols indicate the values of these parameters calculated for real objects.

Figure C.1c depicts the distribution of the absolute value of windmill factor ($\varphi_w$) defined by Equation 3.11 within the set of 1000 Gaussian random spheres. (The windmill factor corresponds to the strength of YORP effect and depends on the shape of body.) There are also values for several real asteroids in the plot. The median of windmill factor is the value 0.014. The shapes of 200 Gaussian random spheres can be seen in Figures C.2 - C.7.

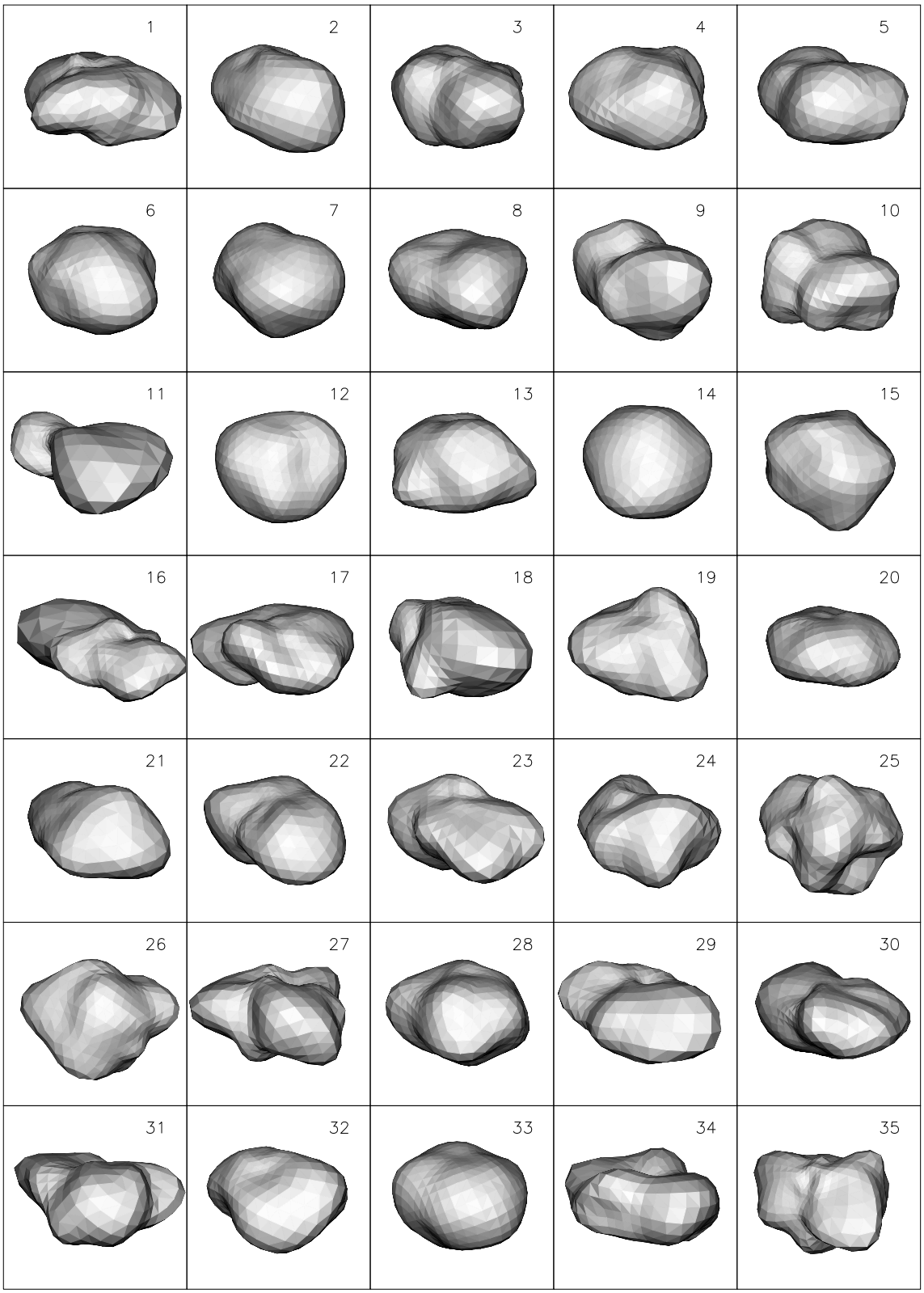


Figure C.2: Gaussian random spheres no. 1 ... 35

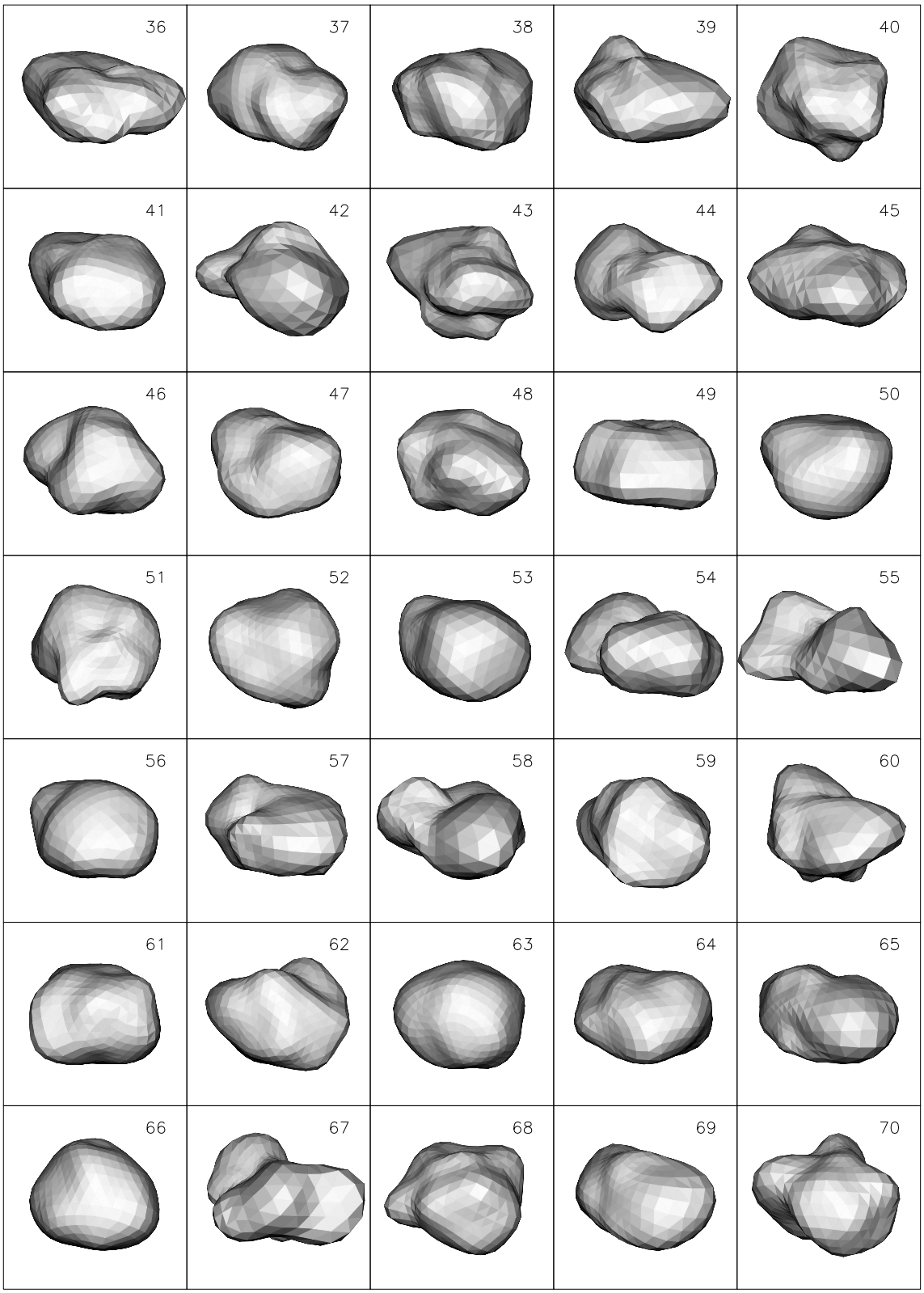


Figure C.3: Gaussian random spheres no. 36 ... 70

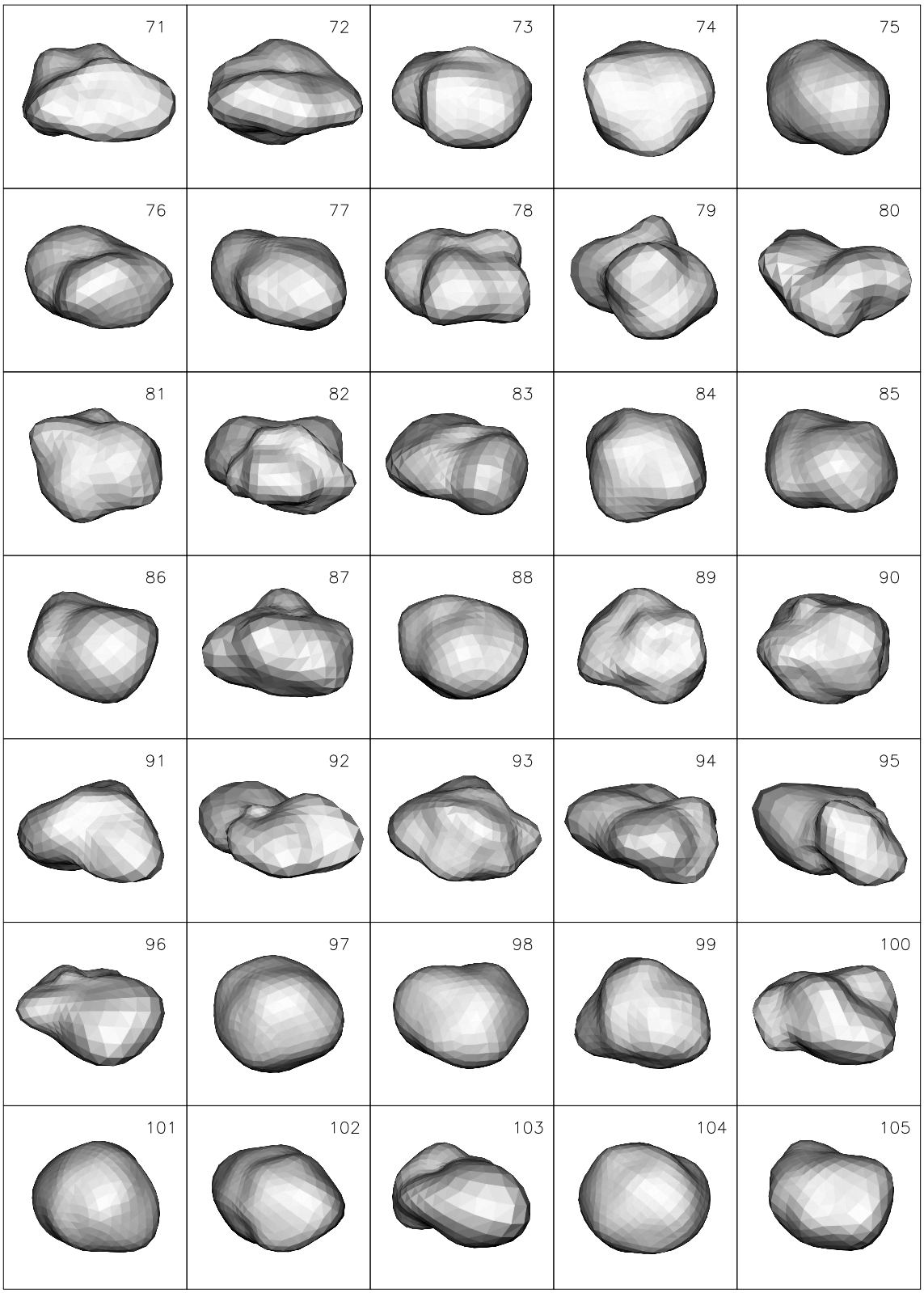


Figure C.4: Gaussian random spheres no. 71 ... 105

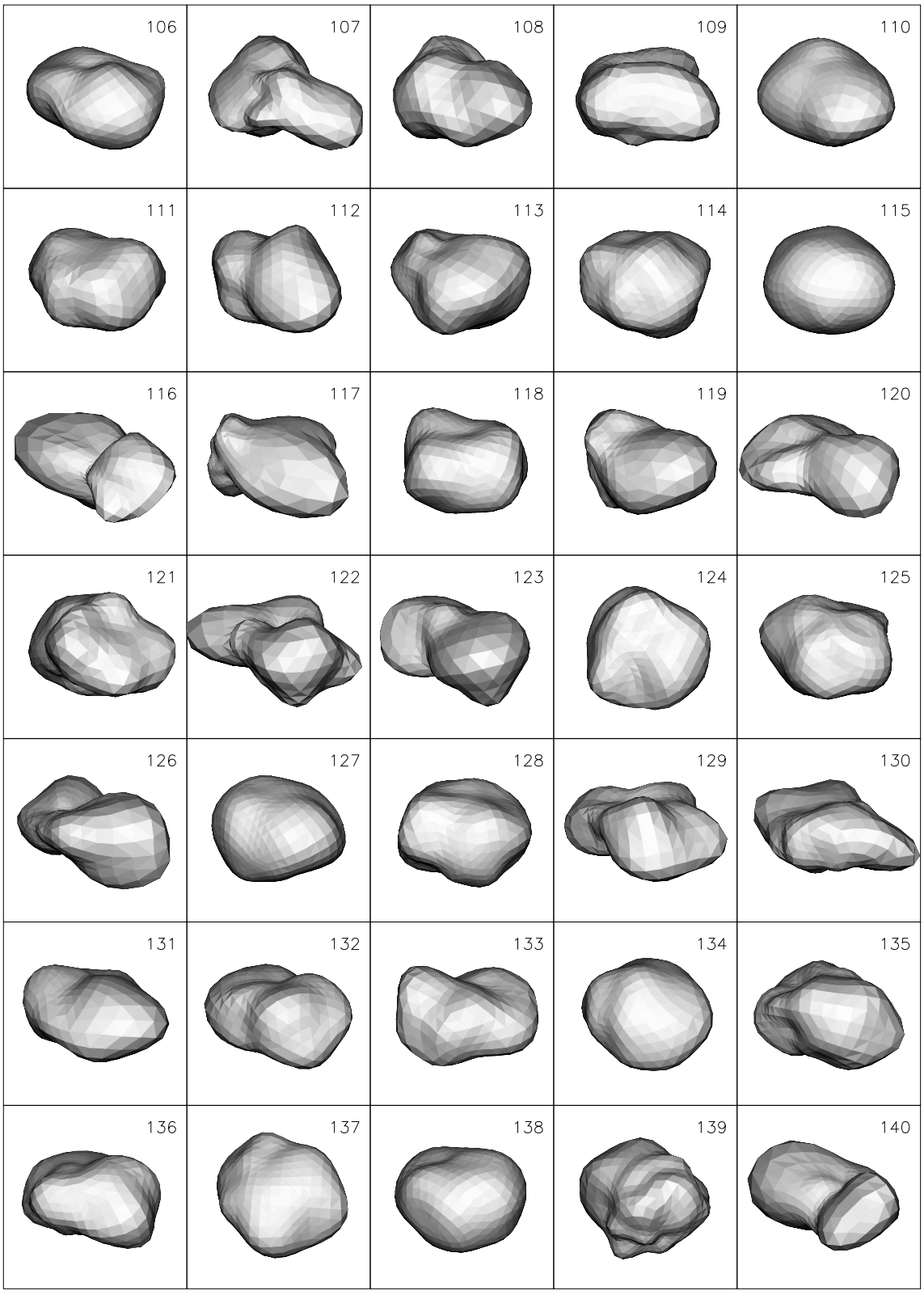


Figure C.5: Gaussian random spheres no. 106 ... 140

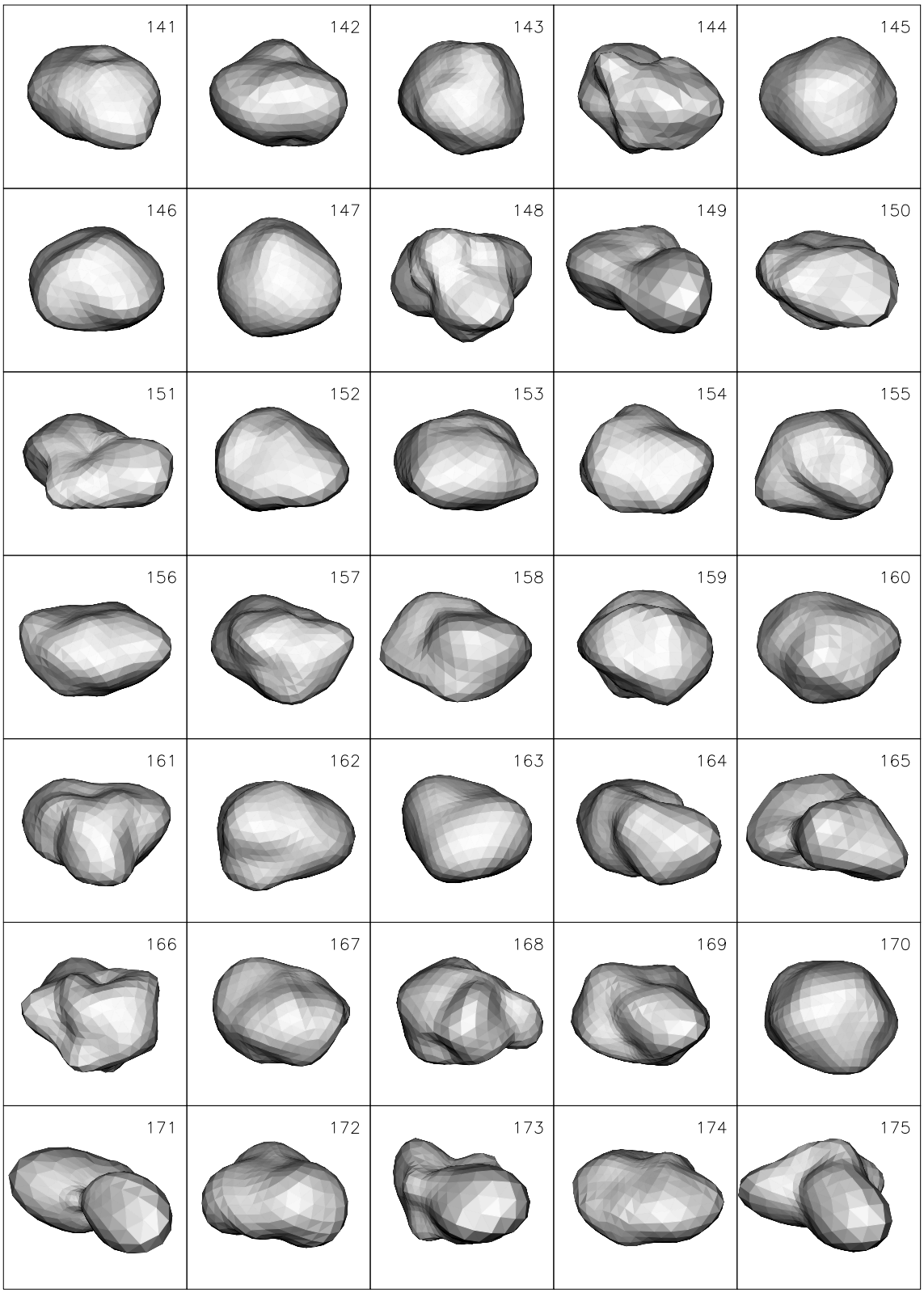


Figure C.6: Gaussian random spheres no. 141 ... 175

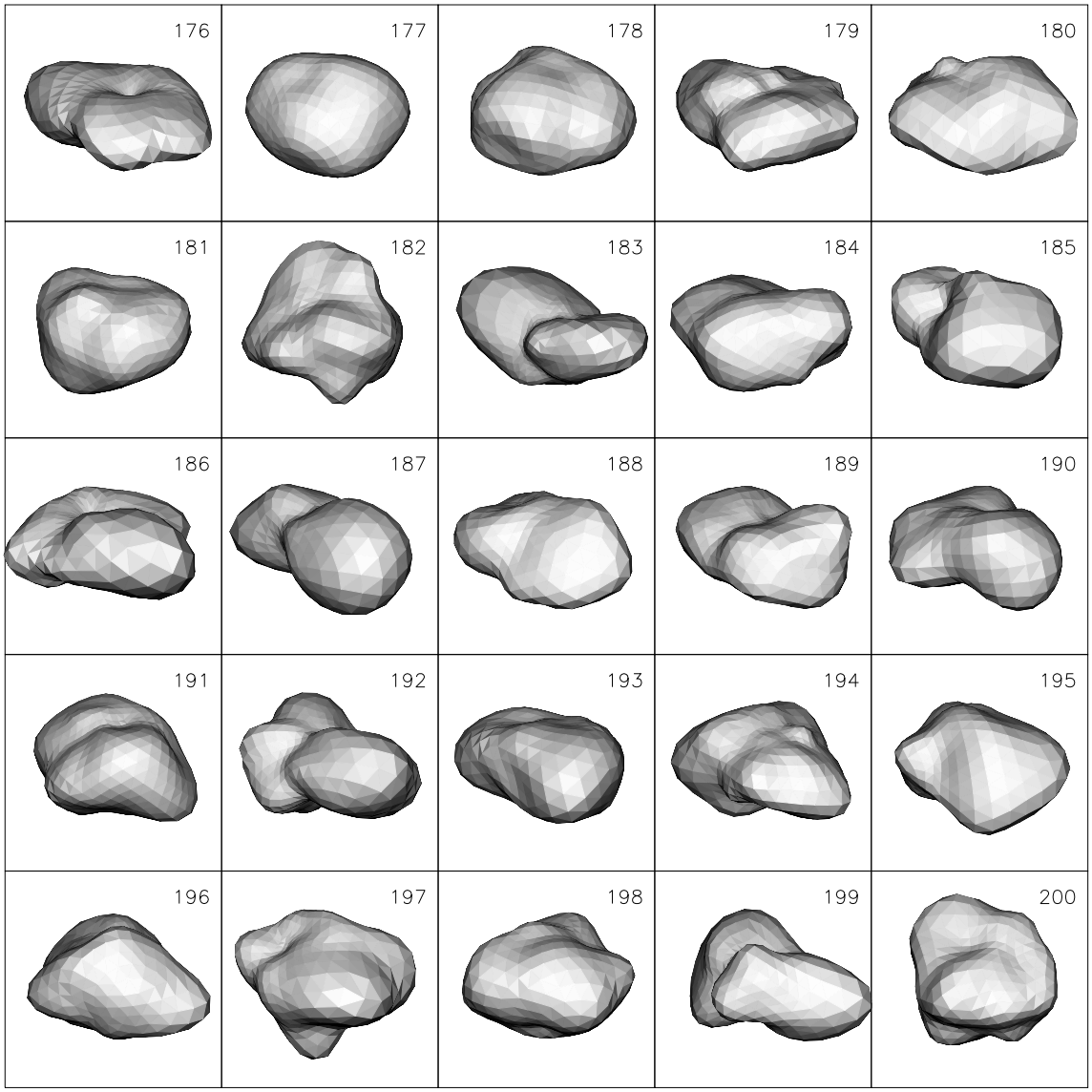


Figure C.7: Gaussian random spheres no. 176 ... 200

# Appendix D

# Shape models of real asteroids

Here we shall to present the shape models of asteroids that were used for our study of the YORP and Yarkovsky effect. All the bodies are represented by polyhedrons with typically several thousands of surface triangular facets. Their axes coincide with the main axis of inertia tensor and the origin is considered in the center of mass (assuming an uniform density). The shape models of the following asteroids are available from `http://www.psi.edu/pds/asteroid/`: (433) Eros, (1620) Geographos, (6489) Golevka, (25143) Itokawa, (243) Ida, 1998KY26, (4197) Toutatis.

For each asteroid there is a file with the following format:

```
v   x1 y1 z1
v   x2 y2 z2
v   x3 y3 z3
...
f   i1 j1 k1
f   i2 j2 k2
f   i3 j3 k3
...
```

The first part of the file represents a vertex table, each row starts with the letter `v` and contains $x$, $y$, $z$ coordinates of one vertex. The second part is a facet table, containing the linkages the vertices into facets. Each triangular facet begins with the letter `f`. Note the relationship between the number of facets $n_f$ and the number of vertices $n_v$ is $n_f = 2\,n_v - 4$ for the body consisting of triangular facets. All important quantities, like volume, inertia tensor, area of facets, etc., were determined by the technique described in Appendix B.

For all the bodies, which were used in our research of the Yarkovsky/YORP effect, we computed the parameter $\varphi_w$, describing the windmill asymmetry, see (Equation 3.11). (The windmill factor is dimensionalless quantity which depends only on the shape of the body and corresponds to the strength and "sense" of YORP effect.) The values for particular bodies can be found in Table D.1. The shape models can be seen in Figures D.2 – D.8.

| | | | | | |
|---|---|---|---|---|---|
| Golevka | -0.0009 | 6053 | -0.0064 | Deimos | -0.0121 |
| Castalia | 0.0031 | Bacchus | 0.0067 | Eros | 0.0219 |
| Gaspra | 0.0054 | 1998KY26 | 0.0080 | Kleopatra | -0.0354 |
| Geographos | 0.0054 | Itokawa | 0.0111 | Ida | -0.0436 |

Table D.1: Windmill factors $\varphi_w$ for 11 asteroids and Deimos.

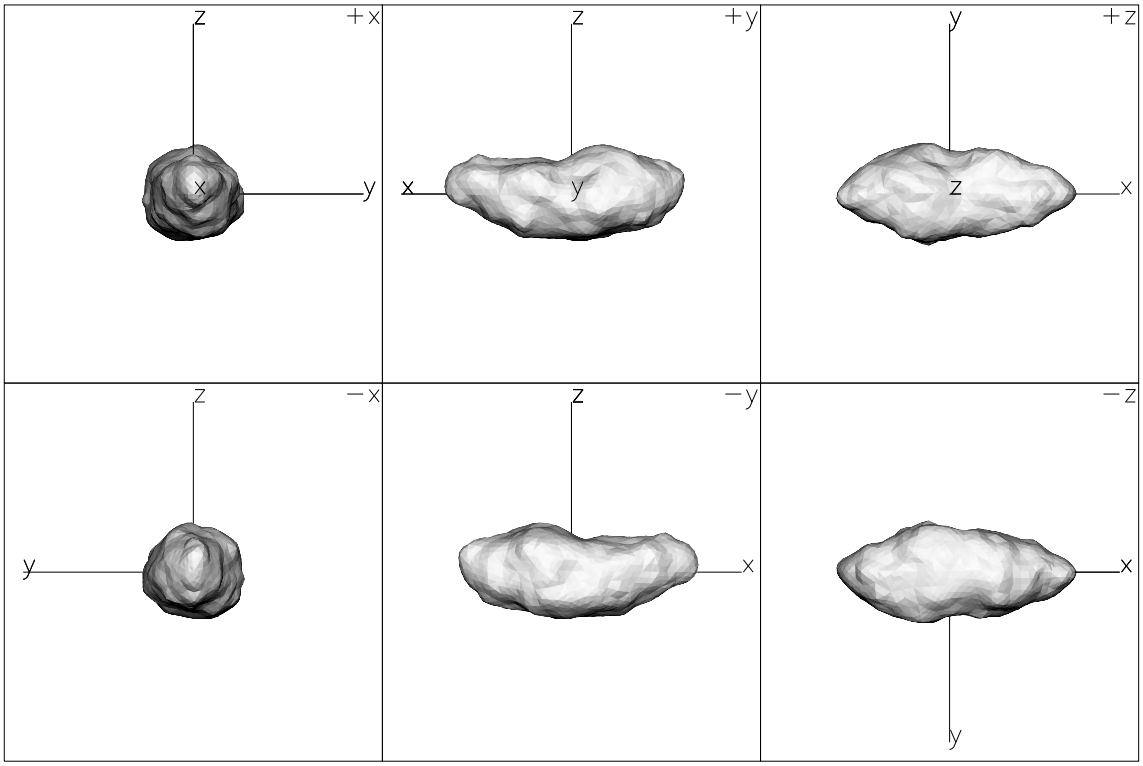


Figure D.1: The shape model of (1620) Geographos based on radar and optical observations. Dimension of each box is 8000 m. ([Hudson and Ostro, 1999]).

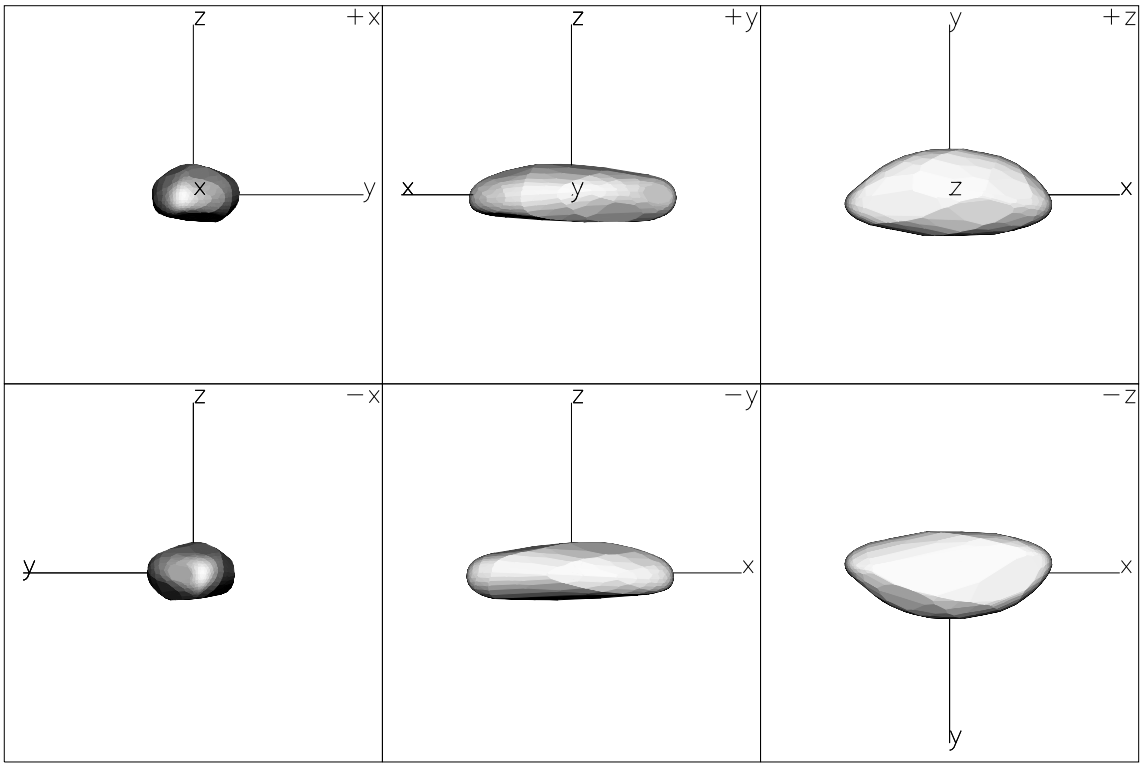


Figure D.2: Another shape model of (1620) Geographos determined by the lightcurve inversion method. Dimension of each box is 8000 m. (J. Ďurech, personal communication).

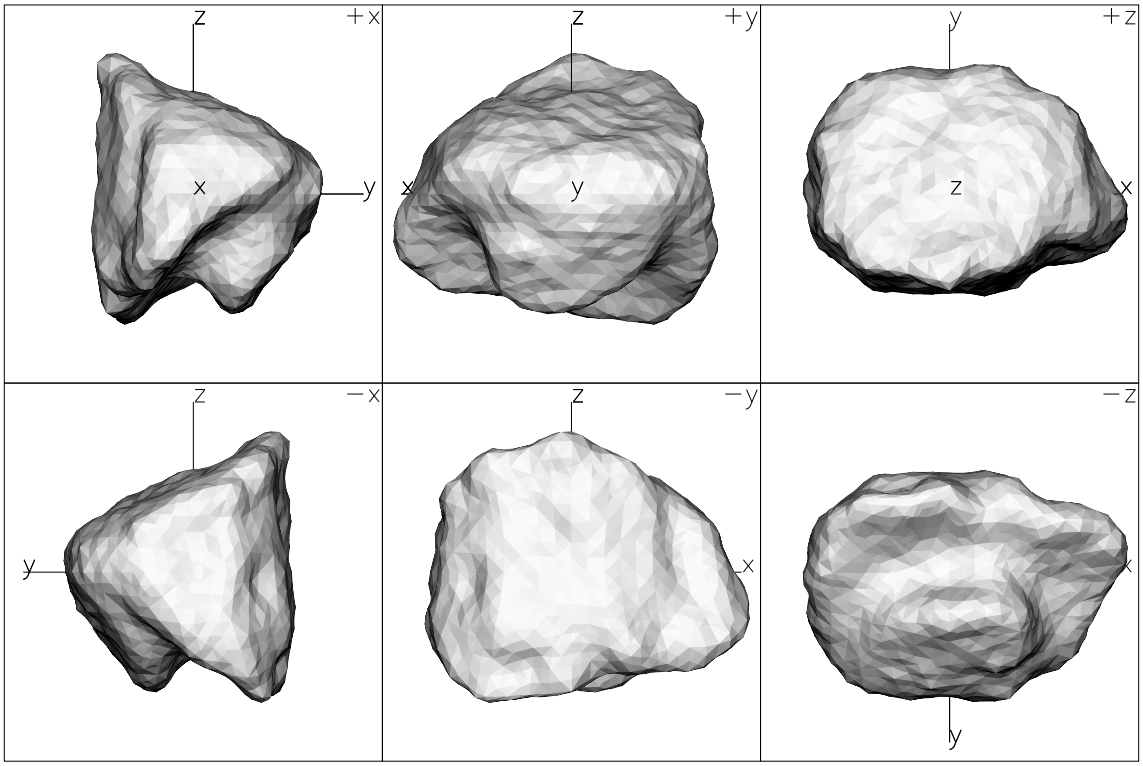


Figure D.3: The 4092-facets model of (6489) Golevka. The dimension of each box is 800 m. ([Hudson et al., 2000])

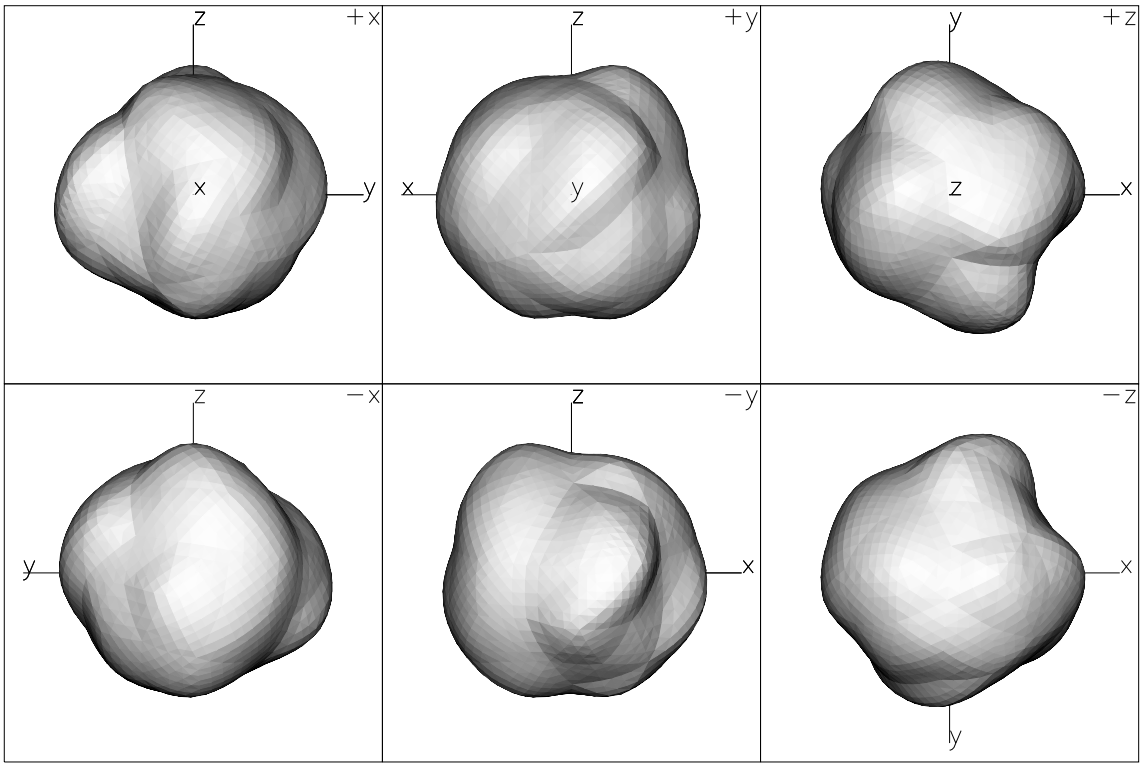


Figure D.4: The 4092-facets model of 1998 KY26. The dimension of each box is 30 m. ([Ostro et al., 1999])

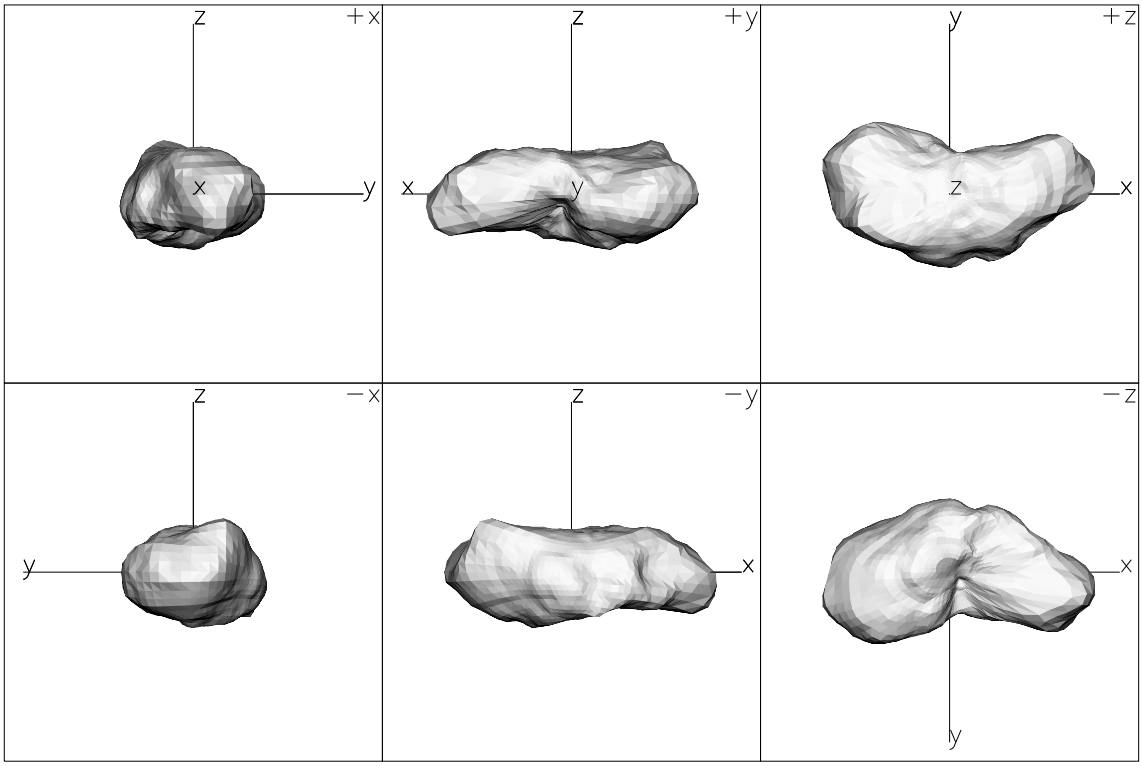


Figure D.5: The model of (243) Ida composed from 4036 surface triangular facets. The dimension of each box is 40 km. ([Thomas et al., 1996])

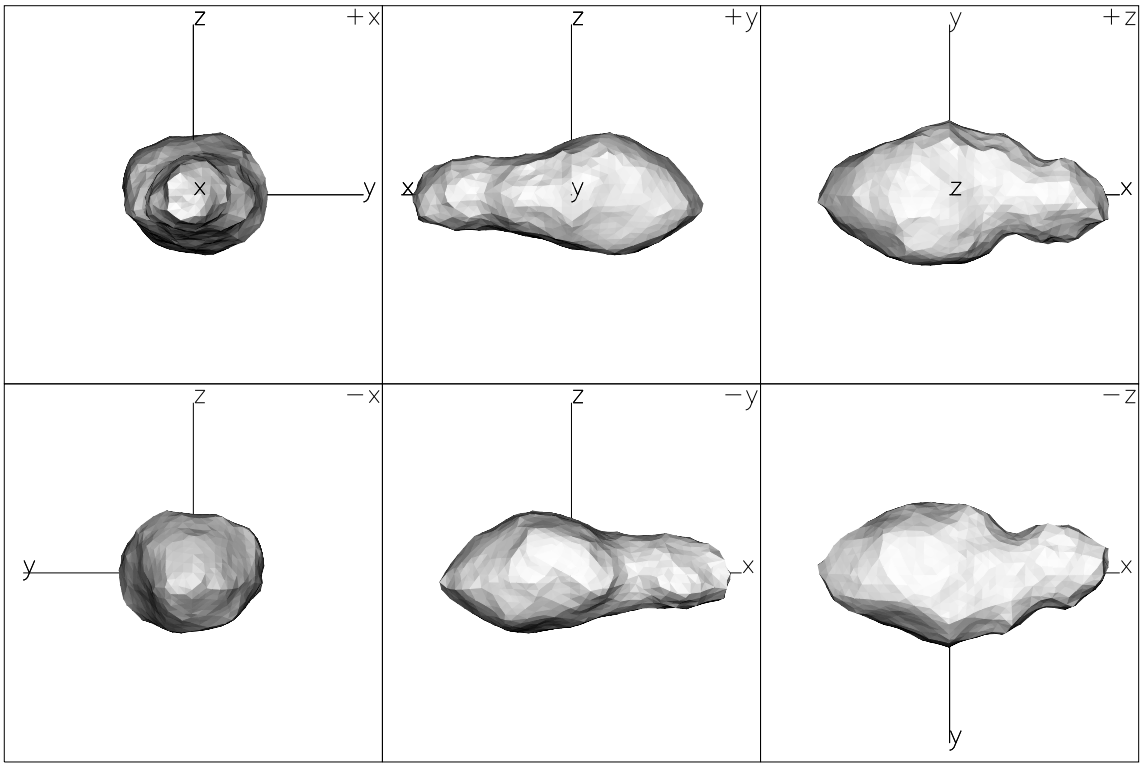


Figure D.6: The 12796-facet model of the asteroid (4179) Toutatis. The dimension of each box is 6 km. ([Hudson et al., 2003])

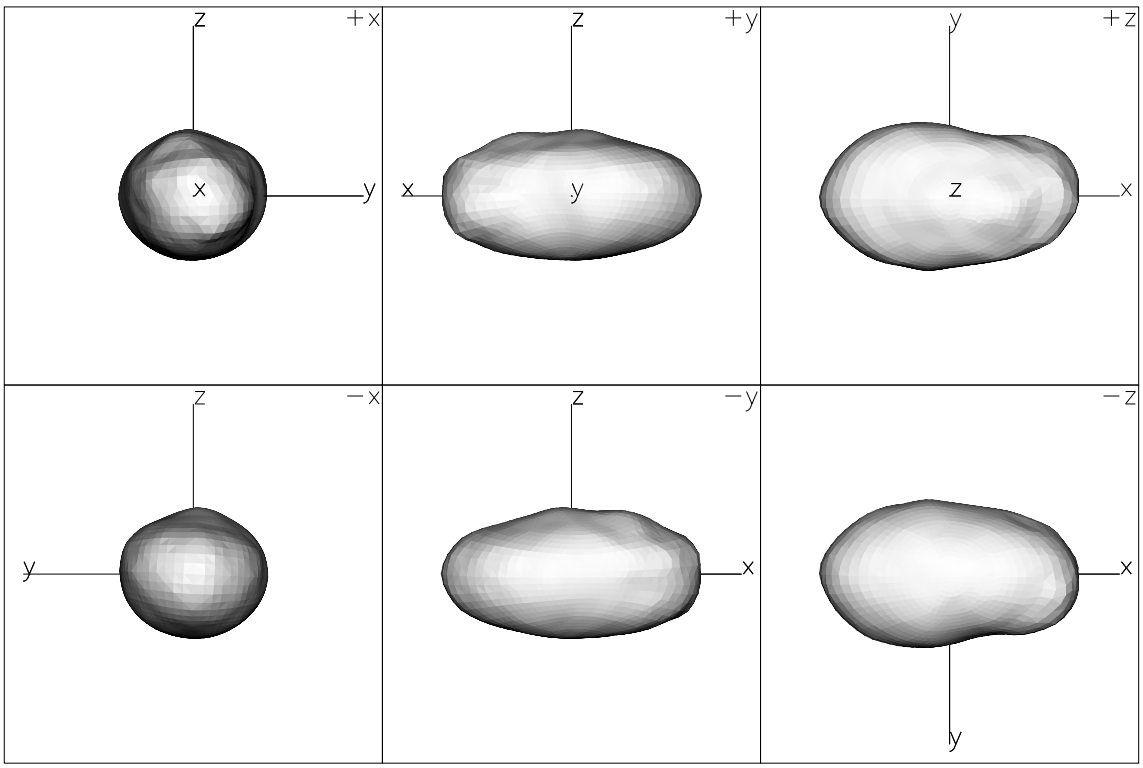


Figure D.7: The model of (25143) Itokawa. The dimension of each box is 800 m. At present, a more accurate shape model is available (e.g. [Demura et al., 2006]). Here we show the model determined by [Ostro et al., 2004].

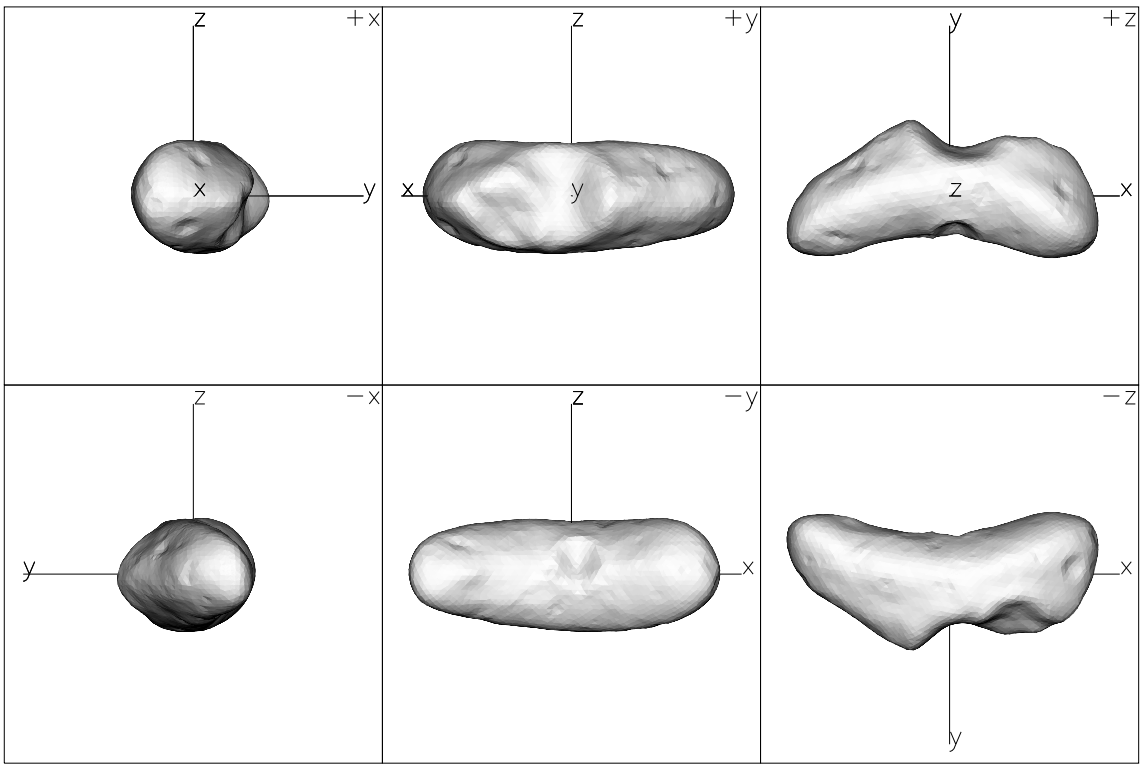


Figure D.8: The 7790-facets model of (433) Eros. The same model with reduced number of facets (1708 facets) was used for the study of the $K$ influence on the YORP effect. The dimension of each box is 40 km. ([Miller et al., 2002])

# Appendix E

# Publications

We list recorded independent citations below each publication.

### Refereed papers

- Vokrouhlický, D. and **Čapek, D.** (2002). YORP-Induced Long-Term Evolution of the Spin State of Small Asteroids and Meteoroids: Rubincam's Approximation. *Icarus*, **159**, 449-467.

    1. J.N. Spitale and R. Greenberg, Numerical evaluation of the general Yarkovsky effect: Effects on eccentricity, inclination and longitude of periapse, *Icarus*, **156**, 211, 2002.
    2. D.P. O'Brien and R. Greenberg, Steady-state size distributions for collisional populations: analytical solution with size-dependent strength, *Icarus* **164**, 334, 2003.
    3. M. Kaasalainen et al., Photometry and models of 8 near-Earth asteroids, *Icarus* **167**, 178, 2004.
    4. H. Hsieh, D.C. Jewitt and Y.R. Fernandez, The strange case of 133P/Elst-Pizarro: A comet among the asteroids, *Astron. J.* **127**, 2997, 2004.
    5. P. Pravec et al., Tumbling asteroids, *Icarus* **173**, 108, 2005.
    6. D. Nesvorný and W.F. Bottke, Direct detection of the Yarkovsky effect for main-belt asteroids, *Icarus* **170**, 324, 2004.
    7. D.P. O'Brien, *The Collisional and Dynamical Evolution of the Main-Belt, NEA, and TNO Populations*, PhD Dissertation, University of Arizona, 2004.
    8. A.W. Harris, YORP alteration of asteroid spins: Why are slow rotators tumbling and not synchronized?, *BAAS* **36**, 1185 (also http://www.aas.org/publications/baas/v36n4/dps2004/137.htm).
    9. D.P. O'Brien and R. Greenberg, Collisional and dynamical evolution of the main-belt and NEA size distributions, *Icarus* **178**, 179, 2005.
    10. J. Ďurech, 433 Eros – comparison of lightcurve extrema from 1901-1931 with the actual rotation state, *Astron. Astrophys.* **431**, 381, 2005.
    11. M. Ćuk and J.A. Burns, Effects of thermal radiation on the dynamics of binary NEAs, *Icarus* **176**, 418, 2005.
    12. D.C. Richardson and K.J. Walsh, Binary minor planets, *Ann. Rev. Earth Planet. Sci.* **34**, 47, 2006.
    13. M. Makuch, N.V. Brilliantov, M. Sremčević, F. Spahn and A.V. Krivov, Stochastic circumplanetary dynamics of rotating non-spherical dust particles, *Planet. Sp. Sci.* **54**, 855, 2006.
    14. D.J. Scheeres, The dynamical evolution of uniformly rotating asteroids subject to YORP, *Icarus*, in press, 2007.

15. E. Mysen, Canonical rotation variables and non-Hamiltonian forces: solar radiation pressure effects on asteroid rotation, *Mon. Not. R. Astr. Soc.* **372**, 1345, 2006.
16. P. Jenniskens, Meteor Showers and their Parent Comets (Cambridge, Cambridge University Press, 2006) p. 536.
17. M. Delbó, A. dell'Oro, A.W. Harris, S. Mottola and M. Mueller, Thermal inertia of near-Earth asteroids and implications for the magnitude of the Yarkovsky effect, *Icarus*, in press, 2007.
18. V. Carruba, F. Roig, T.A. Michtchenko, S. Ferraz-Mello and D. Nesvorný, Modeling close encounters with massive asteroids: a Markovian approach, *Astron. Astrophys.*, in press, 2007.

- Chesley, S. R., Ostro, S. J., Vokrouhlický, D., **Čapek, D.**, Giorgini, J. D., Nolan, M. C., Margot, J.-L., Hine, A. A., Benner, L. A. M., and Chamberlin, A. B. (2003). Direct Detection of the Yarkovsky Effect by Radar Ranging to Asteroid 6489 Golevka. *Science*, **302**, 1739–1742.

1. E.S. Reich, Sunlight's gentle nudge on asteroids detected, http://www.newscientist.com/news/.
2. S. Ives, Will discovery help repel asteroids headed for Earth?, Science and Technology section of *NationalGeographic.Com*, December 11, 2003.
(also http://news.nationalgeographic.com/news/science.html)
3. S. Hurtley and P. Szuromi, A nudge from Yarkovsky, *Science* **302**, 1621, 2003.
4. D. Morrison, Precision NEO Orbits and the Yarkovsky Effect, http://nai.arc.nasa.gov/impact/news_detail.cfm?ID= 132
5. D. Tytell, The Asteroid and the Pea, *Sky & Telescope*
(also http://skyandtelescope.com/news/article_1126_1.asp)
6. B. Dumé, Radar reveals asteroid force, *Physics Web*, http://physicsweb.org/article/news/7/12/3
7. D. Tytell, Sunlight makes asteroids spin in harmony, *Sky & Telescope*, p. 26, January 2004.
8. C. Schreiber, Kann der Yarkovsky-Effekt die Asteroiden neu gruppieren?, *Telepolis*, http://www.heise.de/tp/r4/artikel/16/16261/1.html
9. http://www.masterliness.com/a/Yarkovsky.effect.htm
10. http://www.absoluteastronomy.com/encyclopedia/Y/Ya/Yarkovsky_effect.htm
11. http://www.economicexpert.com/a/Yarkovsky:effect.html
12. *Yarkovsky effect* in Wikipedia http://en.wikipedia.org/wiki/Yarkovsky_effect
13. U. Penco, A. Dell'Oro, P. Paolicchi et al., Yarkovsky depletion and asteroid collisional evolution, *Planet. Sp. Science* **52**, 1087, 2004.
14. R.D. Lorentz and J.N. Spitale, The Yarkovsky effect as a heat engine, *Icarus* **170**, 229, 2004.
15. R. Michelsen, Near-Earth Asteroids from discovery to characterization, *PhD Thesis*, N. Bohr Institute for Astronomy, Physics and Geophysics, University of Copenhagen, 2004.
16. V. Carruba, Dynamics of asteroid families and irregular satellites of jovian planets, *PhD Thesis*, Cornell University, 2004 (http://www.astro.iag.usp.br/~valerio/PUB/thesis.pdf).
17. A. Cellino, A. Dell'Oro and V. Zappalà, Asteroid families: open problems, *Planet. Sp. Sci.* **52**, 1075, 2004.
18. A. Dell'Oro, G. Bigongiari, P. Paolicchi and A. Cellino, Asteroid families: evidence of ageing of the proper elements, *Icarus* **169**, 341, 2004.
19. B.J. Butler, D.B. Campbell, I. de Pater, et al., Solar system science with SKA, *New Astronomy Revs.* **48**, 1511, 2004.
20. A. Lemaitre, Asteroid family classification from very large catalogs, in: *Dynamics of Populations of Planetary Systems*, IAU Colloquium 197, Cambridge University Press, 2005, p. 135.

21. D. Nesvorný, R. Jedicke, R.J. Whiteley and Z. Ivezić, Evidence for asteroids space weathering from the Sloan Digital Sky Survey, *Icarus* **173**, 132, 2005.
22. S.R. Valluri, P. Yu, G.E. Smith, et al., An extension of Newton's apsidal precession theorem, *Mon. Not. R. Astron. Soc.* **358**, 1273, 2005.
23. V. Trimble and M. Aschwanden, Astrophysics in 2004, *Publ. Astron. Soc. Pacific* **117**, 311, 2005.
24. R. Kippenhahn, Der sanfte druck des lichtes, *Sterne und Weltraum*, Sep 2005, p. 46.
25. P. Tanga, Impact of Gaia on dynamics and evolution of the Solar System, in *The Three-Dimensional Universe with Gaia*, C. Turon, K.S. O'Flaherty, M.A.C. Perryman (Eds.), p. 243, 2005.
26. F. Yoshida and T. Nakamura, Size distribution of faint Jovian L4 Trojan asteroids, *Astron. J.* **130**, 2900, 2005.
27. J.R. Gott, Lagrange L-4/L-5 points and the origin of our Moon and Saturn's Moons and rings, *Ann. New York Acad. Sci.* **1065**, 325, 2005.
28. G. Wurm and O. Krauss, Concentration and sorting of chondrules and CAIs in the late Solar Nebula, *Icarus* **180**, 487, 2006.
29. K.J. Walsh and D.C. Richardson, Binary near-Earth asteroid formation: Rubble pile model of tidal distortions, *Icarus* **180**, 201, 2006.
30. S. Marchi, P. Paolicchi, M. Lazzarin and S. Magrin, A general spectral slope-exposure relation for S-type main belt and near-Earth asteroids, *Astron. J.* **131**, 1138, 2006.
31. G. Beekman, I.O. Yarkovsky and the discovery of his effect, *J. History of Astronomy* **37**, 71, 2006.
32. G. Cheng, J. Duan, S. Zhang and Y. Chen, Inverse thinking and problems for light scattering, *Progress in Physics* **26**, 51, 2006 (in chinese).
33. D.C. Richardson and K.J. Walsh, Binary minor planets, *Ann. Rev. Earth Planet. Sci.* **34**, 47, 2006.
34. G.B. Valsecchi, A. Milani, A. Rossi and G. Tommei, The SRT, Near-Earth objects, and space debris, *Mem. Soc. Astron. Italiana* **10**, 186, 2006.
35. M. Delbó, A. dell'Oro, A.W. Harris, S. Mottola and M. Mueller, Thermal inertia of near-Earth asteroids and implications for the magnitude of the Yarkovsky effect, *Icarus*, in press, 2007.
36. D.F. Lupishko, M. Di Martino and R.P. Binzel, Near-Earth objects as principal impactors on the Earth, in: *Near Earth Objects, our Celestial Neighbors: Opportunity and Risk*, A. Milani, G.B. Valsecchi and D. Vokrouhlický, Eds., Cambridge Univ. Press, 2007, in press.
37. P. Michel and K.A. Holsapple, Tidal disturbances of small cohesionless bodies: limit planetary distances and applications, in: *Near Earth Objects, our Celestial Neighbors: Opportunity and Risk*, A. Milani, G.B. Valsecchi and D. Vokrouhlický, Eds., Cambridge Univ. Press, 2007, in press.

- Vokrouhlický, D., **Čapek, D.**, Kaasalainen, M., and Ostro, S. J. (2004). Detectability of YORP rotational slowing of asteroid 25143 Itokawa. *Astronomy and Astrophysics*, 414:L21–L24.

1. A.W. Harris and P. Pravec, Rotational properties of asteroids, comets and TNOs, in: *Asteroids, Comets and Meteors*, eds. D. Lazzaro, S. Ferraz-Mello and J.A. Fernandez, Cambridge University Press, p. 439, 2006.
2. D.J. Scheeres, M. Abe, R. Nakamura, R.W. Gaskell, P.A. Abell, Predicted rotational deceleration of asteroid Itokawa due to YORP, abstract COSPAR2006-A-02665 at COSPAR meeting, Beijing, 2006. (http://www.cosis.net/abstracts/COSPAR2006/02665/COSPAR2006-A-02665.pdf)

3. M. Kaasalainen, J. Ďurech, B.D. Warner, Y.N. Krugly, N.M. Gaftonyuk, Acceleration of the rotation of asteroid 1862 Apollo by radiation torques, *Nature*, **446**, 420, 2007.
4. D.J. Scheeres, The dynamical evolution of uniformly rotating asteroids subject to YORP, *Icarus*, in press, 2007.
5. D.J. Scheeres, M. Abe, M. Yoshikawa, R. Nakamura, R.W. Gaskell, P.A. Abell, The effect of YORP on Itokawa, *Icarus*, submitted, 2007.
6. T.G. Müller, T. Sekiguchi, M. Kaasalainen, M. Abe and S. Hagesawa, Itokawa: The power of ground-based mid-infrared observations, in: *Near Earth Objects, our Celestial Neighbors: Opportunity and Risk*, A. Milani, G.B. Valsecchi and D. Vokrouhlický, Eds., Cambridge Univ. Press, 2007, in press.

- **Čapek, D.** and Vokrouhlický, D. (2004). The YORP effect with finite thermal conductivity. *Icarus*, 172:526–536.

1. J. Ďurech, 433 Eros – comparison of lightcurve extrema from 1901-1931 with the actual rotation state, *Astron. Astrophys.* **431**, 381, 2005.
2. V. Carruba, T.A. Michtchenko, F. Roig, S. Ferraz-Mello and D. Nesvorný, On the V-type asteroids outside the Vesta family. I. Interplay ..., *Astron. Astrophys.* **441**, 819, 2005.
3. D.J. Scheeres, The dynamical evolution of uniformly rotating asteroids subject to YORP, *Icarus*, in press, 2007.
4. E. Mysen, Canonical rotation variables and non-Hamiltonian forces: solar radiation pressure effects on asteroid rotation, *Mon. Not. R. Astr. Soc.* **372**, 1345, 2006.
5. P. Jenniskens, Meteor Showers and their Parent Comets (Cambridge, Cambridge University Press, 2006) p. 536.
6. M. Kaasalainen, J. Ďurech, B.D. Warner, Y.N. Krugly, N.M. Gaftonyuk, Acceleration of the rotation of asteroid 1862 Apollo by radiation torques, *Nature*, **446**, 420, 2007.
7. M. Delbó, A. dell'Oro, A.W. Harris, S. Mottola and M. Mueller, Thermal inertia of near-Earth asteroids and implications for the magnitude of the Yarkovsky effect, *Icarus*, in press, 2007.
8. M. Delbò, P. Tanga and F. Mignard, On the detection of the Yarkovsky effect on near-Earth asteroids by means of Gaia, *Planet. Sp. Sci.*, in press, 2007.
9. V. Carruba, F. Roig, T.A. Michtchenko, S. Ferraz-Mello and D. Nesvorný, Modeling close encounters with massive asteroids: a Markovian approach, *Astron. Astrophys.*, in press, 2007.

- Vokrouhlický, D., **Čapek, D.**, Chesley, S. R., and Ostro, S. J. (2005a). Yarkovsky detection opportunities. I. Solitary asteroids. *Icarus*, 173:166–184.

1. D. Nesvorný and W.F. Bottke, Direct detection of the Yarkovsky effect for main-belt asteroids, *Icarus* **170**, 324, 2004.
2. T.G. Müller, T. Sekiguchi, M. Kaasalainen, M. Abe and S. Hagesawa, Itokawa: The power of ground-based mid-infrared observations, in: *Near Earth Objects, our Celestial Neighbors: Opportunity and Risk*, A. Milani, G.B. Valsecchi and D. Vokrouhlický, Eds., Cambridge Univ. Press, 2007, in press.
3. M. Delbò, P. Tanga and F. Mignard, On the detection of the Yarkovsky effect on near-Earth asteroids by means of Gaia, *Planet. Sp. Sci.*, in press, 2007.

- Vokrouhlický, D., **Čapek, D.**, Chesley, S. R., and Ostro, S. J. (2005b). Yarkovsky detection opportunities II. Binary asteroids.. *Icarus*, 179:128–138.

1. A. Morbidelli, H.F. Levison and W.F. Bottke, Formation of the binary near-Earth object 1996 FG(3): Can binary NEOs be the source of short-CRE meteorites? *Meteor. Planet. Sci.* **41**, 875, 2006.
2. D.J. Scheeres, The dynamics of NEO binary asteroids, in: *Near Earth Objects, our Celestial Neighbors: Opportunity and Risk*, A. Milani, G.B. Valsecchi and D. Vokrouhlický, Eds., Cambridge Univ. Press, 2007, in press.

**Proceedings**

- **Čapek, D.** and Vokrouhlický, D. (2005). Accurate model for the Yarkovsky effect. In Knezevic, Z. and Milani, A., editors, *IAU Colloq. 197: Dynamics of Populations of Planetary Systems*, p. 171–178.

- Brož, M. and Vokrouhlický, D. and Bottke, W. F. and Nesvorný, D. and Morbidelli, A. and **Čapek, D.** (2006), Non-gravitational forces acting on small bodies. *IAU Symp. 229: Asteroids, Comets, and Meteors*, p. 351-365.

**Abstracts**

- **Čapek, D.** and Vokrouhlický, D. (2002). Yarkovsky force and torque on Gaussian random spheres. Poster at *Asteroids, Comets and Meteors*, Berlin, Germany.

- S.R. Chesley, D. Vokrouhlický, D. **Čapek** and S. Ostro (2003). Test of the Yarkovsky effect using radar ranging to Golevka: Place your bets, *BAAS* **35**, 1033.

- D. Vokrouhlický, **D. Čapek**, S.R. Chesley and S. Ostro (2004). Next Yarkovsky candidates, *New trends in near-Earth asteroids research*, Arecibo, Puerto Rico.

- S.R. Chesley, S.J. Ostro, D. Vokrouhlický, J.D. Giorgini, **D. Čapek**, L.A.M. Benner, M.C. Nolan and J.-L. Margot (2005). Direct detection of the Yarkovsky effect: Progress and prognostications, *BAAS* **37**, 521.

- **Čapek, D.** and Vokrouhlický, D. (2005). Plausible constraint on Golevka's regolith from an accurate Yarkovsky/YORP effect model. Poster at *Asteroids, Comets and Meteors*, Búzios, Rio de Janeiro, Brazil.

# Bibliography


[Bertotti et al., 2003] Bertotti, B., Farinella, P., and Vokrouhlický, D. (2003). *Physics of Solar system (Dynamics and evolution, space physics, and spacetime structure)*. Kluwer Academic Press, Dordrecht.

[Bottke et al., 2002] Bottke, W. F., Morbidelli, A., Jedicke, R., Petit, J.-M., Levison, H. F., Michel, P., and Metcalfe, T. S. (2002). Debiased orbital and absolute magnitude distribution of the near-Earth objects. *Icarus*, 156:399–433.

[Bottke et al., 2001] Bottke, W. F., Vokrouhlický, D., Brož, M., Nesvorný, D., and Morbidelli, A. (2001). Dynamical spreading of asteroid families by the Yarkovsky effect. *Science*, 294:1693–1696.

[Breiter et al., 2007] Breiter, S., Michalska, H., Vokrouhlický, D., and Borczyk, W. (2007). Radiation induced torques on spheroids. *Astronomy and Astrophysics,* in press.

[Brož, 2006] Brož, M. (2006). *Yarkovsky effect and the dynamics of the Solar System. PhD thesis*. Charles University, Prague.

[Burns et al., 1979] Burns, J. A., Lamy, P. L., and Soter, S. (1979). Radiation forces on small particles in the solar system. *Icarus*, 40:1–48.

[Burns and Safronov, 1973] Burns, J. A. and Safronov, V. S. (1973). Asteroid nutation angles. *Monthly Notices of the Royal Astronomical Society*, 165:403–411.

[Čapek and Vokrouhlický, 2002] Čapek, D. and Vokrouhlický, D. (2002). Yarkovsky force and torque on Gaussian random spheres. Poster at *Asteroids, Comets and Meteors,* Berlin, Germany.

[Čapek and Vokrouhlický, 2004] Čapek, D. and Vokrouhlický, D. (2004). The YORP effect with finite thermal conductivity. *Icarus*, 172:526–536.

[Čapek and Vokrouhlický, 2005a] Čapek, D. and Vokrouhlický, D. (2005a). Accurate model for the Yarkovsky effect. In Knežević, Z. and Milani, A., editors, *IAU Colloq. 197: Dynamics of Populations of Planetary Systems*, pages 171–178.

[Čapek and Vokrouhlický, 2005b] Čapek, D. and Vokrouhlický, D. (2005b). Plausible constraint on Golevka's regolith from an accurate Yarkovsky/YORP effect model. Poster at *Asteroids, Comets and Meteors,* Búzios, Rio de Janeiro, Brazil.

[Chesley et al., 2003] Chesley, S. R., Ostro, S. J., Vokrouhlický, D., Čapek, D., Giorgini, J. D., Nolan, M. C., Margot, J.-L., Hine, A. A., Benner, L. A. M., and Chamberlin, A. B. (2003). Direct detection of the Yarkovsky effect by radar ranging to asteroid 6489 Golevka. *Science*, 302:1739–1742.

[Chesley et al., 2006] Chesley, S. R., Vokrouhlický, D., and Matson, R. D. (2006). Direct measurement of the Yarkovsky effect acting on near-Earth asteroid 1992 BF. In *Bull. Am. Astron. Soc.*, volume 38, page 591.

[Cremers, 1972] Cremers, C. J. (1972). Thermal conductivity of Apollo 12 fines at intermediate density. *Moon*, 4:88.

[Davies et al., 1996] Davies, M. E., Colvin, T. R., Belton, M. J. S., Veverka, J., and Thomas, P. C. (1996). The direction of the north pole and the control network of asteroid 243 Ida. *Icarus*, 120:33–37.

[Delbò et al., 2006] Delbò, M., Dell'Oro, A., Harris, A. W., Mottola, S., and Mueller, M. (2006). Thermal inertia of near-Earth asteroids and strength of the Yarkovsky effect. In *Bull. Am. Astron. Soc.*, volume 38.

[Delbò et al., 2007] Delbò, M., dell'Oro, A., Harris, A. W., Mottola, S., and Mueller, M. (2007). Thermal inertia of near-earth asteroids and implications for the magnitude of the yarkovsky effect. *Icarus,* in press.

[Demura et al., 2006] Demura, H., Kobayashi, S., Nemoto, E., Matsumoto, N., Furuya, M., Yukishita, A., Muranaka, N., Morita, H., Shirakawa, K., Maruya, M., Ohyama, H., Uo, M., Kubota, T., Hashimoto, T., Kawaguchi, J., Fujiwara, A., Saito, J., Sasaki, S., Miyamoto, H., and Hirata, N. (2006). Pole and global shape of 25143 Itokawa. *Science*, 312:1347–1349.

[Dobrovolskis, 1996] Dobrovolskis, A. R. (1996). Inertia of any polyhedron. *Icarus*, 124:698–704.

[Ďurech, 2005] Ďurech, J. (2005). 433 Eros - comparison of lightcurve extrema from 1901-1931 with the present rotation state. *Astronomy and Astrophysics*, 431:381–383.

[Efroimsky and Lazarian, 2000] Efroimsky, M. and Lazarian, A. (2000). Inelastic dissipation in wobbling asteroids and comets. *Monthly Notices of the Royal Astronomical Society*, 311:269–278.

[Farinella et al., 1992] Farinella, P., Davis, D. R., Paolicchi, P., Cellino, A., and Zappalà, V. (1992). Asteroid collisional evolution - an integrated model for the evolution of asteroid rotation rates. *Astronomy and Astrophysics*, 253:604–614.

[Farinella et al., 1998] Farinella, P., Vokrouhlick/'y, D., and Hartmann, W. K. (1998). Meteorite delivery via Yarkovsky orbital drift. *Icarus*, 132:378–387.

[Gaskell et al., 2006] Gaskell, R., Saito, J., Ishiguro, M., Kubota, T., Hashimoto, T., Hirata, N., Abe, S., Barnouin-Jha, O. S., and Scheeres, D. (2006). Global topography of asteroid 25143 Itokawa. In Mackwell, S. and Stansbery, E., editors, *37th Annual Lunar and Planetary Science Conference*, page 1876.

[Hamilton and Matson, 1987] Hamilton, R. H. and Matson, D. L. (1987). Thermal effects of insolation propagation into the regoliths of airless bodies. *Icarus*, 72:84–94.

[Helin et al., 1991] Helin, E., Lawrence, K., Rose, P., and Williams, G. (1991). 1991 JX. *IAU Circ.*, 5268:1.

[Hudson et al., 2000] Hudson, R. S., Ostro, S. J., Jurgens, R. F., Rosema, K. D., Giorgini, J. D., Winkler, R., Rose, R., Choate, D., Cormier, R. A., Franck, C. R., Frye, R., Howard, D., Kelley, D., Littlefair, R., Slade, M. A., Benner, L. A. M., Thomas, M. L., Mitchell, D. L., Chodas, P. W., Yeomans, D. K., Scheeres, D. J., Palmer, P., Zaitsev, A., Koyama, Y.,

Nakamura, A., Harris, A. W., and Meshkov, M. N. (2000). Radar observations and physical model of asteroid 6489 Golevka. *Icarus*, 148:37–51.

[Hudson et al., 2003] Hudson, R. S., Ostro, S. J., and Scheeres, D. J. (2003). High-resolution model of asteroid 4179 Toutatis. *Icarus*, 161:346–355.

[Hudson and Ostro, 1995] Hudson, R. S. and Ostro, S. J. (1995). Shape and non-principal axis spin state of asteroid 4179 Toutatis. *Science*, 270:84–86.

[Hudson and Ostro, 1999] Hudson, R. S. and Ostro, S. J. (1999). Physical Model of asteroid 1620 Geographos from radar and optical data. *Icarus*, 140:369–378.

[Isachenko et al., 1969] Isachenko, V., Osipova, V., and Sukomel, A. (1969). *Heat transfer*. Mir publishers, Moscow.

[Kaasalainen et al., 2007] Kaasalainen, M., Ďurech, J., Warner, B. D., Krugly, Y. N., and Gaftonyuk, N. M. (2007). Acceleration of the rotation of asteroid 1862 Apollo by radiation torques. *Nature*, 446:420–422.

[Kaasalainen et al., 2003] Kaasalainen, M., Kwiatkowski, T., Abe, M., Piironen, J., Nakamura, T., Ohba, Y., Dermawan, B., Farnham, T., Colas, F., Lowry, S., Weissman, P., Whiteley, R. J., Tholen, D. J., Larson, S. M., Yoshikawa, M., Toth, I., and Velichko, F. P. (2003). CCD photometry and model of MUSES-C target (25143) 1998 SF36. *Astronomy and Astrophysics*, 405:L29–L32.

[Kryszczyńska et al., 1999] Kryszczyńska, A., Kwiatkowski, T., Breiter, S., and Michałowski, T. (1999). Relation between rotation and lightcurve of 4179 Toutatis. *Astronomy and Astrophysics*, 345:643–645.

[La Spina et al., 2004] La Spina, A., Paolicchi, P., Kryszczyńska, A., and Pravec, P. (2004). Retrograde spins of near-Earth asteroids from the Yarkovsky effect. *Nature*, 428:400–401.

[Lowry et al., 2007] Lowry, S. C., Fitzsimmons, A., Pravec, P., Vokrouhlický, D., Boehnhardt, H., A., T. P., A., G., M., I., J., I., and P., K. (2007). Direct detection of the asteroidal YORP effect. *Science,* in press.

[Margot et al., 2002] Margot, J. L., Nolan, M. C., Benner, L. A. M., Ostro, S. J., Jurgens, R. F., Giorgini, J. D., Slade, M. A., and Campbell, D. B. (2002). Binary asteroids in the near-Earth object population. *Science*, 296:1445–1448.

[Miller et al., 2002] Miller, J. K., Konopliv, A. S., Antreasian, P. G., Bordi, J. J., Chesley, S., Helfrich, C. E., Owen, W. M., Wang, T. C., Williams, B. G., Yeomans, D. K., and Scheeres, D. J. (2002). Determination of shape, gravity, and rotational state of asteroid 433 Eros. *Icarus*, 155:3–17.

[Morbidelli and Vokrouhlický, 2003] Morbidelli, A. and Vokrouhlický, D. (2003). The Yarkovsky-driven origin of near-Earth asteroids. *Icarus*, 163:120–134.

[Mottola et al., 1997] Mottola, S., Erikson, A., Harris, A. W., Hahn, G., Neukum, G., Buie, M. W., Sears, W. D., Harris, A. W., Tholen, D. J., Whiteley, R. J., Magnusson, P., Piironen, J., Kwiatkowski, T., Borczyk, W., Howell, E. S., Hicks, M. D., Fevig, R., Krugly, Y. N., Velichko, F. P., Chiorny, V. G., Gaftonyuk, N. M., di Martino, M., Pravec, P., Sarounova, L., Wolf, M., Worman, W., Davies, J. K., Schober, H.-J., and Pych, W. (1997). Physical model of near-Earth asteroid 6489 golevka (1991 JX) from optical and infrared observations. *The Astronomical Journal*, 114:1234–1245.

[Muinonen and Lagerros, 1998] Muinonen, K. and Lagerros, J. S. V. (1998). Inversion of shape statistics for small solar system bodies. *Astronomy and Astrophysics*, 333:753–761.

[Muinonen, 1996] Muinonen, K. (1996). Light scattering by gaussian random particles. *Earth, Moon and Planets*, 72:339–342.

[Muinonen, 1998] Muinonen, K. (1998). Introducing the gaussian shape hypothesis for asteroids and comets. *Astronomy and Astrophysics*, 332:1087–1098.

[Nesvorný and Bottke, 2004] Nesvorný, D. and Bottke, W. F. (2004). Detection of the Yarkovsky effect for main-belt asteroids. *Icarus*, 170:324–342.

[Öpik, 1951] Öpik, E. J. (1951). Collision probability with the planets and the distribution of planetary matter. *Proc. R. Irish Acad. Sect. A*, 54:165–199.

[Ostro et al., 2004] Ostro, S. J., Benner, L. A. M., Nolan, M. C., Magri, C., Giorgini, J. D., Scheeres, D. J., Broschart, S. B., Kaasalainen, M., Vokrouhlický, D., Chesley, S. R., Margot, J.-L., Jurgens, R. F., Rose, R., Yeomans, D. K., Suzuku, S., and de Jong, E. M. (2004). Radar observations of asteroid 25143 Itokawa (1998 SF36). *Meteoritics and Planetary Science*, 39:407–424.

[Ostro et al., 1991] Ostro, S. J., Harmon, J. K., Hine, A. A., Perillat, P., Campbell, D. B., Chandler, J. F., Shapiro, I. I., Jurgens, R. F., and Yeomans, D. K. (1991). High-resolution radar ranging to near-Earth asteroids. In *Bulletin of the American Astronomical Society*, pages 1144–+.

[Ostro et al., 1999] Ostro, S. J., Hudson, R. S., Rosema, K. D., Giorgini, J. D., Jurgens, R. F., Yeomans, D. K., Chodas, P. W., Winkler, R., Rose, R., Choate, D., Cormier, R. A., Kelley, D., Littlefair, R., Benner, L. A. M., Thomas, M. L., and Slade, M. A. (1999). Asteroid 4179 Toutatis: 1996 radar observations. *Icarus*, 137:122–139.

[Ostro et al., 2006] Ostro, S. J., Margot, J.-L., Benner, L. A. M., Giorgini, J. D., Scheeres, D. J., Fahnestock, E. G., Broschart, S. B., Bellerose, J., Nolan, M. C., Magri, C., Pravec, P., Scheirich, P., Rose, R., Jurgens, R. F., De Jong, E. M., and Suzuki, S. (2006). Radar imaging of binary near-Earth asteroid (66391) 1999 KW4. *Science*, 314:1276–1280.

[Ostro et al., 1999] Ostro, S. J., Pravec, P., Benner, L. A. M., Hudson, R. S., Šarounov, L., Hicks, M. D., Rabinowitz, D. L., Scotti, J. V., Tholen, D. J., Wolf, M., Jurgens, R. F., Thomas, M. L., Giorgini, J. D., Chodas, P. W., Yeomans, D. K., Rose, R., Frye, R., Rosema, K. D., Winkler, R., and Slade, M. A. (1999). Radar and optical observations of asteroid 1998 KY26. *Science*, 285(5427):557–559.

[Paddack, 1969] Paddack, S. J. (1969). Rotational bursting of small celestial bodies: Effects of radiation pressure. *Journal of Geophysical Research*, 74:7379–4381.

[Peterson, 1976] Peterson, C. (1976). A source mechanism for meteorites controlled by the Yarkovsky effect. *Icarus*, 29:91–111.

[Press et al., 1992] Press, W. H., Teukolsky, S. A., Vetterling, W. T., and Flannery, B. P. (1992). *Numerical recipes, 2nd edition*. Cambridge University Press, New York.

[Radzievskii, 1952] Radzievskii, V. V. (1952). A mechanism for the disintegration of asteroids and meteorites. *Astron. Zh.*, 29:162–170.

[Radzievskii, 1954] Radzievskii, V. V. (1954). A mechanism for the disintegration of asteroids and meteorites. *Dokl. Akad. Nauk SSSR*, 97:49–52.

[Robie et al., 1970] Robie, R. A., Hemingway, B. S., and Wilson, W. H. (1970). Specific heats of lunar surface materials from 90° to 350°K. *Geochimica et Cosmochimica Acta Supplement*, 1:2361.

[Rubincam, 1987] Rubincam, D. P. (1987). LAGEOS orbit decay due to infrared radiation from Earth. *Journal of Geophysical research*, 92:1287–1294.

[Rubincam, 1990] Rubincam, D. P. (1990). Drag on the Lageos satellite. *Journal of Geophysical research*, 95:4881–4886.

[Rubincam, 2000] Rubincam, D. P. (2000). Radiative spin-up and spin-down of small asteroids. *Icarus*, 148:2–11.

[Saito et al., 2006] Saito, J., Miyamoto, H., Nakamura, R., Ishiguro, M., Michikami, T., Nakamura, A. M., Demura, H., Sasaki, S., Hirata, N., Honda, C., Yamamoto, A., Yokota, Y., Fuse, T., Yoshida, F., Tholen, D. J., Gaskell, R. W., Hashimoto, T., Kubota, T., Higuchi, Y., Nakamura, T., Smith, P., Hiraoka, K., Honda, T., Kobayashi, S., Furuya, M., Matsumoto, N., Nemoto, E., Yukishita, A., Kitazato, K., Dermawan, B., Sogame, A., Terazono, J., Shinohara, C., and Akiyama, H. (2006). Detailed images of asteroid 25143 Itokawa from Hayabusa. *Science*, 312:1341–1344.

[Scheeres et al., 2007] Scheeres, D. J., Abe, M., Yoshikawa, M., Nakamura, R., Gaskell, R. W., and Abell, P. A. (2007). The effect of YORP on Itokawa. *Icarus,* in press.

[Scheeres, 2007] Scheeres, D. J. (2007). The dynamical evolution of uniformly rotating asteroids subject to YORP. *Icarus,* in press.

[Sedlák and Štoll, 1993] Sedlák, B. and Štoll, I. (1993). *Elektřina a magnetismus.* Academia and Charles University, Prague.

[Simonelli et al., 1993] Simonelli, D. P., Thomas, P. C., Carcich, B. T., and Veverka, J. (1993). The generation and use of numerical shape models for irregular Solar System objects. *Icarus*, 103:49–61.

[Slivan, 2002] Slivan, S. M. (2002). Spin vector alignment of Koronis family asteroids. *Nature*, 419:49–51.

[Spencer et al., 1989] Spencer, J. R., Lebofsky, L. A., and Sykes, M. V. (1989). Systematic biases in radiometric diameter determinations. *Icarus*, 78:337–354.

[Svoboda and Bakule, 1992] Svoboda, E. and Bakule, R. (1992). *Molekulová fyzika.* Academia, Praha.

[Swihart, 1971] Swihart, T. L. (1971). *Basic physics of stellar atmospheres.* Astronomy and astrophysics series. In: Intermediate short texts in Astrophysics, Tucson: Pachart Publishing House, 1971.

[Taylor et al., 2007] Taylor, P. A., Margot, J. L., Vokrouhlický, D. Scheeres, D. J., Pravec, P., Lowry, S. C., Fitzsimmons, A., C., N. M., Ostro, S. J., Benner, L. A., Giorgini, J. D., and Magri, C. (2007). Increasing spin rate of asteroid 54509 (2000 PH5) a result of the YORP effect. *Science,* in press.

[Thomas et al., 1996] Thomas, P. C., Belton, M. J. S., Carcich, B., Chapman, C. R., Davies, M. E., Sullivan, R., and Veverka, J. (1996). The shape of Ida. *Icarus*, 120:20–32.

[Urquhart and Jakosky, 1997] Urquhart, M. L. and Jakosky, B. M. (1997). Lunar thermal emission and remote determination of surface properties. *Journal of Geophysical Research*, 102:10 959–10 969.

[Vitásek, 1987] Vitásek, E. (1987). *Numerické metody.* Státní nakladatelství technické literatury, Praha.

[Vokrouhlický et al., 2007] Vokrouhlický, D., Breiter, S., Nesvorný, D., and Bottke, W. F. (2007). Generalized YORP evolution: onset of tumbling and new asymptotic states. *Icarus,* submitted.

[Vokrouhlický et al., 2006a] Vokrouhlický, D., Brož, M., Bottke, W. F., Nesvorný, D., and Morbidelli, A. (2006a). Yarkovsky/YORP chronology of asteroid families. *Icarus*, 182:118–142.

[Vokrouhlický et al., 2006b] Vokrouhlický, D., Brož, M., Morbidelli, A., Bottke, W. F., Nesvorný, D., Lazzaro, D., and Rivkin, A. S. (2006b). Yarkovsky footprints in the Eos family. *Icarus*, 182:92–117.

[Vokrouhlický and Brož , 1999] Vokrouhlický, D. and Brož , M. (1999). An improved model of the seasonal Yarkovsky force for regolith-covered asteroid fragments. *Astronomy and Astrophysics*, 350:1079–1084.

[Vokrouhlický and Farinella, 1998] Vokrouhlický, D. and Farinella, P. (1998). Orbital evolution of asteroidal fragments into the nu_6 resonance via Yarkovsky effects. *Astronomy and Astrophysics*, 335:351–362.

[Vokrouhlický and Farinella, 1999] Vokrouhlický, D. and Farinella, P. (1999). The Yarkovsky seasonal effect on asteroidal fragments: A nonlinearized theory for spherical bodies. *Astrophysical Journal*, 118:3049–3060.

[Vokrouhlický and Farinella, 2000] Vokrouhlický, D. and Farinella, P. (2000). Efficient delivery of meteorites to the Earth from a wide range of asteroid parent bodies. *Nature*, 407:606–608.

[Vokrouhlický et al., 2000] Vokrouhlický, D., Milani, A., and Chesley, S. R. (2000). Yarkovsky effect on small near-Earth asteroids: Mathematical formulation and examples. *Icarus*, 148:118–138.

[Vokrouhlický and Milani, 2000] Vokrouhlický, D. and Milani, A. (2000). Direct solar radiation pressure on the orbits of small near-Earth asteroids: observable effects? *Astronomy and Astrophysics*, 362:746–755.

[Vokrouhlický et al., 2003] Vokrouhlický, D., Nesvorný, D., and Bottke, W. F. (2003). The vector alignments of asteroid spins by thermal torques. *Nature*, 425:147–151.

[Vokrouhlický et al., 2005a] Vokrouhlický, D., Čapek, D., Chesley, S. R., and Ostro, S. J. (2005a). Yarkovsky detection opportunities. I. Solitary asteroids. *Icarus*, 173:166–184.

[Vokrouhlický et al., 2005b] Vokrouhlický, D., Čapek, D., Chesley, S. R., and Ostro, S. J. (2005b). Yarkovsky detection opportunities. *Icarus*, 179:128–138.

[Vokrouhlický et al., 2004] Vokrouhlický, D., Čapek, D., Kaasalainen, M., and Ostro, S. J. (2004). Detectability of YORP rotational slowing of asteroid 25143 Itokawa. *Astronomy and Astrophysics*, 414:L21–L24.

[Vokrouhlický and Čapek, 2002] Vokrouhlický, D. and Čapek, D. (2002). YORP-induced long-term evolution of the spin state of small asteroids and meteoroids: Rubincam's approximation. *Icarus*, 159:449–467.

[Vokrouhlický, 1998a] Vokrouhlický, D. (1998a). Diurnal Yarkovsky effect as a source of mobility of meter-sized asteroidal fragments. I. Linear theory. *Astronomy and Astrophysics*, 335:1093–1100.

[Vokrouhlický, 1998b] Vokrouhlický, D. (1998b). Diurnal Yarkovsky effect as a source of mobility of meter-sized asteroidal fragments. II. Non-sphericity effects. *Astronomy and Astrophysics*, 338:353–363.

[Vokrouhlický, 1999] Vokrouhlický, D. (1999). A complete linear model for the Yarkovsky thermal force on spherical asteroid fragments. *Astronomy and Astrophysics*, 344:362–366.

[Winter and Saari, 1969] Winter, D. F. and Saari, J. M. (1969). A particulate model of the lunar soil. *The Astrophysical Journal*, 156:1135–1151.

[Yomogida and Matsui, 1983] Yomogida, K. and Matsui, T. (1983). Physical properties of ordinary chondrites. *Journal of Geophysical Research*, 88:9513–9533.